





**DEVELOPMENT AND PROCESSING OF  
NICKEL ALUMINIDE-CARBIDE ALLOYS**

A Thesis  
Presented for the  
Master of Science  
Degree  
University of Tennessee, Knoxville

Timothy Scott Newport



## ACKNOWLEDGMENT

Several individuals were instrumental in the pursuit of this investigation. As my advisor for this project, Dr. B. F. Oliver has been patient, forgiving, and helpful in all respects. It has been an honor to work with him and his advise has been greatly appreciated. I would also like to thank Dr. D. R. Johnson and Dr. S. M. Joslin for their friendship and guidance. Their helpful discussions and instructions were beneficial in assimilating me to the graduate program. Thanks to Dr. C. R. Brooks for his helpful discussion of the microstructures and solidification behavior of these alloys. Thanks also to Dr. W. T. Becker and Dr. J. E. Spruiell for their confidence in me as a graduate student.

Dr. R. D. Noebe, NASA Lewis Research Center, has been beneficial in both his financial and technical support of this research. Without his and NASA's support of Dr. Oliver's research program for the past seven years, much of the work presented here and by former graduate students would not have been possible.

Special thanks to Mr. B. L. McGill for his suggestions and assistance with the scanning electron microscopy. Thanks also to Mr. Ron Johnson for his assistance in maintaining the equipment and software in the High Temperature Metals Research Laboratory. Other members of the Electronics Shop provided additional support. I also would like to thank the Machine Shop for sample preparation and test fixtures. Thanks are also in order for Dr. John Dunlap and Mr. Dick Williams of the Biology Electron Microscopy Facility for their assistance with the transmission electron microscopy.

Special thanks to my friends, Robert Perrin, Chuck Thomas, Daryl Grummitt, Richard Edwards, Mike Strauss, and Dr. Paul Qiao, for their helpful discussions and friendship. Apologizes to anyone left from this acknowledgment.

## ABSTRACT

With the upper temperature limit of the Ni-based superalloys attained, a new class of materials is required. Intermetallics appear as likely candidates because of their attractive physical properties. With a relatively low density, high thermal conductivity, excellent oxidation resistance, high melting point, and simple crystal structure, nickel aluminide (NiAl) appears to be a potential candidate. However, NiAl is limited in structural applications due to its low room temperature fracture toughness and poor elevated temperature strength. One approach to improving these properties has been through the application of eutectic composites. Researchers have shown that containerless directional solidification of NiAl-based eutectic alloys can provide improvements in both the creep strength and fracture toughness.

Although these systems have shown improvements in the mechanical properties, the presence of refractory metals increases the density significantly in some alloys. Lower density systems, such as the carbides, nitrides, and borides, may provide NiAl-based eutectic structures. With little or no information available on these systems, experimental investigation is required.

The objective of this research was to locate and develop NiAl-carbide eutectic alloys. Exploratory arc-melts were performed in NiAl-refractory metal-C systems. Refractory metal systems investigated included Co, Cr, Fe, Hf, Mo, Nb, Ta, Ti, W, and Zr. Systems containing carbides with excellent stability (i.e., HfC, NbC, TaC, TiC, and ZrC) produced large blocky, cubic carbides in an NiAl matrix. The carbides appeared to have formed in the liquid state and were randomly distributed throughout the polycrystalline NiAl. The Co, Cr, Fe, Mo, and W systems contained NiAl dendrites with a two-phase interdendritic microconstituent present. Of these systems, the NiAl-Mo-C system had the most promising microstructural for in-situ composites.

Three processing techniques were used to evaluate the NiAl-Mo-C system: arc-melting, slow cooling, and containerless directional solidification. Arc-melting provided a wide range of compositions in an economical and simple fashion. The slow cooled ingots provided larger ingots and slower cooling rates than arc-melting. Directional solidification was used to produce in-situ composites consisting of NiAl reinforced with molybdenum carbides.

Dramatic changes in microstructures were observed for small compositional variations ( $< 0.1$  at. %) in the arc-melted ingots. Regions containing specific primary phases or two-phase microconstituents were identified. A unique structure to this system was recognized: the "spline". Basically a large, broken lamellar sheet surrounded by a sheath of NiAl, the spline was observed in arc-melts, slow cooled ingots, or spilled liquid during directional solidification. In fact, these splines, still surrounded by NiAl, remained after high temperature heat treatments. Heat treatments also revealed Widmanstatten-type precipitation in the slow cooled NiAl-1Mo-1C ingots.

The slow cooled ingots contained large regions of aligned carbides and graphite in an NiAl matrix. The existence of a broken lamellar eutectic in this system is possible. Morphology, solidification behavior, and volume fraction all support this theory but uncertainty remains. The Widmanstatten precipitation may also be confusing the results. Although MoC has been identified by x-ray diffraction as the reinforcing phase, it is possible that more than one carbide is present.

In-situ reaction of graphite with the liquid zone during containerless directional solidification proved unsuccessful. A graphite coating, with high emissivity, coated the surface of the liquid thus limiting induction melting. Two ingots, NiAl-1Mo-0.61C and NiAl-1Mo-0.73C were successfully directionally solidified. Although consisting primarily of polycrystalline NiAl with a fine dispersion of carbides, regions near the end of processing contained aligned carbides. Directional solidification of NiAl-1Mo-

1C ingots was impaired by the formation of a coating on the liquid zone. This coating is most likely graphite, but could be a carbide precipitating from the liquid.

Four-point flexure testing and creep compression testing were performed on the directionally solidified NiAl-Mo-C ingots. Fracture toughness values ranged from 10.4 to 13.5 MPa $\sqrt{m}$  compared to 4 to 6 MPa $\sqrt{m}$  for polycrystalline NiAl. Although much less than many of the other NiAl-based eutectic systems, the creep strength was also greater than that of single crystal NiAl. However, these mechanical properties do not represent the optimum morphology, volume fraction, or growth conditions for this system.

## TABLE OF CONTENTS

1.	<b>INTRODUCTION AND REVIEW</b> . . . . .	1
	Introduction and Objectives . . . . .	1
	Literature Review . . . . .	3
	Nickel aluminide . . . . .	3
	Physical properties . . . . .	3
	Mechanical behavior . . . . .	7
	Polyphase in-situ composites . . . . .	11
	Carbides . . . . .	15
2.	<b>ALLOY DEVELOPMENT</b> . . . . .	19
	Introduction . . . . .	19
	Experimental Procedures . . . . .	19
	Arc-melted ingots . . . . .	19
	Metallography . . . . .	20
	Results . . . . .	20
	Discussion . . . . .	22
3.	<b>PROCESSING OF NiAl-Mo-C ALLOYS</b> . . . . .	26
	Introduction . . . . .	26
	Experimental Procedures . . . . .	26
	Arc-melting . . . . .	26
	Slow cooling . . . . .	26
	Containerless directional solidification . . . . .	27
	Results . . . . .	30
	Arc-melting . . . . .	30
	Slow cooling . . . . .	32
	Containerless directional solidification . . . . .	32
	Discussion . . . . .	40

4.	MICROSTRUCTURES OF NiAl-Mo-C ALLOYS . . . . .	46
	Introduction . . . . .	46
	Experimental Procedures . . . . .	46
	Optical microscopy . . . . .	46
	Scanning electron microscopy . . . . .	47
	Transmission electron microscopy . . . . .	47
	Differential thermal analysis . . . . .	48
	X-ray diffraction . . . . .	48
	Results . . . . .	49
	Arc-melted ingots . . . . .	49
	Slow cooled ingots . . . . .	62
	Heat treated ingots . . . . .	70
	Directionally solidified ingots . . . . .	70
	Discussion . . . . .	82
5.	MECHANICAL PROPERTIES OF NiAl-Mo-C ALLOYS. . . . .	88
	Introduction . . . . .	88
	Experimental procedures . . . . .	88
	Flexure testing . . . . .	88
	Compression testing . . . . .	90
	Results . . . . .	90
	Room temperature fracture toughness . . . . .	90
	Elevated temperature strength . . . . .	92
	Discussion . . . . .	98
6	SUMMARY. . . . .	101
	Conclusions . . . . .	101
	Recommendations. . . . .	102
	LIST OF REFERENCES . . . . .	104
	APPENDICES . . . . .	110
	APPENDIX A: X-RAY DIFFRACTION RESULTS . . . . .	111
	APPENDIX B: DTA RESULTS . . . . .	118
	APPENDIX C: FLEXURE TESTING RESULTS . . . . .	122
	APPENDIX D: COMPRESSION TESTING RESULTS. . . . .	126
	VITA . . . . .	132

**LIST OF TABLES**

Table 1:	Characterization of NiAl-based eutectics directionally solidified by containerless means at the University of Tennessee . . . . .	13
Table 2:	Selected physical and mechanical properties of various refractory metal carbides, summarized from [63, 64]. . . . .	17
Table 3:	Free energy of formation for several carbides, summarized from [63]. . . . .	24
Table 4:	Slow cooled ingots prepared by melting within an induction furnace at 0.05 MPa helium. . . . .	33
Table 5:	Precursor ingots prepared at the University of Tennessee-Knoxville (UTK) and NASA Lewis Research Center (NLRC) with containerless directional solidification processing conditions. . . . .	34
Table 6:	Four point flexure results for containerless directionally solidified and slow cooled NiAl-Mo-C ingots. . . . .	91
Table 7:	Representative creep behavior of NiAl-Mo-C alloys compared to stoichiometric single crystal NiAl. . . . .	96

## LIST OF FIGURES

Figure 1:	Phase diagram for the nickel-aluminum system [5] . . . . .	4
Figure 2:	Crystal structure of NiAl represented as (a) B2 (CsCl type) and (b) interpenetrating simple cubic sublattices of Al and Ni. . . . .	5
Figure 3:	Improvement in the room temperature ductility of NiAl crystals, [001] orientation, with microalloying [1]. . . . .	9
Figure 4:	Performance plot of various NiAl-based eutectic systems directionally solidified at the University of Tennessee, modified from [24]. . . . .	14
Figure 5:	Density adjusted performance plot of various NiAl-based eutectic systems directionally solidified at the University of Tennessee, modified from [3]. . . . .	16
Figure 6:	Light optical micrographs of NiAl-refractory metal-carbon arc-melts (at. %): (a) NiAl-1Nb-1.02C (b) NiAl-0.97Hf-1C, (c) NiAl-1Ta-1C, (d) NiAl-2Ti-2.04C,, and (e) NiAl-1.95Zr-1.81C. . . . .	22
Figure 7:	Light optical micrographs of NiAl-refractory metal-carbon arc-melts (at. %): (a) NiAl-0.76Co-1.05C, (b) NiAl-1.02Cr-0.97C, (c) NiAl-0.99Fe-1.05C, (d) NiAl-1Mo-1C, and (e) NiAl-0.7W-1.05C. . . . .	23
Figure 8:	Plot of free energy of formation versus temperature for various refractory carbides [plotted from data in Table 3]. . . . .	25
Figure 9:	Schematic of a molten zone during directional solidification [2, 65]. . . . .	29
Figure 10:	Compositions of arc-melts made in the NiAl-rich corner of the NiAl-Mo-C system. . . . .	31
Figure 11:	NiAl-1Mo precursor ingot directionally solidified in a stagnant atmosphere of methane and helium. . . . .	36

Figure 12:	Directionally solidified NiAl-1Mo ingot processed in a flowing atmosphere of methane and helium with emphasis on (a) processed region and (b) deposited film. . . . .	37
Figure 13:	NiAl-1Mo-0.59C ingot with graphite dots on unprocessed region of the ingot. . . . .	38
Figure 14:	As processed, directionally solidified ingots of (a) NiAl-1Mo-0.61C and (b) NiAl-1Mo-0.73C. . . . .	39
Figure 15:	Melt record for NiAl-1Mo-0.73C directionally solidified ingot. Shown are (a) liquid diameter, (b) percent power, (c) temperature, (d) stretch/squeeze, (e) interface position, (f) solid diameter, (g) rotation, (h) velocity, and (i) relative ingot position. . . . .	41
Figure 16:	Failed directional solidification of an NiAl-1Mo-1C precursor ingot. . . . .	42
Figure 17:	Schematic binary phase diagram for (a) eutectic reaction and (b) peritectic reaction. . . . .	44
Figure 18:	Light optical micrographs of arc-melted ingots with compositions of (a) NiAl-1.58Mo-0.41C and (b) NiAl-1Mo-0.5C. . . . .	50
Figure 19:	Light optical micrographs of arc-melted ingots with compositions of (a) NiAl-1Mo-1C and (b) NiAl-0.5Mo-1.5C. . . . .	51
Figure 20:	Light optical micrographs of arc-melted ingots with compositions of (a) NiAl-1Mo-1.5C and (b) NiAl-2.75Mo-1.24C. . . . .	52
Figure 21:	Arc-melted ingot compositions containing (a) "splines" with NiAl sheath, (b) graphite flakes, and (c) NiAl dendrites (no spline). . . . .	53
Figure 22:	Arc-melted ingot compositions containing (a) NiAl-MoC? (sheet) two-phase structure, (b) NiAl-MoC? (fine) two-phase structure, and (c) NiAl-Mo two-phase eutectic. . . . .	54

Figure 23:	SEM backscattered electron micrograph of an arc-melted NiAl-1Mo-1C ingot showing splines with lattice-type structures. . . . .	55
Figure 24:	SEM backscattered electron micrograph of an arc-melted NiAl-1.58Mo-0.41C ingot showing a "spline" with sheath and the NiAl-MoC? (fine) constituent. . . . .	57
Figure 25:	Brightfield TEM photomicrograph of extracted particles from an arc-melted NiAl-1.58Mo-0.41C ingot. . . . .	58
Figure 26:	Brightfield TEM photomicrograph of extracted particles from an arc-melted NiAl- 1.58Mo-0.41C ingot. . . . .	59
Figure 27:	Brightfield TEM photomicrograph of extracted particles from an arc-melted NiAl-1.58Mo-0.41C ingot. . . . .	59
Figure 28:	Brightfield TEM photomicrograph of extracted particles from an arc-melted NiAl-1.58Mo-0.41C ingot. . . . .	60
Figure 29:	Brightfield TEM photomicrograph of extracted particles from an arc-melted NiAl-2.75Mo-1.24C ingot. . . . .	60
Figure 30:	Brightfield TEM photomicrograph of extracted particles from an arc-melted NiAl- 0.5Mo-1.5C ingot. . . . .	61
Figure 31:	Backscattered SEM micrograph of a heavily etched slow cooled NiAl-1Mo-3C ingot showing spline with holes. . . . .	63
Figure 32:	Light optical micrographs showing aligned carbides in slow cooled ingots (a) NiAl-1Mo-1C and (b) NiAl-1Mo-3C. . . . .	64
Figure 33:	Backscattered SEM micrographs showing aligned carbides in slow cooled ingot SC-2 (NiAl-1Mo-1C). . . . .	65
Figure 34:	Light optical micrograph showing broken lamellar sheets of carbides in a slow cooled NiAl-1Mo-3C ingot. . . . .	66
Figure 35:	Backscattered SEM micrograph showing branched carbides in slow cooled ingots (a) SC-2 (NiAl-1Mo-1C) and (b) SC-6 (NiAl-1Mo-3C). . . . .	67

Figure 36:	Backscattered SEM micrograph for slowed cooled ingot SC-7 (NiAl-1Mo-1C) showing spline with NiAl sheath surrounded by aligned carbides. . . . .	68
Figure 37:	Brightfield TEM photomicrograph of particles protruding from the matrix of Ingot SC-2 (NiAl-1Mo-1C).. . . . .	69
Figure 38:	Backscattered SEM micrograph of a slow cooled NiAl-1Mo-1C ingot after differential thermal analysis. . . . .	71
Figure 39:	Light optical photomicrographs of characteristic microstructures for a slow cooled NiAl-1Mo-1C ingot prior to heat treatments. . . . .	72
Figure 40:	Light optical micrographs for a slow cooled NiAl-1Mo-1C ingot annealed at 1603 K for 3 hours and furnace cooled. . . . .	73
Figure 41:	Light optical micrographs for a slow cooled NiAl-1Mo-1C ingot annealed at 1623 K for 6 hours and furnace cooled. . . . .	74
Figure 42:	Light optical micrographs for a slow cooled NiAl-1Mo-1C ingot annealed at 1723 K for 3 hours and furnace cooled. . . . .	75
Figure 43:	Backscattered SEM micrograph for a slow cooled NiAl-1Mo-1C ingot annealed at 1623 K for 6 hours and furnace cooled. . . . .	76
Figure 44:	Light optical micrographs of cast precursor ingots (a) MoC #1 (NiAl-1Mo-0.59C) and (b) MoC #3 (NiAl-1Mo-0.73C).. . . . .	78
Figure 45:	Light optical micrographs for directionally solidified Ingot MoC #3 (NiAl-1Mo-0.73C) showing transition from (a) near first zone to (d) just before last zone.. . . .	79
Figure 46:	Light optical micrographs for directionally solidified ingot MoC #4 (NiAl-1Mo-1C). . . . .	80

Figure 47:	Light optical micrographs for a spill which occurred during containerless directional solidification of Ingot MoC #4 showing (a) splines and (b) Widmanstatten-type structure. . . . .	81
Figure 48:	Light optical micrographs for a spill which occurred during containerless directional solidification of Ingot MoC #2 showing splines with a sheath of NiAl surrounding each. . . . .	81
Figure 49:	Simulated diffraction patterns with a zone axis of (0001) for (a) MoC and (b) Mo <sub>2</sub> C. Information for atom locations and lattice constants taken from [75]. . . . .	83
Figure 50:	Phase diagram for the molybdenum-carbon system [5]. . . . .	85
Figure 51:	Geometry of the four-point flexure testing fixture and bend sample [2]. . . . .	89
Figure 52:	Backscattered SEM micrograph of a fracture surface from a directionally solidified NiAl-1Mo-0.73C bend specimen. . . . .	93
Figure 53:	Backscattered SEM micrograph of a fracture surface from a directionally solidified NiAl-1Mo-0.73C bend specimen. . . . .	94
Figure 54:	Secondary SEM micrograph of a fracture surface from a directionally solidified NiAl-1Mo-0.61C bend specimen. . . . .	94
Figure 55:	Secondary SEM micrograph of a fracture surface from a directionally solidified NiAl-1Mo-0.61C bend specimen. . . . .	95
Figure 56:	1300 K compressive flow stress-strain rate behavior for directionally solidified and slow cooled NiAl-Mo-C compared to NiAl and NASAIR 100 [78, 79]. . . . .	97
Figure 57:	Performance plot of various NiAl-based eutectic systems directionally solidified at the University of Tennessee with the NiAl-Mo-C system included, modified from [24]. . . . .	100

Figure A1:	Powder x-ray diffraction scan for an arc-melted NiAl-1Mo-1C ingot. . . . .	112
Figure A2:	Powder x-ray diffraction scan for an arc-melted NiAl-1Mo-1C ingot. . . . .	113
Figure A3:	Powder x-ray diffraction scan for an arc-melted NiAl-0.9Mo-0.9C ingot. . . . .	114
Figure A4:	Powder x-ray diffraction scan for a slow cooled NiAl-1Mo-1C ingot. . . . .	115
Figure A5:	Powder x-ray diffraction scan for an arc-melted NiAl-1Mo-1C ingot etched in Solution 1 for several days. . . . .	116
Figure A6:	Powder x-ray diffraction scan for an arc-melted NiAl-1Mo-1C ingot etched in Solution 2 for several days. . . . .	117
Figure B1:	DTA scan for material taken from an NiAl-1Mo-1C slow cooled ingot. . . . .	119
Figure B2:	DTA scan for material taken from an NiAl-1Mo-0.61C directionally solidified ingot. . . . .	120
Figure B3:	DTA scan for material taken from an NiAl-1Mo-0.73C directionally solidified ingot. . . . .	121
Figure C1:	Load-displacement curves for 4-point flexure testing of a directionally solidified NiAl-1Mo-0.61C ingot. . . . .	123
Figure C2:	Load-displacement curves for 4-point flexure testing of a directionally solidified NiAl-1Mo-0.61C ingot. . . . .	124
Figure C3:	Load-displacement curves for 4-point flexure testing of a directionally solidified NiAl-1Mo-0.73C ingot. . . . .	125
Figure D1:	True compressive stress-true compressive strain curves for NiAl-Mo-C directionally solidified ingots at 1200 K. . . . .	127
Figure D2:	True compressive stress-true compressive strain curves for NiAl-Mo-C directionally solidified ingots at 1300 K. . . . .	128

Figure D3: True compressive stress-true compressive strain curves  
for NiAl-Mo-C slow cooled ingots at 1100 K. . . . . 129

Figure D4: True compressive stress-true compressive strain curves  
for NiAl-Mo-C slow cooled ingots at 1200 K. . . . . 130

Figure D5: True compressive stress-true compressive strain curves  
for NiAl-Mo-C slow cooled ingots at 1300 K. . . . . 131

## CHAPTER 1

### INTRODUCTION AND REVIEW

#### Introduction and Objectives

Needed technological advances within the aerospace and other industries require new high temperature materials to meet higher standards of operation. The upper temperature limit of the current superalloys appear stable suggesting that the development of a new class of materials is required. Intermetallic compounds initially appear to be likely candidates but are often limited by certain mechanical properties. One promising compound is nickel aluminide (NiAl). Currently used as coating on nearly all high-pressure turbine blades, NiAl has several properties of engineering significance [1]. However, NiAl has a low room temperature fracture toughness and poor elevated temperature strength, limiting its use as a structural material. Improvement of these properties has been the primary goal in attempting to develop NiAl as an engineering material.

One promising approach has been the development of NiAl-based eutectic in-situ composites. Typical processing methods involve casting, extrusion, or directional solidification. Directional solidification is a likely choice of processing technique to develop composites with oriented structures and properties. Several NiAl-based systems have recently been developed and directionally solidified by containerless means at the University of Tennessee [2, 3]. Compared to binary NiAl, these systems exhibited improvements in both the room temperature fracture toughness and high temperature creep behavior.

The eutectic structures studied show significant improvements over binary NiAl while maintaining many of the properties which originally attracted researchers. While

the oxidation resistance and thermal conductivity are only slightly altered in many of the systems, the density and melting points can become critical issues. Although NiAl has an extremely high melting point, some of the eutectic temperatures are much lower. For some of these systems, this may be a limiting factor. Density also becomes a concern when the reinforcing phase(s) are a much higher density than that of stoichiometric NiAl. To alleviate this potential problem, emphasis has recently been placed on locating and developing lower density NiAl-based eutectic systems. Potential systems include those containing compounds formed by the interstitial elements: boron, carbon, nitrogen, oxygen, and sulfur.

Much current research has concentrated on the removal or limitation of interstitial elements from most alloys. The refractory compounds formed by these elements include the borides, carbides, nitrides, oxides, and sulfides. While the binary phase diagrams for these individual compounds tend to be well known, little constitutional information is available on their interaction with NiAl in more complex systems. The carbides are of particular interest due their high melting points, correspondingly high strength at elevated temperatures, high hardness values, relatively low densities, and good stability [4].

An objective of this research was to explore NiAl-carbide alloys for high temperature applications. The objectives may be stated as:

1. locate NiAl-carbide systems with emphasis on low density, eutectic structures,
2. develop processing techniques for specific systems of interest, including directional solidification where possible
3. evaluate processed materials through microstructural characterization, and
4. evaluate processed materials for room temperature fracture toughness and elevated temperature strength.

## Literature Review

### Nickel aluminide

The nickel-aluminum phase diagram is illustrated in Figure 1 [5].

This system is characterized by several intermetallic compounds. The compound with the highest melting point is nickel aluminide (NiAl). Due to its high melting point, good oxidation resistance, high thermal conductivity, and low density, NiAl has been investigated as a potential high temperature engineering material for at least five decades [6]. In spite of these beneficial physical properties observed in NiAl, the mechanical properties have always been a limiting factor in its use as a structural material. Previous and current research has been established to improve and modify the mechanical behavior of NiAl or NiAl alloys through processing techniques, alloying additions, microstructural control, and/or composites.

### Physical properties

NiAl crystallizes in an ordered body-center cubic structure (B2, CsCl type). Figure 2 is a schematic illustration of this structure and may be described as two interpenetrating simple cubic lattices, one of Ni and the other of Al. The intermetallic compound exists from 45 to 60 at. % Ni at 1000 K, while at more elevated temperatures, the phase field extends from 45 to 68 at. % Ni (Figure 1). With such a large variation in stoichiometry available, physical properties will vary dramatically with the composition of NiAl. At off-stoichiometric compositions (*i.e.*,  $\neq$  Ni-50 at. % Al), constitutional defects are incorporated into the crystal structure. While excess nickel substitutes for aluminum on the aluminum sublattice, excess aluminum produces vacancies in the nickel sublattice [7]. The stoichiometric lattice parameter has been reported as 2.886 Å, but decreases with a variation in the composition [8-12]. The

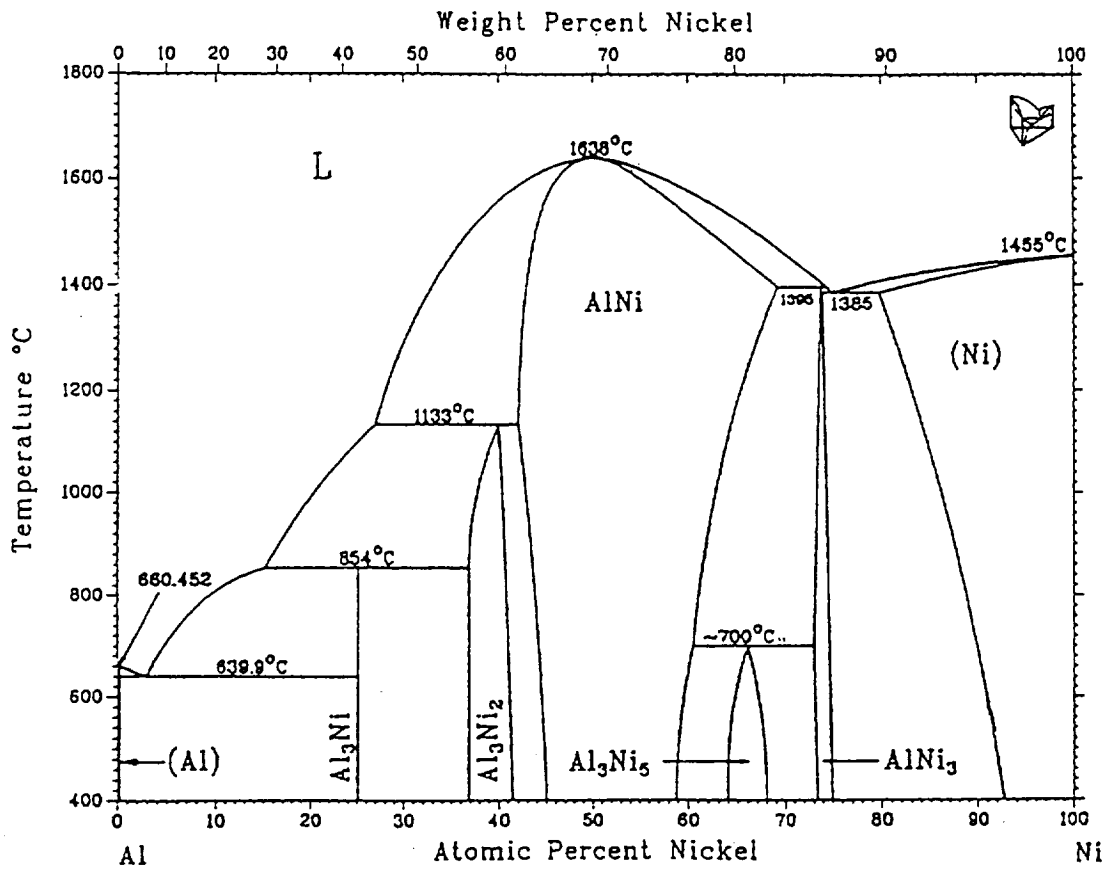


Figure 1: Phase diagram for the nickel-aluminum system [5].

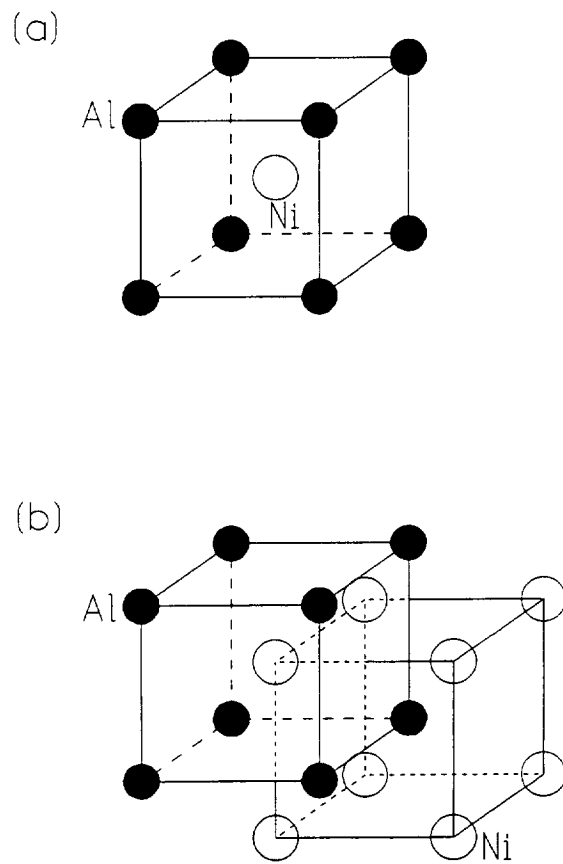


Figure 2: Crystal structure of NiAl represented as (a) B2 (CsCl type) and (b) interpenetrating simple cubic sublattices of Al and Ni.

simple and symmetric crystal system of NiAl provides both advantages and disadvantages. Although the potential for alloying by substitutional or interstitial means are available, the open structure will also provide for much higher diffusion rates than in more complex close-packed structures [1, 13, 14].

The melting point of stoichiometric NiAl is currently an issue of debate. Although the previously reported value of 1911 K is commonly accepted, the most recent efforts report the melting point of stoichiometric NiAl near 1955 K [15]. While this discrepancy has been associated with a steep drop-off in melting temperature due to deviation from stoichiometry, it may also be associated with the unintentional addition of ternary elements [16, 17]. In addition to a high melting point, NiAl also exhibits a high degree of thermal stability [18].

With a density approximately two-thirds that of the nickel superalloys currently used as high-pressure turbine blades, applying NiAl to this technology would provide a reduction in the overall weight of the blades. This reduction would allow for lower centrifugal forces and result in greater efficiency. If the melting point of NiAl is maintained, these blades would allow for higher operating temperatures. Stoichiometric NiAl has a density of  $5.90 \text{ g/cm}^3$  [8-10] The density increases with excess nickel but decreases with excess aluminum as the composition varies from stoichiometry.

Other additional benefits of NiAl as turbine blade material are its excellent oxidation resistance and high thermal conductivity. Currently used as a coating on turbine blades and vanes due its excellent oxidation, NiAl also prevents the development of "hot spots" by distributing the heat across the surface more evenly than conventional superalloys. NiAl has a thermal conductivity four to eight times that of conventional nickel superalloys and one-third that of aluminum [1, 6].

### Mechanical behavior

Although its physical properties are appealing to engineers, NiAl exhibits poor room temperature fracture toughness and low elevated temperature strength which limit its use in structural applications. The predominate slip system in NiAl at room temperature is the  $\langle 100 \rangle \{110\}$  system [19-23]. With only three independent slip systems, NiAl does not have the five independent systems necessary for polycrystalline deformation. Investigations reveal that  $\langle 001 \rangle$  dislocations are dominant within polycrystalline NiAl. While other types have been observed, the numbers are limited and the effect upon properties is not apparent [24].

With polycrystalline deformation appearing to be limited, much research has been invested in the development and growth of single crystals. Two types of behavior appear to be present within NiAl: "hard" and "soft" orientations. "Soft" orientation crystals are those which contain a non- $\langle 100 \rangle$  growth orientation. The observed slip systems within "soft" orientation NiAl have been  $\langle 001 \rangle \{110\}$  and  $\langle 001 \rangle \{100\}$ . These results appear to be independent of temperature [25, 26].

Referred to as the "hard" orientation within NiAl,  $[001]$  oriented crystals are considered a special case. During deformation, the resolved shear stress approaches zero. As this occurs, the stress necessary for deformation is much higher than for other orientations [26, 27]. The observed slip directions vary dramatically with temperature for "hard" orientation crystals. For temperatures ranging from 77 to about 600 K, the primary slip system is  $\langle 111 \rangle \{112\}$  [28, 29]. At temperatures higher than the brittle-ductile transition for NiAl ( $> 600$  K), the operative system changes to  $\langle 001 \rangle \{011\}$  [30, 31].

During deformation, investigators must also be concerned with the location of the cleavage plane. In NiAl, the cleavage planes are  $\{110\}$  types. Therefore, as the critical resolved shear stress increases, so does a normal stress on the cleavage plane.

With these conditions, it becomes extremely difficult to improve both the plane strain fracture toughness and tensile ductility [2].

Attempts to initiate slip on other systems has shown some success. One of the most promising is the application of alloying additions. Additions of Cr, Mn, and V have been theorized to induce  $\langle 111 \rangle$  slip within NiAl [32]. Although results have been mixed, some  $\langle 111 \rangle$  slip vectors have been observed. However, the mechanical behavior of these alloys were relatively unchanged. In general, alloying has been unsuccessful at altering the operative slip system.

Room temperature fracture toughness data is readily available for NiAl. The plane strain fracture toughness at room temperature for polycrystalline NiAl is approximately 4 to 6  $\text{MPa}\sqrt{\text{m}}$  [33-38]. These values appear to be independent of grain size, processing technique, or stoichiometry [32]. Although polycrystalline NiAl has a fairly consistent fracture toughness, single crystal values are very dependent upon orientation. NiAl single crystals notched parallel to the [001] orientation appear to have a higher fracture toughness (10  $\text{MPa}\sqrt{\text{m}}$ ) than those notched with an [011] orientation (6  $\text{MPa}\sqrt{\text{m}}$ ) [39]. The effect of microalloying on the properties of NiAl has also been investigated. Darolia has shown that small additions of Fe, Mo, and Ga to single crystals will improve the tensile ductility of stoichiometric NiAl [1]. However, this effect has been limited to small quantities, microalloying, of each element (Figure 3).

Purity has also been shown to have an impact on the mechanical properties of NiAl. In one study,  $\langle 110 \rangle$  seeded containerless grown NiAl crystals were tested in biaxial tension. Although one specimen exhibited nearly 13% elongation, the other specimens failed by notch sensitivity due to prior surface damage [40]. Another study indicates that commercial purity NiAl single crystals are sensitive to heat treatment and cooling rate, but that zone refined, low interstitial NiAl crystals are not [41, 42].

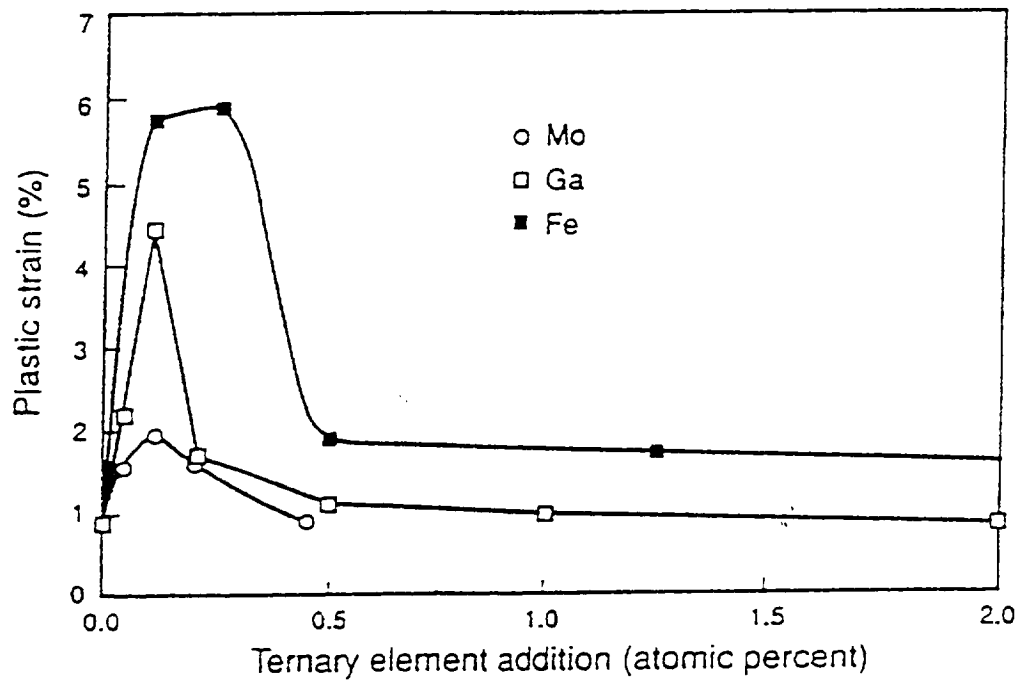


Figure 3: Improvement in the room temperature ductility of NiAl crystals, [001] orientation, with microalloying [1].

When tested in biaxial bending and tension, the high purity crystals were shown to have higher room temperature ductility and fracture strength than commercially pure material [42, 43]. This behavior is consistent with strain aging phenomena and similar to observations made in mild steels [24].

The effect of interstitial elements upon the mechanical properties of NiAl is not completely clear. Although oxygen and nitrogen have been shown to produce no adverse effects on the mechanical properties, recent efforts have stated that carbon is the primary element which produces strain aging in NiAl [24, 41, 44-47]. Although silicon does not appear to initiate strain aging behavior, it has been suggested to enhance the strain aging behavior caused by carbon [47].

Unlike many other intermetallics, microstructural effects on the fracture behavior of NiAl are limited. While decreasing the grain size often produces a higher fracture toughness in some intermetallic systems, the effects on NiAl are only observed above the ductile-brittle transition temperature (DBTT) [48, 49]. For many intermetallics, increasing the content of the more noble metal (e.g. Ni in Ni<sub>3</sub>Al, Ag in AgMg, and Fe in FeAl) increases its ductility. Nickel aluminide is a major exception with the stoichiometric composition producing the lowest DBTT [49].

Through macroalloying and second phase additions, some improvement in fracture toughness has been observed [34, 35, 38]. If processed within the NiAl ( $\beta$ ) + Ni<sub>3</sub>Al ( $\gamma'$ ) region (61.5% Ni), a toughness value of approximately 9 MPa $\sqrt{m}$  is observed. Two possible theories exist about this toughening effect. The first theory suggests a martensitic transformation within the NiAl, while the second theory involves formation of a Ni<sub>3</sub>Al necklace structure around grain boundaries [35, 36]. However, the volume change associated with the transformation appears to be very small. Therefore, the second theory appears to be more logical. The improved toughness can be associated with typical ductile reinforcement. While some attempts at macroalloying

NiAl have succeeded, others have been unsuccessful. Additions of 5% Mn or Cr produced  $\langle 111 \rangle$  dislocations and changed fracture modes from intergranular to transgranular. However, no effect on the fracture toughness was observed [50].

While many intermetallics have a relatively high creep resistance due to their complex crystal structures, the simple B2 crystal structure of NiAl promotes poor creep strength. In general, creep is most commonly due to diffusion processes which are accelerated at elevated temperatures. With the open, simple body-centered cubic structure, it is expected that NiAl exhibits poorer creep resistance than more complex structures such as Ni<sub>3</sub>Al or TiAl [13, 51].

Several methods have been evaluated to improve the overall creep resistance of NiAl. Solid solution hardening and precipitation strengthening are beneficial at high loading rates, but the benefits are lost at slower rates [52]. Second phase additions of more complex compounds, such as the Laves or Heusler phases, have provided the most promising outlook for improving the creep resistance to date [1].

#### Polyphase in-situ composites

One of the most promising approaches to improving the mechanical behavior of NiAl alloys is through in-situ eutectic composites. While eutectic alloy phases are usually thermodynamically compatible up to the melting point, volume fraction and phase morphology are not completely free variables. Typical processing of these alloys involves casting, extrusion, or directional solidification. Casting and extrusion are limited by the varying morphology within the final structure. Directional solidification appears to be the most likely choice of processing technique to develop composites with oriented structures and properties.

Czochralski and Bridgman techniques have shown success, but impurities are often introduced from crucibles [53-56]. To avoid this contamination, a containerless

means of directional solidification is required. At the University of Tennessee, Oliver, *et al*, have developed containerless methods involving induction heating and melting within a controlled environment. The induction heating generates a liquid zone and partially constrains and levitates the liquid. The dimensions and position of the molten zone are computer controlled promoting stable growth and microstructure control of the freezing ingot. A detailed discussion of the equipment and its operation is presented elsewhere [2, 3, 42, 56, 57].

In-situ composites require phase constitution information which is limited or nonexistent for many possible ternary and quaternary systems. Table 1 provides a summary of interesting systems recently explored at the University of Tennessee [2, 3, 58, 59, 60]. Included within Table 1 are the compositions, melting points, phases present, morphology, and metallic volume fractions of the eutectic systems. These eutectics include two and three phase structures. In the majority of the alloys listed, the NiAl is the matrix with either a refractory metal and/or an intermetallic phase acting as a reinforcement.

Containerless directional solidification of these alloys produced significant results. Figure 4 is a plot of room temperature fracture toughness versus 1300 K creep strength for the directionally solidified eutectic structures. A nickel-based superalloy (NASAIR 100) is included to illustrate a goal for new systems as defined by a currently used alloy. The upper temperature limit of engineering application for NASAIR 100 is near 1300 K. As may be observed, the in-situ composites achieve a notable improvement of properties over NiAl. The NiAl-15Ta eutectic alloy illustrated creep strength comparable to that of the nickel superalloy, while the other eutectic systems have shown a distinct improvement over single crystal NiAl [001]. Although the toughness values for the in-situ composites fall far short of the best current superalloys,

Table 1: Characterization of NiAl-based eutectics directionally solidified by containerless means at the University of Tennessee.

Eutectic Composition, at%	Melting Point, K	Phases	Morphology	Volume Fractions	Density, [58] g/cm <sup>3</sup>	Refs.
NiAl-40V	1633	NiAl V	Matrix Lamellae	0.50 0.50	5.93	3
NiAl-34Cr	1723	NiAl Cr	Matrix Rod	0.66 0.34	6.36	2
NiAl-28Cr-6Mo	1723	NiAl (Cr, Mo)	Matrix Lamellae	0.66 0.34	6.57	2
NiAl-9Mo	1778	NiAl Mo	Matrix Rod	0.89 0.11	6.39	3
NiAl-15.5Ta	1833	NiAl NiAlTa	Matrix Lamellae	0.53 0.47	8.34	2
NiAl-16.5Nb	1710	NiAl NiAlNb	Lamellae Matrix	0.47 0.53	6.51	59
Ni-42Al-12.5Ta-7Mo	1800	NiAl NiAlTa (Mo, Ta)	Matrix Lamellae Rod	0.57 0.33 0.10	7.99	2
Ni-30.5Al-33Cr-6Ta	1698	NiAl (Cr,Al)NiTa Cr	Matrix Lamellae Rod	0.40 0.25 0.35	7.25	2
Ni-28.5Al-33V-10Ta	1578	NiAl NiAlTa V	Matrix Blade Rod	0.24 0.32 0.44	7.41	2
NiAl-33.3Cr-11.1Nb	1633	NiAl (Cr,Al)NbNi Cr	Lamellae Matrix Rod	?	6.67	60
NiAl-15Zr-15V	1494	NiAl Ni <sub>2</sub> AlZr V <sub>2</sub> Zr	Matrix Lamellae @ Interface	0.49 0.35 0.16	6.07	3

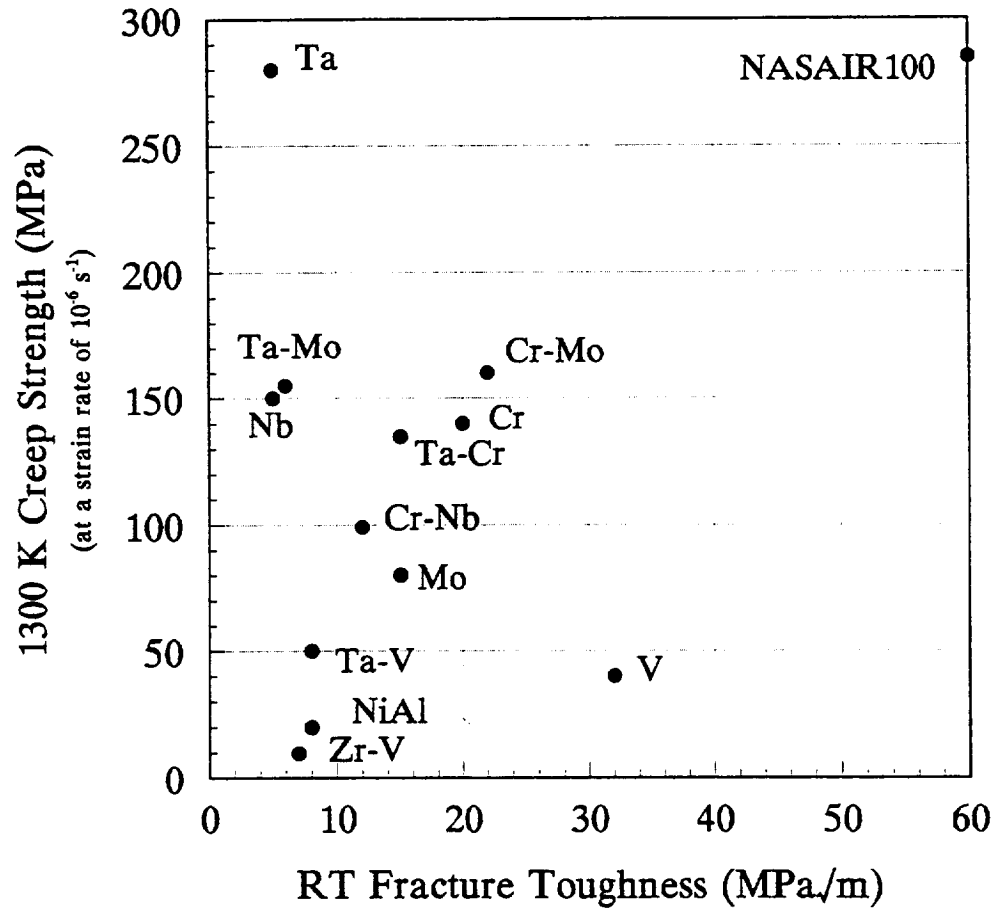


Figure 4: Performance plot of various NiAl-based eutectic systems directionally solidified at the University of Tennessee, modified from [24].

the increases are significant enough to warrant further investigations since the microstructures were not optimized during directional solidification.

The polyphase eutectic composites are among the most interesting of the those studied to this point. For example, in the NiAl-NiAlTa-Cr eutectic, the microstructure consists of an NiAl matrix containing Cr rods with laths of NiAlTa. While the NiAl matrix tends to be brittle at room temperature with poor creep strength, the Cr acts as a ductile reinforcement and the Laves phase acts as a creep strengthener. As seen from Figure 4, this alloy exhibits significant increases in room temperature fracture toughness and creep strength. The other polyphase eutectic systems also exhibit similar results but by different means (see Table 1 and Figure 4) [2, 3].

The eutectic structures studied show significant improvements over binary NiAl while maintaining many of the properties which originally attracted researchers. While the oxidation resistance and thermal conductivity are little affected in many of the systems, the density and melting points can become critical issues. Figure 5 is a plot of specific creep strength (creep strength/density) versus room temperature fracture toughness. Comparison of Figure 4 to Figure 5 reveals that many of the eutectic systems appear more attractive when density is considered. Although NiAl has an extremely high melting point, many of the eutectic temperatures are lower and hence the creep tests are not a constant fraction of the eutectic temperature.

### Carbides

Recent interest has been placed on developing NiAl-based eutectic systems with a density comparable to that of stoichiometric NiAl. The compounds formed by the interstitial elements appear as likely sources. The borides, carbides, nitrides, and oxides are stable, high temperature compounds, some with low densities compared to

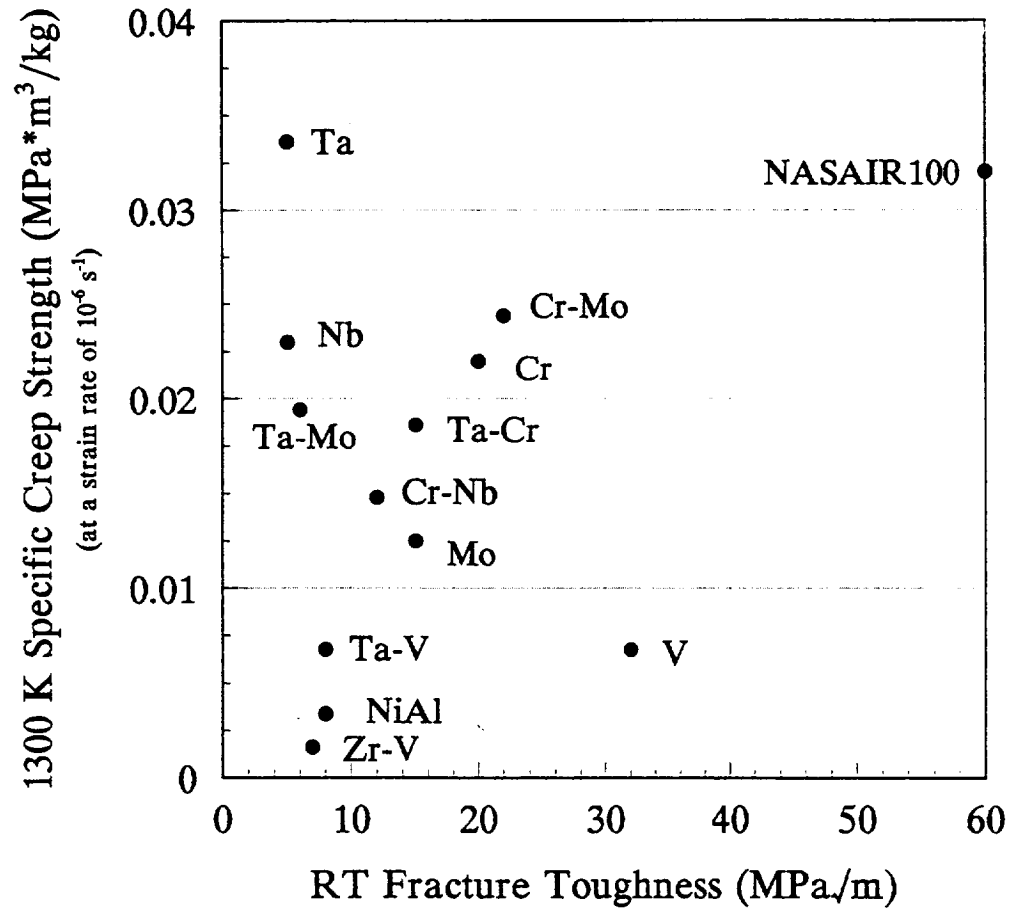


Figure 5: Density adjusted performance plot of various NiAl-based eutectic systems directionally solidified at the University of Tennessee, modified from [3].

pure refractory metals. The carbides are particularly interesting due to their high melting temperatures and attractive mechanical properties.

The limited availability of literature based upon NiAl-carbide systems prevents adequate discussion. Some investigation has been made into the Ni-Al-C and Ni-Al-Ti-C systems, but only limited phase constitution information was provided [61, 62]. Therefore, this section will concentrate on the physical and mechanical properties of various refractory metal carbides. Table 2 provides a summarization of a selection of carbides along with various physical and mechanical properties [63, 64]. As may be observed, the carbides have high melting points, some with low densities, high hardness, and high elastic moduli. They also have good thermal stability and high temperature strength. The "cemented carbides," combinations of carbides with binder materials such as cobalt and nickel, are mass produced for use as tool materials and wear resistant parts [4].

While the binary phase diagrams for the individual systems tend to be well known, little constitutional information is available on their interaction with NiAl in more complex systems. This study examines NiAl-based carbide systems with a priority placed upon lower density structures and polyphase eutectics.

Table 2: Selected physical and mechanical properties of various refractory metal carbides, summarized from [63, 64].

Carbide	Structure	Density, g/cm <sup>3</sup>	Melting Point, K	Microhardness, kgf/mm <sup>2</sup>	Elastic Modulus, kgf/mm <sup>2</sup>
TiC	Cubic	4.93	3530	2850 ± 40	32000
ZrC	Cubic	6.73	3803	2925 ± 184	35500
HfC	Cubic	12.67	4163	2913	35900
VC	Cubic	5.48	2921	2094	27600
NbC	Cubic	7.82	3886	1961	-
Nb <sub>2</sub> C	Hex.	7.85	3308	2123 ± 199	-
Ta <sub>2</sub> C	Hex.	15.04	3603	1714 ± 159	-
TaC	Cubic	14.4	4258	1599 ± 49	-
Cr <sub>23</sub> C <sub>6</sub>	Cubic	6.98	1791	1650	-
Cr <sub>7</sub> C <sub>3</sub>	Rhomb.	6.97	2055	2200	-
Cr <sub>3</sub> C <sub>2</sub>	Rhomb.	6.74	2168	2280	38000
α-MoC	Cubic	8.88	2873	-	-
Mo <sub>2</sub> C	Hex.	9.18	2753	1479 ± 24	22100
WC	Hex.	15.77	3058	923	72200
β-W <sub>2</sub> C	Cubic	17.34	3068	3000	42800
Fe <sub>3</sub> C	Rhomb.	7.69	1923	-	-

## CHAPTER 2

### ALLOY DEVELOPMENT

#### Introduction

With the limited ternary and quaternary information available in most systems, the identification of new eutectic systems required exploratory melts to determine the phase constitution information. Although there has been some investigation into computer generation of phase diagrams from thermodynamic values, experimental evaluation is still the most reliable source of information. Initially, several NiAl-X-C systems were investigated as potential candidates due to the stability of the carbides formed during solidification (where X = refractory metal). Systems investigated include Cr, Co, Fe, Hf, Mo, Nb, Ta, Ti, W, and Zr.

#### Experimental Procedures

##### Arc-melted ingots

New NiAl-based systems were examined using an arc-melter with a controlled gas system. High purity Al, Ni, and C were reacted with a refractory metal on a water-cooled copper hearth in a flowing argon atmosphere. Melting was achieved with a non-consumable tungsten electrode controlled by a 400 amp welder. Ingot size varied from 10 to 25 grams. Initially, all components were reacted simultaneously. In subsequent ingots, high purity C was reacted with the Ni prior to reaction with the other components. Each ingot was also melted at least 4 times and turned over between each melting to encourage homogeneity. A zirconium charge was melted prior to and after each melting to reduce the amount of impurity pickup. In an effort to maintain a

density near that of NiAl, refractory metal and carbon additions were limited to less than 5 atomic percent.

### Metallography

Arc-melted ingots were sectioned using a high speed, water cooled abrasive cut-off wheel. Sectioned samples were metallographically polished and etched with a 90 vol. % H<sub>2</sub>O, 5 vol. % HNO<sub>3</sub>, 5 vol. % HF solution. Optical microscopy was used to explore the presence of eutectic microstructure within each ingot.

### **Results**

Initial melts in which all components were reacted simultaneously were not successful. Difficulty arose in completing the dissolution of carbon. Reacting the carbon with the nickel prior to combination with the other components proved a successful route. For higher melting elements, such as Ta and W, complete reaction of the refractory metal was also not always achieved. Alternatively, melting these high temperature components with the aluminum prior to reaction with the Ni-C pellets proved successful. Limited metallography performed on partially reacted ingots proved beneficial to composition and refractory metal selection for later ingots. All further results are based on completely reacted melts.

In comparison to other systems examined by the author, the NiAl-X-C systems exhibited a high fluidity of the liquid. Other systems, such as stoichiometric NiAl, NiAl-9Mo, NiAl-34Cr, and NiAl-33.3Cr-11.1Nb, were not as severely affected by the force generated by the arc. The systems containing carbon flowed much more readily under similar conditions (ingot size, argon flow rate, and control current).

Two types of characteristic structures were observed in the NiAl-X-C systems: "coarse", sometimes faceted, particles and "fine" interdendritic two-phase constituent.

Figure 6 is a collection of optical micrographs for systems which produced coarse particles within the cast structure, while Figure 7 contains representative micrographs for systems containing the fine interdendritic, two-phase structures.

### Discussion

As observed by the micrographs in Figure 6 and 7, many of the systems contain coarse, cube-like particles, a fine interdendritic structure, or a mixture of the two. Although some of the fine microstructures appear promising, the ones containing large cube-like particles do not. The presence of the cube-like particles was not totally unexpected. The particles are most likely carbides, but no specific test was performed for verification. Table 3 contains representative reactions and free energies of formation for possible carbides within the systems investigated. These values are plotted in Figure 8. Refractory metals which produce extremely stable carbides (HfC, NbC, TaC, WC, and ZrC) also formed the blocky or cube-like particles observed in Figure 6. These particles are most likely carbides which formed from the liquid state and were randomly distributed throughout the structure as the ingot froze.

Several of the systems do show potential. The NiAl-Mo-C, NiAl-Cr-C, and the NiAl-Co-C systems all contain what appears to be an interdendritic "eutectic" structure. Attempts to improve the volume fraction of the "eutectic" constituent within the chromium or cobalt systems by varying the melt compositions proved unsuccessful. However, the molybdenum system did exhibit changes in volume fraction of the interdendritic two-phase structure.

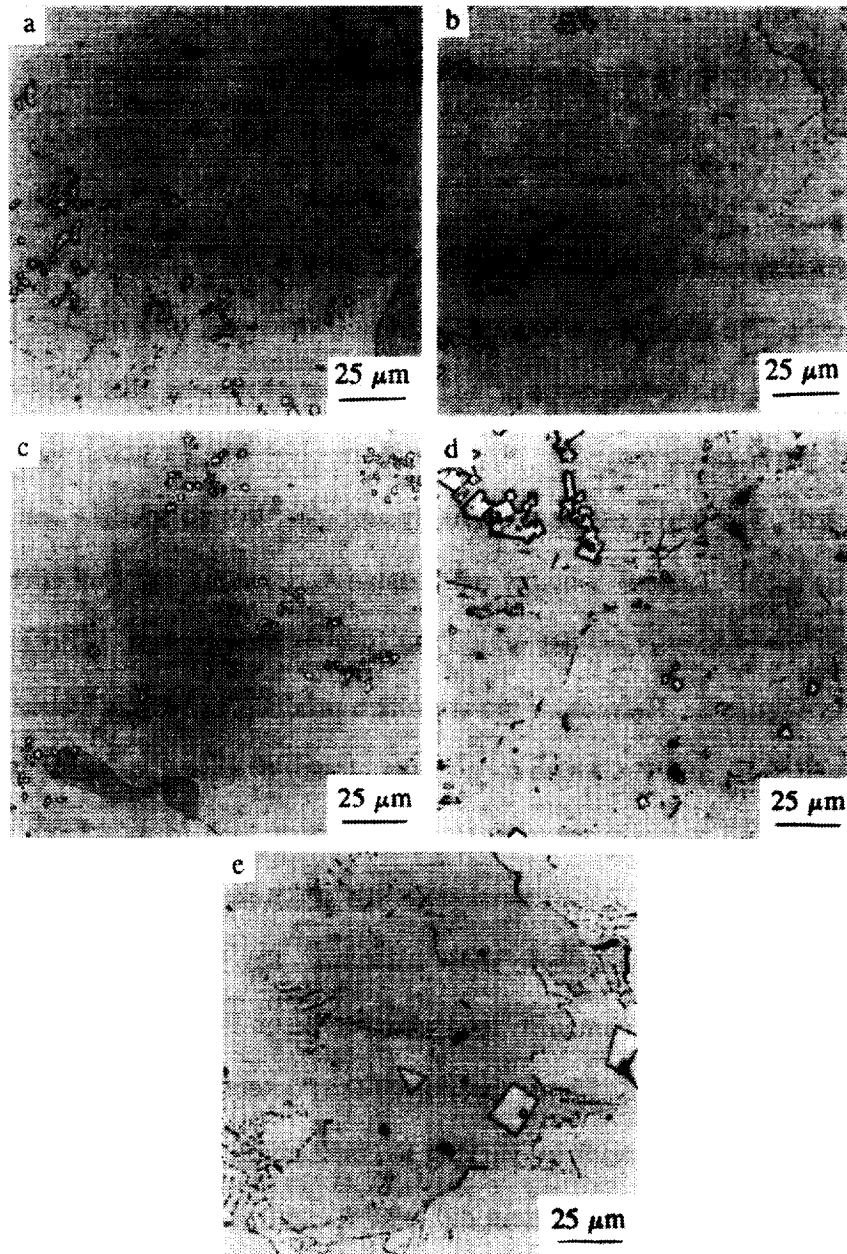


Figure 6: Light optical micrographs of NiAl-refractory metal-carbon arc-melts (all in at. %): (a) NiAl-1Nb-1.02C, (b) NiAl-0.97Hf-1C, (c) NiAl-1Ta-1C, (d) NiAl-2Ti-2.04C, and (e) NiAl-1.95Zr-1.81C.

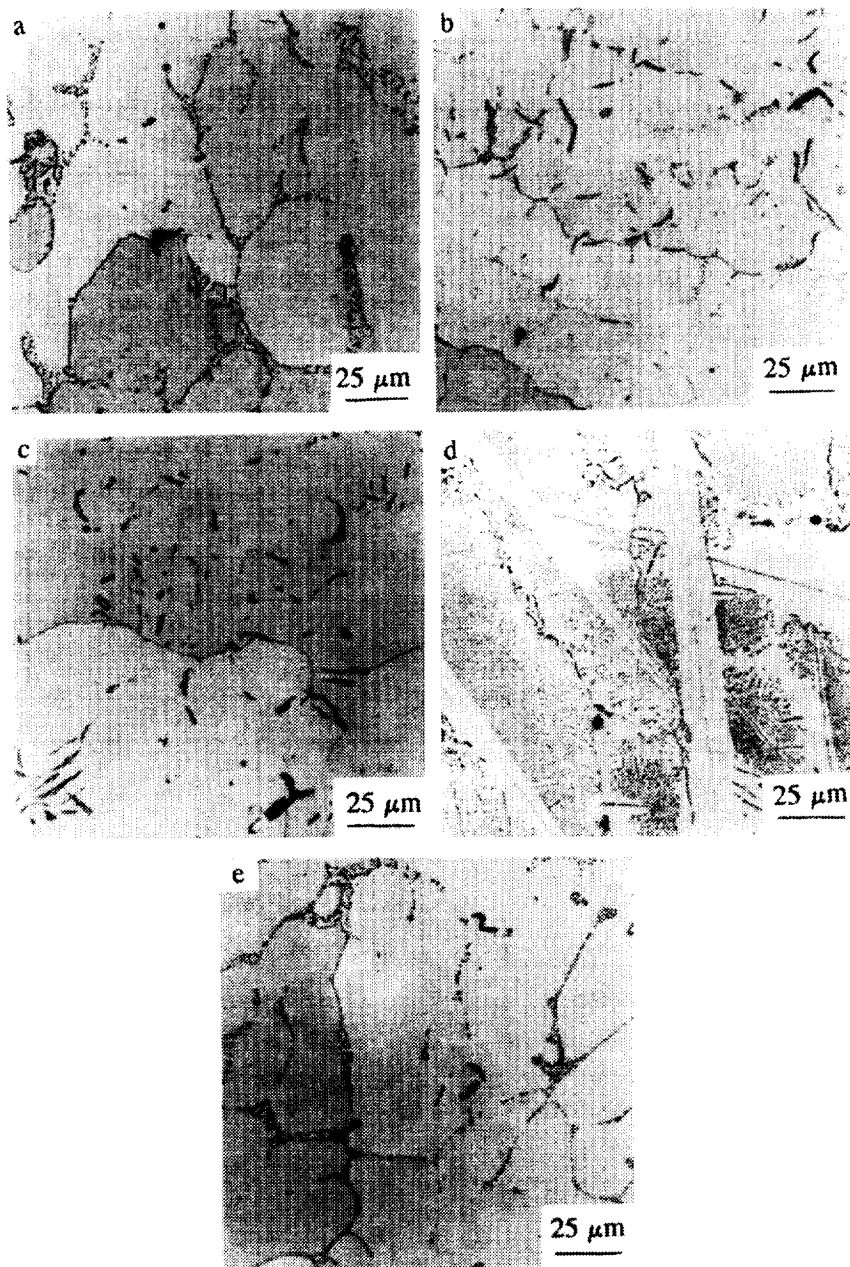


Figure 7: Light optical micrographs of NiAl-refractory metal-carbon arc-melts (all in at. %): (a) NiAl-0.76Co-1.05C, (b) NiAl-1.02Cr-0.97C, (c) NiAl-0.99Fe-1.05C, (d) NiAl-1Mo-1C, and (e) NiAl-0.7W-1.05C.

Table 3: Free energy of formation for several carbides, summarized from [63].

Carbide	Reaction	Free Energy, cal/mol	Temp. Range, K
TiC	Ti + C = TiC	-43750 + 2.41 T -44600 + 3.16 T	298-1155 1155-2000
ZrC	Zr + C = ZrC	-44100 + 2.2 T	298-2200
HfC	Hf + C = HfC	-48500 + 3.262 T	298-2600
NbC	Nb + C = NbC	-33980 - 5.64 T log T + 17.79 T + 0.927*10 <sup>-3</sup> T <sup>2</sup> + 0.49*10 <sup>-1</sup> T <sup>-1</sup>	298-1800
TaC	Ta + C = TaC	-33497 + 1.332 T	298-3000
Cr <sub>23</sub> C <sub>6</sub>	23/6 Cr + C = 1/6 Cr <sub>23</sub> C <sub>6</sub>	-16380 - 1.54 T	973-1273
Cr <sub>7</sub> C <sub>3</sub>	7/27 Cr + C = 23/27 Cr <sub>7</sub> C <sub>3</sub>	-10050 - 2.85 T	298-1673
Cr <sub>3</sub> C <sub>2</sub>	3 Cr + 2 C = Cr <sub>3</sub> C <sub>2</sub>	-8550 - 5.03 T	298-2171
Mo <sub>2</sub> C	2 Mo + C = Mo <sub>2</sub> C	-6700 -11700 - 1.83 T	298-1273 1200-1340
WC	W + C = WC	-9100 + 0.4 T	298-2000
Fe <sub>3</sub> C	3 Fe + C = Fe <sub>3</sub> C	+6200 - 5.56 T +6380 - 5.92 T +2475 - 2.43 T	298-463 463-1115 1115-1808
Co <sub>3</sub> C	3 Co + C = Co <sub>3</sub> C	-395 + 1006 T log T - 3.43 T	298-1273

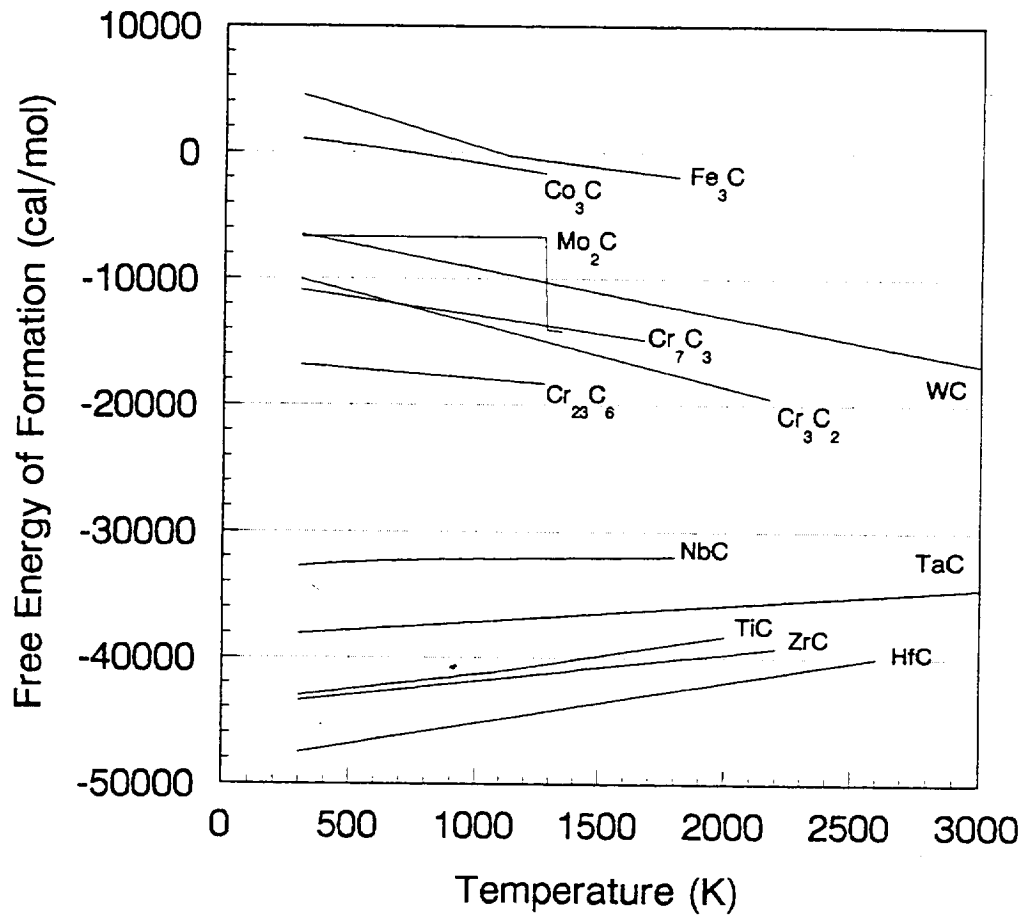


Figure 8: Plot of free energy of formation versus temperature for various refractory carbides [plotted from data in Table 3].

## CHAPTER 3

### PROCESSING OF NiAl-Mo-C ALLOYS

#### Introduction

Initial results from the exploratory melts revealed that the NiAl-Mo-C alloys had the most promising microstructures of those examined. Although a eutectic-like microstructure was present interdendritically, the optimum composition was unknown. With very little phase constitution information available in this system, a decision was made to process numerous compositions in an effort to determine some of this information.

As discussed previously, some difficulties were experienced in the arc-melting of the NiAl-carbide alloys. Although arc-melting remained the simplest and easiest method of producing a large number of small ingots, several other approaches to processing were explored and evaluated.

#### Experimental Procedures

##### Arc-melting

Selected compositions were prepared by arc-melting high purity Ni, Al, Mo, and C on a water-cooled copper hearth in an argon atmosphere. Ingots were prepared by reacting the Ni with C prior to reaction with the other components. Homogeneity was promoted by melting the reacted ingot at least 4 times. Ingot size varied from 10 to 25 grams.

Selected compositions were further evaluated by heat treatments at elevated temperatures. Ingots were sectioned and encapsulated in silica glass in a reduced pressure argon atmosphere. Argon pressures were calculated for the annealing

temperature of 1473 K. Encapsulated specimens were annealed in a high temperature tube furnace for 24 hours. The mass of each sample was recorded before and after annealing. Observations were also made for oxidation behavior and general appearance.

### Slow cooling

Due to the fine structure and rapid cooling rates observed in arc-melted samples, another technique was incorporated to produce conditions closer to equilibrium. To ensure complete reaction, the Ni and C were reacted by means of arc-melting. These Ni-C ingots were then reacted with the Al and Mo in a high purity alumina crucible by induction melting in a 0.05 MPa helium atmosphere. Solidified melts were allowed to slowly cool. Ingot size was limited to approximately 55 grams by the use of these crucibles. To produce larger melts, a stabilized zirconia crucible was employed.

Specific compositions were sectioned and annealed within an induction furnace in a helium atmosphere of 0.05 MPa. Annealing temperatures were measured using an optical pyrometer. Various annealing times were used depending upon the measured temperature. Although most annealed specimens were furnace cooled, attempts were made to rapidly quench a specimen into a bath of water cooled diffusion pump oil.

### Containerless directional solidification

Before directional solidification could be performed, a series of cast precursor ingots were prepared. All precursor ingots were prepared by induction melting in a helium atmosphere and chill cast into copper molds at either the University of Tennessee-Knoxville (UTK) or NASA Lewis Research Center (NLRC). At NLRC, all components were reacted simultaneously. As with the slow cooled ingots previously

discussed, precursor ingots from UTK were prepared by combining the Ni and C by arc-melting prior to reaction with the other components. The copper molds also differed in diameter. NLRC molds were 1" diameter, while UTK molds were 0.875" diameter. Precursor ingots from NLRC were chemically analyzed for carbon on a Simultaneous N/O Determinator, Leco Corporation, Model TC-244, prior to processing. All precursor ingots received surface grinding before directional solidification.

Directional solidification of all ingots was achieved by a containerless electromagnetically levitated zone process. The ultimate goal during processing was to maintain a uniform ingot diameter and a steady state microstructure. The system utilizes induction power to melt, levitate, and constrain a liquid zone. A schematic of the liquid zone along with possible control actions is presented in Figure 9. In summary, the position and shape of the liquid zone is controlled by two major actions: induced power and stretch/squeeze. The induced power controls the location of the solid-liquid interface with the coils, while the stretch/squeeze controls the diameter and shape of the liquid zone. These values are maintained at target values by proportional, integral control loops. In addition, the temperature near the solid-liquid interface is measured using an infrared pyrometer. A detailed description of the equipment setup, process control variables, and other pertinent information is presented elsewhere [2, 3, 65, 66].

In an effort to increase the amount of carbon in certain ingots, a partial pressure of methane ( $\text{CH}_4$ ) was added to the high purity helium typically used. At elevated temperatures, the methane should reduce to hydrogen gas and graphite. Since the majority of the internal surfaces are water cooled to prevent oxidation or reaction, the methane should reduce at the hottest location: the liquid zone. Two techniques were incorporated. The first technique used a stagnant atmosphere of high purity helium at

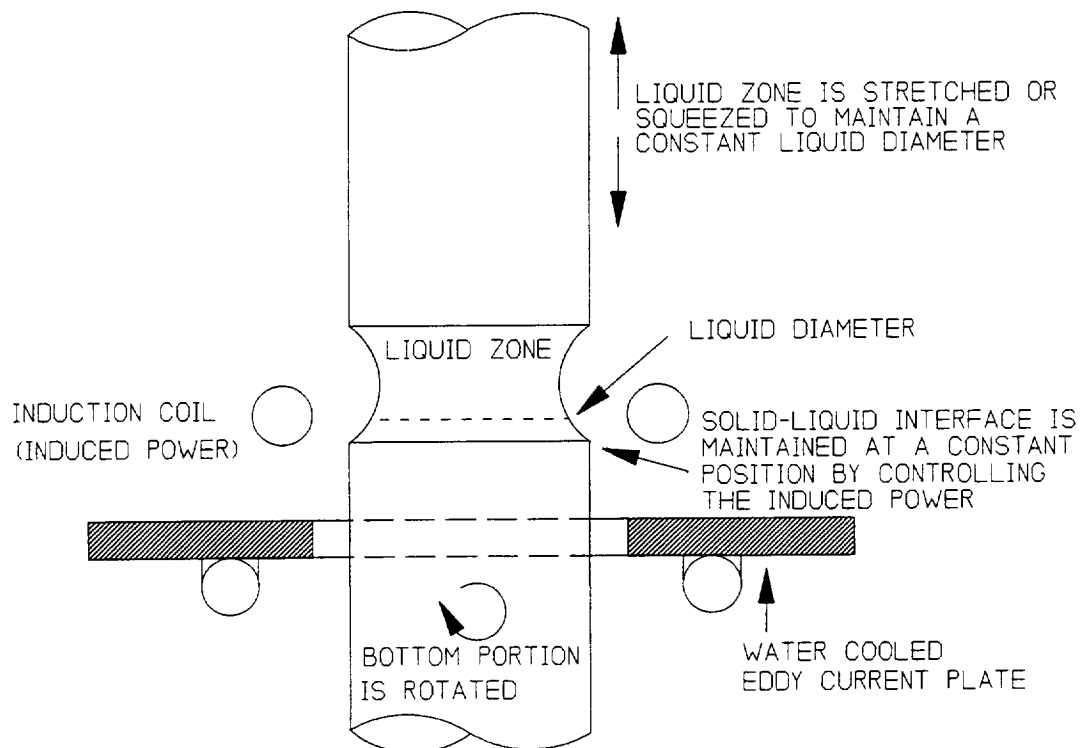


Figure 9: Schematic of a molten zone during directional solidification [2, 65].

0.05 MPa. After the liquid zone had been established, a mixture of 95 vol. % He/5 vol. % CH<sub>4</sub> was added until the chamber pressure was 0.11 MPa. The second technique established the liquid zone in a 100% high purity helium atmosphere at 0.11 MPa. The mixture of 95 vol. % He/5 vol. % CH<sub>4</sub> was then flowed through the processing chamber at a rate of 51 liters/hr.

Carbon dots were painted onto the surface of one precursor ingot prior to directional solidification. During processing, the carbon dots would eventually come in contact with liquid at the solid-liquid interface. At this point, the carbon should go into solution without interrupting control of the liquid zone. The carbon paint was prepared by mixing graphite powder with methanol to a "medium" thickness. The ingot was then processed in a high purity helium atmosphere at 0.11 MPa. All remaining precursor ingots were processed in a high purity helium atmosphere at approximately 0.11 MPa. After directional solidification, observations were made about the appearance of each ingot and optical macrographs were taken. Processing records were then evaluated and printed in hard copy form.

## Results

### Arc-melting

A summary of the various compositions investigated within the NiAl-Mo-C system by arc-melting is presented in Figure 10. Compositions were also prepared along the pseudobinaries of NiAl-Mo and NiAl-C to verify the results of literature work. At lower compositions of carbon (generally less than 3 at. %), no difficulties were observed in processing other than those discussed previously. However, at higher carbon contents, it became more difficult to react the carbon completely with the nickel. Compositions evaluated by heat treatment are also shown in Figure 10.

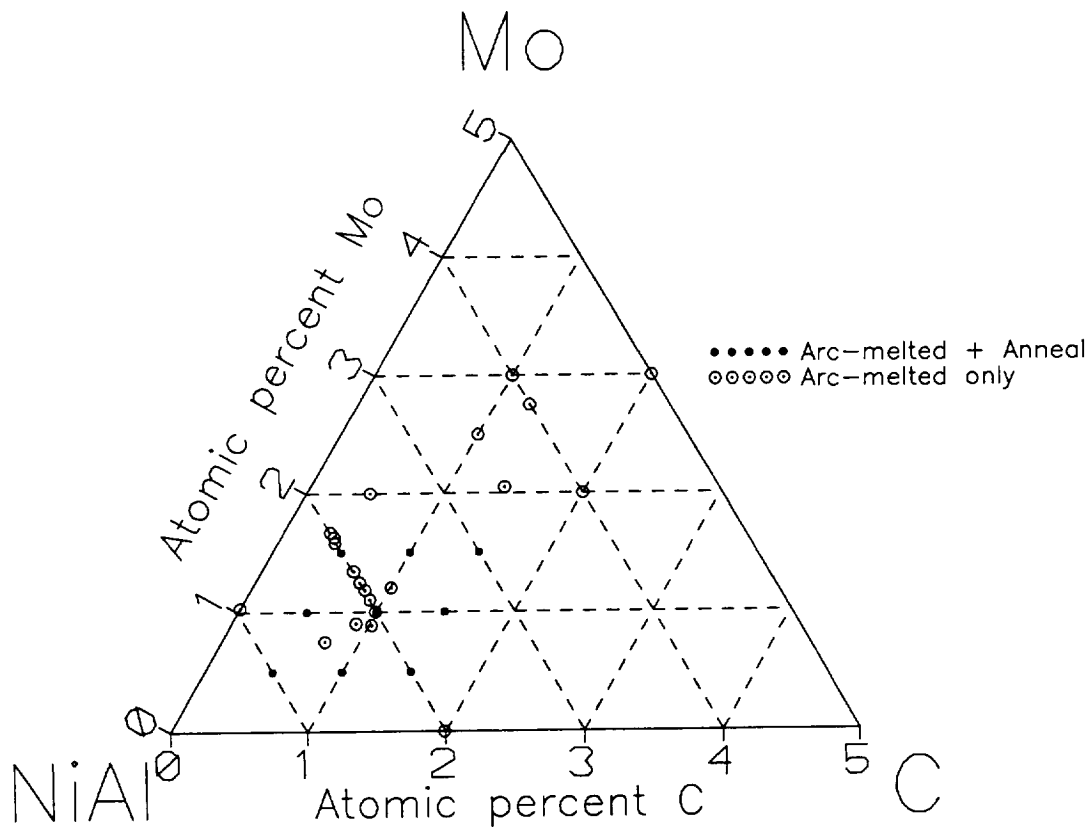


Figure 10: Compositions of arc-melts made in the NiAl-rich corner of the NiAl-Mo-C system.

Although heat treated specimens exhibited limited oxidation, only small changes in mass were observed.

### Slow cooling

Table 4 provides a summary of compositions and relative ingot size cast by induction melting. Initially, recrystallized alumina crucibles were recycled between melts. However, Ingots SC-3 and SC-4 experienced higher levels of porosity within the castings. This was originally thought to be due to the higher levels of carbon present in these ingots or to possible contamination from the argon or helium gas cylinders. Both proved incorrect. Ingot SC-4 appeared to have reacted with the alumina crucible. By switching to a new crucible between melts, this problem was eliminated. All melts except one, Ingot SC-7, were performed in alumina crucibles. This ingot was sent to NLRC for sectioning and further experimental investigation. Results revealed a large shrinkage cavity at the center of the ingot.

Heat treatments were performed on sections of ingot SC-2 (NiAl-1Mo-1C). Temperatures of 1603 and 1723 K were measured using a radiation optical pyrometer. Measurements were performed at fifteen minute intervals. Annealing times were 3 hours with a furnace cool. In addition, a section was annealed at 1623 K for 6 hours with a furnace cool. Quenching of one specimen in a cooled bath of diffusion pump oil were unsuccessful. Further examination by metallography was required.

### Containerless directional solidification

A summary of the precursor ingots is presented in Table 5. Included are the composition, casting location, carbon analysis (if appropriate), and processing method for each ingot. In the precursor ingots cast at NLRC, all of the carbon did not react completely with the other components. Chemical analysis revealed that the

Table 4: Slow cooled ingots prepared by melting within an induction furnace at 0.05 MPa helium.

Ingot #	Composition, at. %	Crucible Type	Mass of Melt, g
SC-1	NiAl-2Mo-2C	RC Al <sub>2</sub> O <sub>3</sub> <sup>a</sup>	34.83
SC-2	NiAl-1Mo-1C	RC Al <sub>2</sub> O <sub>3</sub> <sup>a</sup>	49.49
SC-3	NiAl-2Mo-2C	RC Al <sub>2</sub> O <sub>3</sub> <sup>a</sup>	56.69
SC-4	NiAl-2Mo-2C	RC Al <sub>2</sub> O <sub>3</sub> <sup>a</sup>	50.10
SC-5	NiAl-3Mo-1C	RC Al <sub>2</sub> O <sub>3</sub> <sup>a</sup>	50.58
SC-6	NiAl-1Mo-3C	RC Al <sub>2</sub> O <sub>3</sub> <sup>a</sup>	50.69
SC-7	NiAl-1Mo-1C	S ZrO <sub>2</sub> <sup>b</sup>	≈400

<sup>a</sup> Recrystallized alumina

<sup>b</sup> Stabilized zirconia

Table 5: Precursor ingots prepared at the University of Tennessee-Knoxville (UTK) and NASA Lewis Research Center (NLRC) with containerless directional solidification processing conditions.

Ingot #	Composition, at. %	Location	C Analysis <sup>a</sup> , at. %	Processing atmosphere	Successful, Yes/No	Figure #
NiAl-Mo #1	NiAl-1Mo	NLRC	0.024	He/CH <sub>4</sub> <sup>b</sup>	Yes	11
				He/CH <sub>4</sub> <sup>c</sup>	No	12
MoC #1	NiAl-1Mo-xC	NLRC	0.59	He/C Dots <sup>d</sup>	No	13
MoC #2	NiAl-1Mo-xC	NLRC	0.61	He <sup>e</sup>	Yes	14(a)
MoC #3	NiAl-1Mo-xC	NLRC	0.73	He <sup>e</sup>	Yes	14(b)
MoC #4	NiAl-1Mo-1C	UTK	-	He <sup>e</sup>	No	16
MoC #5	NiAl-1Mo-1C	UTK	-	He <sup>e</sup>	No	-
MoC #6	NiAl-1Mo-1C	UTK	-	He <sup>e</sup>	No	-

<sup>a</sup> Analysis performed on a Simultaneous N/O Determinator. LECO Corp. Model TC-244,  $\pm 10\%$

<sup>b</sup> Stagnant atmosphere of 95 vol. % He/5 vol. % CH<sub>4</sub> mixed with high purity He at 0.05 MPa pressure to a total pressure of 0.11 MPa.

<sup>c</sup> Flowing atmosphere of 95 vol. % He/5 vol. % CH<sub>4</sub> at 51 liters/hr into a 100% high purity He atmosphere at 0.11 MPa pressure.

<sup>d</sup> Stagnant atmosphere of He at 0.11 MPa pressure with graphite dots painted on surface of precursor ingot.

<sup>e</sup> Stagnant atmosphere of high purity He at 0.11 MPa pressure.

compositions varied between 0.59 and 0.73 at. % carbon, while the attempted compositions were 1 at. % carbon. All other cast precursor ingots were determined to be of the calculated compositions.

Attempts at adding carbon to the liquid zone during containerless directional solidification proved unsuccessful. The original technique using a stagnant He + He/CH<sub>4</sub> atmosphere initially appeared successful on Ingot NiAl-Mo #1. Figure 11 is an optical macrograph of the directionally solidified (DS) ingot. The original composition contained almost no carbon (see Table 5), thus any changes would be apparent microstructurally. It was later revealed that almost no carbon was added to the DS ingot. In an effort to increase the partial pressure of methane, a mixture of He/CH<sub>4</sub> was flowed through the high purity He with the zone already established on the previously DS material. The directional solidification process was operating smoothly until a heavy coating developed upon the surface of the liquid zone. This "film" is shown in Figures 12(a) and (b) on the DS ingot. At this point, the liquid zone also began to freeze. Efforts to remelt the liquid zone were unsuccessful.

With the methane atmosphere ineffective, graphite dots were placed directly on the surface of a precursor ingot already containing carbon (Ingot MoC #1). The dots were placed randomly across the surface of the ingot. Although the zone was established without difficulty and a small section was directionally solidified, the graphite spots would not go into solution as expected. Figure 13 is an optical micrograph of Ingot MoC #1 after processing.

With the failure of the in-situ reaction of graphite, the remaining ingots were directionally solidified in the as-cast condition within a high purity helium atmosphere. Figures 14 (a) and (b) are optical macrographs of Ingots MoC #2 (NiAl-1Mo-0.61C) and MoC #3 (NiAl-1Mo-0.73C). Although the directional solidification process for Ingot MoC #2 went smoothly without any difficult during processing, Ingot MoC #3

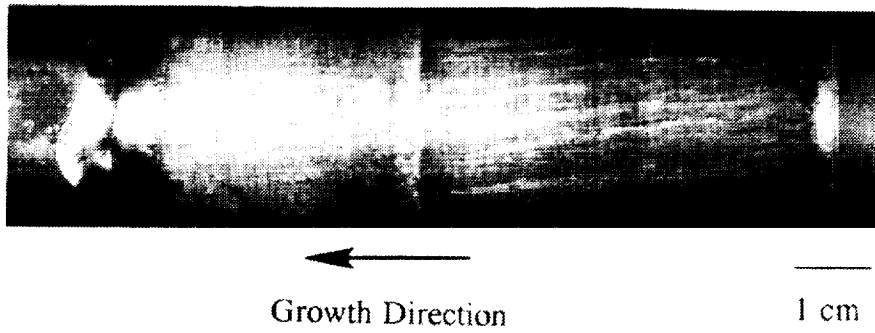


Figure 11: NiAl-1Mo precursor ingot directionally solidified in a stagnant atmosphere of methane and helium.

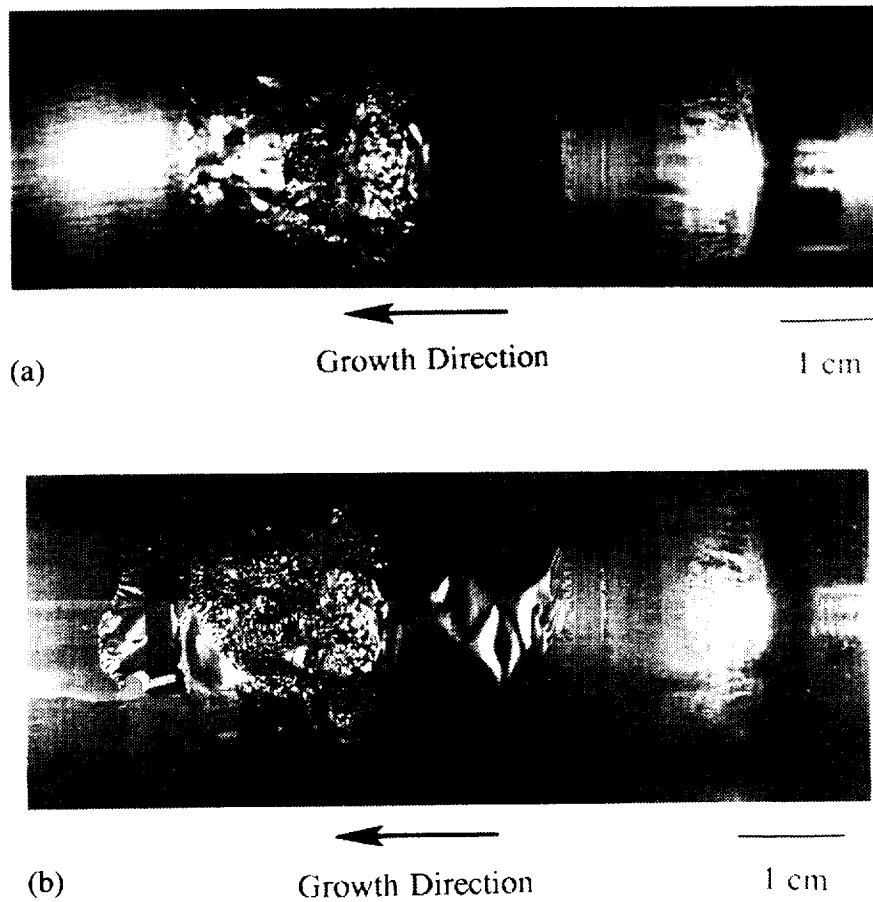


Figure 12: Directionally solidified NiAl-1Mo ingot processed in a flowing atmosphere of methane and helium with emphasis on (a) processed region and (b) deposited film.

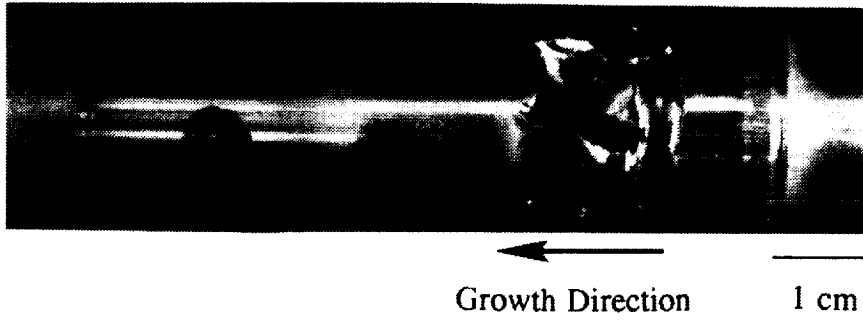


Figure 13: NiAl-1Mo-0.59C ingot with graphite dots on unprocessed region of the ingot.

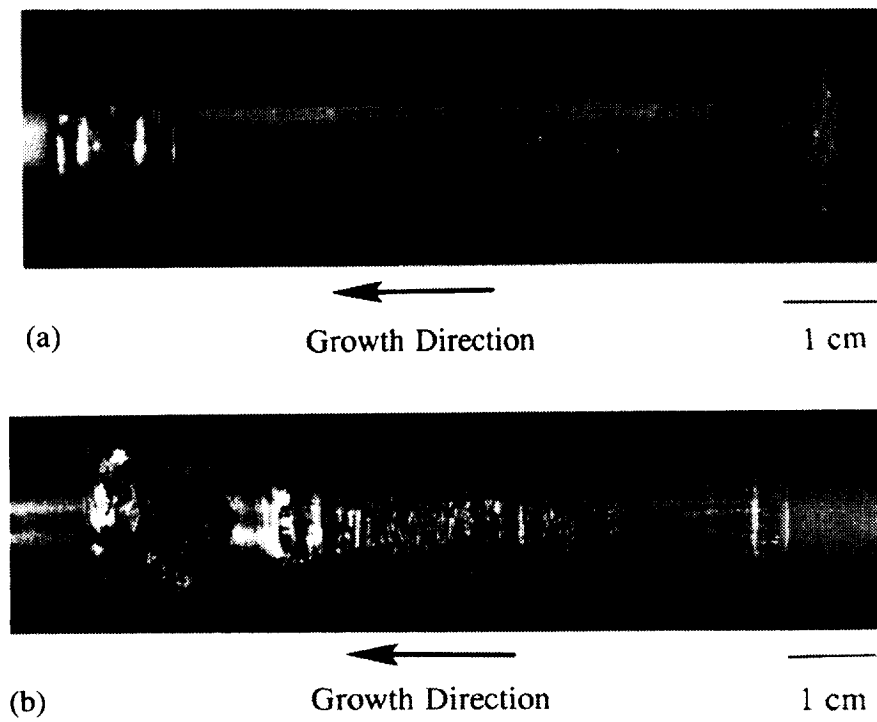


Figure 14: As processed, directionally solidified ingots of (a) NiAl-1Mo-0.61C and (b) NiAl-1Mo-0.73C.

developed an oscillatory behavior associated with precipitation on the liquid zone. Figure 15 is the melt record for Ingot MoC #3. As the precipitate would form on the liquid zone near the solid-liquid interface, the zone would begin to freeze. By increasing the induced power, the particles on the liquid surface went back into solution and the zone was maintained. As discussed previously, arc-melted compositions containing carbon exhibited a higher fluidity in the liquid state than other compositions. At such high power levels, the liquid zone became difficult to control and a spill was inevitable. The power was therefore reduced slightly, but again the precipitate began to form (Figure 15 (c)). Eventually, the precipitate coated the entire zone, which immediately froze, and stopped the directional solidification process.

The same experience was observed in the unsuccessful processing of Ingots MoC #4, MoC #5, and MoC #6, but occurred within a few minutes after formation of the liquid zone. Figure 16 is an optical macrograph of Ingot MoC #4 with the coated, frozen last zone visible. Although the directional solidification process failed within a short period of time, a limited amount of directionally solidified material was obtained. In all three ingots, the precipitate formed near the solid-liquid interface and spread toward the center of the molten zone. Increasing the power stopped the spread of the particles, but this action also produced more lift within the zone. With a higher viscosity than typical melts, this often produced a spill as seen in Figure 16.

### **Discussion**

The failed attempts to react carbon with the liquid zone during processing should not have been totally unexpected. In Ingot NiAl-1Mo #1, the partial pressure of methane was a constant low value in the first attempt but was increasing throughout directional solidification in the second attempt. At higher partial pressures of methane, the amount of graphite deposited upon the surface should have increased. Although no

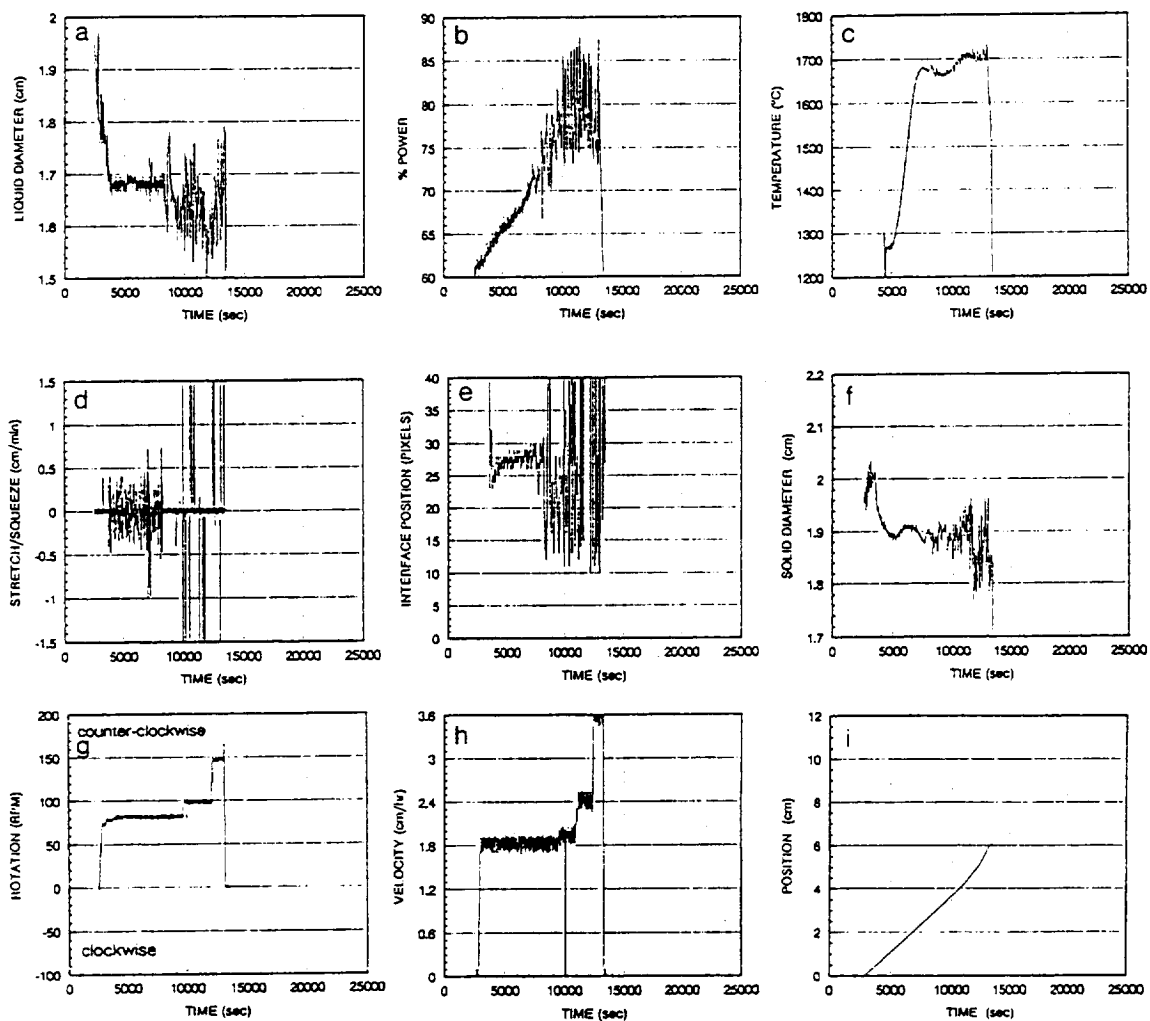


Figure 15: Melt record for NiAl-1Mo-0.73C directionally solidified ingot. Shown are (a) liquid diameter, (b) percent power, (c) temperature, (d) stretch/squeeze, (e) interface position, (f) solid diameter, (g) rotation, (h) velocity, and (i) relative ingot position.

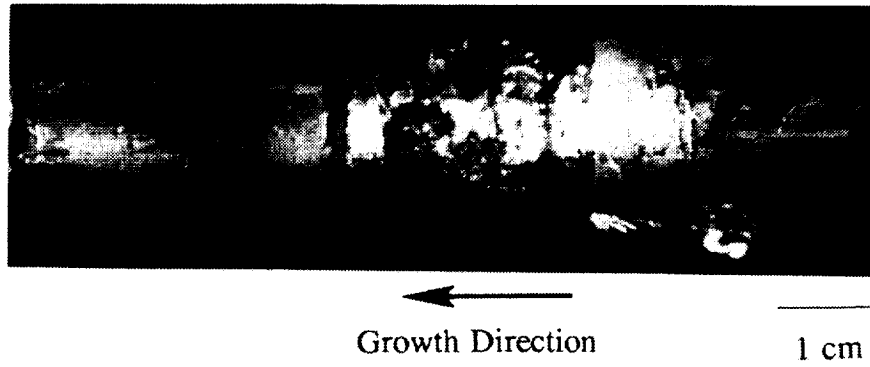


Figure 16: Failed directional solidification of an NiAl-1Mo-1C precursor ingot.

test were performed to verify the nature of the film, it was most likely a thin layer of graphite. With an emissivity of 0.81 or greater for carbon [67], a large portion of the power input into the layer would have been radiated outward. Therefore, increases in power to produce melting on the coated surface would have required more power than was available. In addition, the high emissivity of the graphite on Ingot MoC #1 prevented the anticipated local melting around the painted dots.

One factor involved in the directional solidification process was the size of the precursor ingots. As the diameter of the ingot decreased, the power required for melting and maintaining the liquid zone increased. In Ingots MoC #4 through MoC #6, the diameter was much smaller than in ingots MoC #2 and MoC #3. The higher power level associated with the smaller diameter also produced more levitation to the molten zone. In these ingots under these conditions, long zones with very poor control were typical and spills from the molten zone were common.

The precipitation effect on the liquid zone for Ingots MoC #3 through MoC #6 has been theorized to occur by one of two types of reactions. Both theories assume the presence of a pseudobinary phase relationship between NiAl and a carbide. The first theory is based on a eutectic reaction, while the second is based upon a peritectic reaction. These reactions are schematically illustrated in Figures 17 (a) and (b), respectively. Assuming the presence of an eutectic reaction, the composition of the ingot must be on the carbide-rich side of the eutectic composition. As the ingot melts, the composition of the liquid zone is assumed to be  $C_e$ . At the solid-liquid interface, the precipitation of carbide should occur.

Precipitation of the carbide could also be associated with a peritectic reaction as seen in Figure 17 (b). If the composition of the liquid zone is greater than  $C_1$ , then the carbide would precipitate from the molten zone at the solid-liquid interface. As with graphite, most carbides generally have high emissivity values (between 0.62 and 0.91).

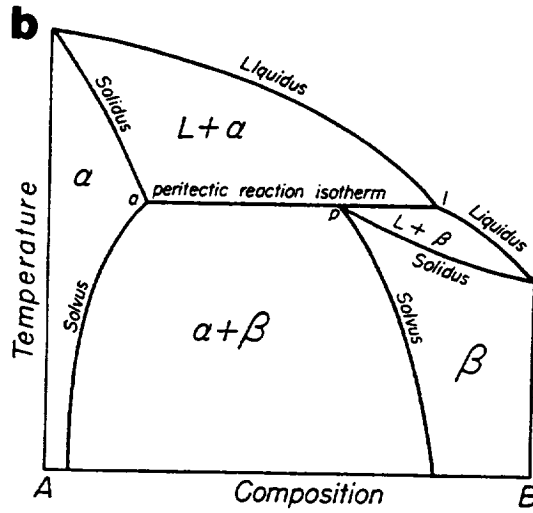
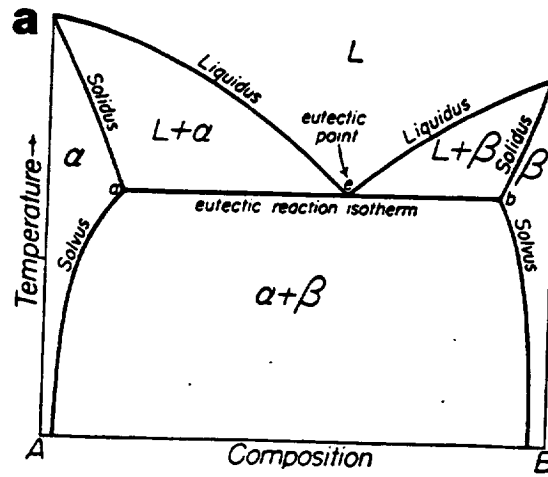


Figure 17: Schematic binary phase diagram for (a) eutectic reaction and (b) peritectic reaction.

For example,  $\text{Mo}_2\text{C}$  has an emissivity of 0.71 [63]. The carbides would behave similar to the graphite spots, requiring high power levels due to the emissivity. Further investigation by microstructural evaluation is required to clarify the precipitation behavior which occurs during directional solidification.

## CHAPTER 4

### MICROSTRUCTURES OF NiAl-Mo-C ALLOYS

#### Introduction

The various processing methods and compositions were evaluated by several techniques. Through the various methods of microscopy, the microstructures associated with a specific composition or technique were characterized. In addition, techniques such as differential thermal analysis and x-ray diffraction can help reveal phase relationships. By interpreting these results, only an imprecise comprehension of the phase constitution relationships and solidification behavior was determined for the NiAl-rich corner of NiAl-Mo-C system. Literature information pertaining to this region is generally not available. Limited information is available for the binary systems and the pseudo-binaries of NiAl-Mo and NiAl-C.

#### Experimental Procedures

##### Optical microscopy

Arc-melted, slow cooled, and heat treated ingots were sectioned, metallographically polished, and etched. Directionally solidified ingots were typically examined by grinding a flat on the surface of the bar with a high speed abrasive wheel. The ground section was then metallographically polished and etched. Ingots which froze or spilled during directional solidification were also sectioned and metallographically polished. All ingots, regardless of composition or processing technique, were etched with a 90 vol. % H<sub>2</sub>O, 5 vol. % HNO<sub>3</sub>, 5 vol. % HF solution. If appropriate, optical micrographs were taken at various magnifications.

### Scanning electron microscopy

Samples were sectioned, mounted in conductive bakelite, and metallographically polished. A number of samples were examined unetched, while the remaining specimens were etched with a 90 vol. % H<sub>2</sub>O, 5 vol. % HNO<sub>3</sub>, 5 vol. % HF solution. A voltage of 20 KeV was typically used while operating in either backscatter (BSE) or secondary (SE) electron collection mode on either a Cambridge Stereoscan 120 or 360 model scanning electron microscope (SEM). Energy dispersive spectroscopy (EDS) was used to determine the elements present within the microconstituents.

### Transmission electron microscopy

Samples were prepared by one of two techniques. Extraction replication was used to remove the compounds from the NiAl matrix [69, 70]. Arc-melted ingots #122 (NiAl-1.58Mo-0.41C) and #128 (NiAl-2.75Mo-1.24C) were sectioned and mounted in bakelite. Each specimen was then metallographically polished. Solution 1, a mixture of 5% nitric acid, 5% hydrofluoric acid, and 90% distilled water, was used to etch the specimen. In this method, a thin film of carbon was evaporated onto the surface of the etched specimens. A scalpel was used to cut the carbon film into 3 mm grids which allowed the etchant to penetrate the surface. The matrix below the coating should have been etched away, freeing the coating and any particles present in the matrix. Two solutions were attempted for this stage. Solution 1 and Solution 2, a mixture of 20 ml hydrochloric acid, 5 g CrO<sub>3</sub>, and 80 ml distilled H<sub>2</sub>O, were evaluated for best performance. Samples were transferred to distilled water for flotation of the film and cleaning. A 200 mesh TEM grid was then used to lift the carbon film from the water. Each grid was allowed to dry on filter paper.

In the other method of sample preparation, thin sections were cut from ingot SC-2 using a low speed diamond saw. These sections, approximately 0.025 inches

thick, were thinned further by dry grinding on abrasive SiC wheels. These samples were then cut into 3 mm disks by sniping with a pair of wire cutters. Final thinning was performed by twin-jet electropolishing in a solution of 5 vol. % perchloric acid, 95 vol. % acetic acid at 40 volts and 300 K. Selected TEM specimens were examined at various voltages and modes of operation.

### Differential thermal analysis

Sections of Ingots SC-2 (as-cast), MoC #2 (DS), and MoC #3 (DS) were sent to NLRC for differential thermal analysis (DTA) to determine the melting point of the three compositions. DTA results may also provide information as to the nature of the reactions occurring in each specimen. An empty reference alumina crucible and another alumina crucible containing the sectioned ingot were heated at 10 K/min in a helium atmosphere with a flow rate of 60 cc/min. After the specimen attained a liquid state, the crucibles were then cooled at a rate of 10 K/min under the same conditions. Energies of phase transformation and differences in heat capacity were reflected by a difference in observed temperature in the two crucibles.

### X-ray diffraction

X-ray diffraction was performed on Ingot SC-2 (NiAl-1Mo-1C) and arc-melted Ingots #82 (NiAl-1Mo-1C), #85 (NiAl-1Mo-1C), and #136 (NiAl-0.9Mo-0.9C). Samples of all four ingots were ground into powder prior to testing. In addition, two sections of Ingot SC-2 were etched in two different solutions to remove the NiAl. Sections were placed in either Solution 1 or Solution 2 for several days. The powder residue within each etchant was removed and allowed to dry on filter paper. Powder samples were then sent to NLRC for identification of phases. Powder diffraction tests were performed on an APD1700 or PW3710 automated diffractometer system. Peak

angles were determined using Cu K $\alpha$  radiation. The peak angles were then used to calculate the lattice parameter. From the lattice parameter, the identity of the phases present could be established.

## Results

### Arc-melted ingots

Several types of microconstituents were commonly observed in the arc-melted ingots. Graphite flakes, NiAl dendrites, and "splines" were distinguished as "primary" constituents. The "spline," extremely long and straight, is of particular interest due to the sheath of NiAl surrounding each spline. The NiAl-Mo, two-phase eutectic, recognizable by comparison with melts along the pseudo-binary of the NiAl-Mo system, was also present in some compositions. Two different types of two-phase NiAl-MoC<sub>2</sub> structures were also observed. The first had a "sheet" morphology, while the second appeared to be a "fine" rod-like structure. Several characteristic microstructures are illustrated and labeled in Figures 18-20.

Microconstituents were observed in specific compositional areas as illustrated in Figures 21 and 22. For discussion, the majority of the compositions will be expressed in terms of carbon to molybdenum ratios (C:Mo). Graphite flakes were observed in C:Mo ratios of 0.67 or higher as seen in Figure 21 (a). In addition, NiAl dendrites (without spline) were observed along the pseudobinaries and in the NiAl corner. Splines (with NiAl sheath) were generally observed at C:Mo ratios between 0.25 and 1.5. The two-phase structures were also detected in specific regions: "sheet" from 0.33-1.5, "fine" from 0.2-3, and NiAl-Mo eutectic from 0-0.45.

Scanning electron microscopy revealed the spline to be a broken, lamellar sheet. In fact, some splines exhibited a regular pattern as shown in Figure 23. Although all of the splines did not exhibit this behavior, several observations were made of this

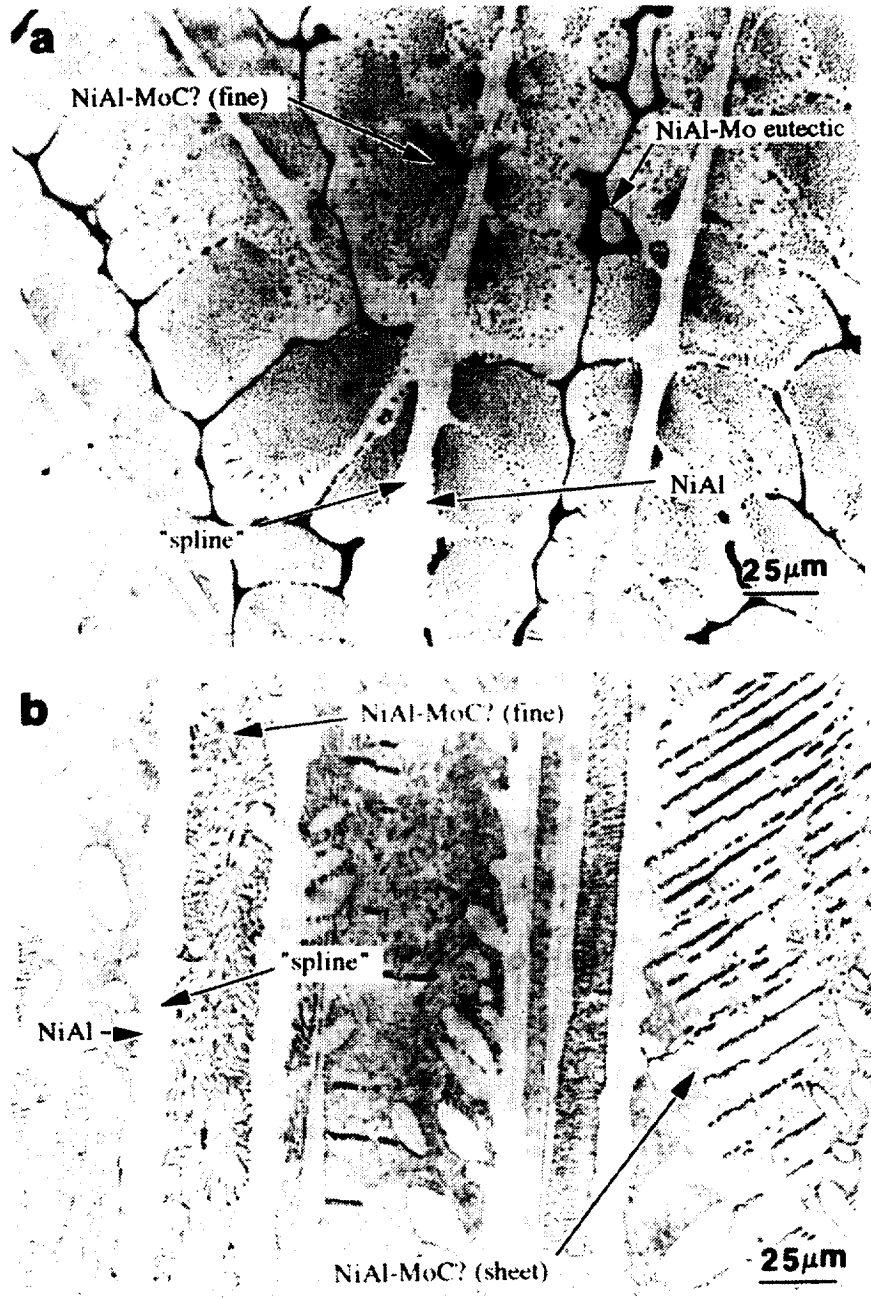


Figure 18: Light optical micrographs of arc-melted ingots with compositions of (a) NiAl-1.58Mo-0.41C and (b) NiAl-1Mo-0.5C.

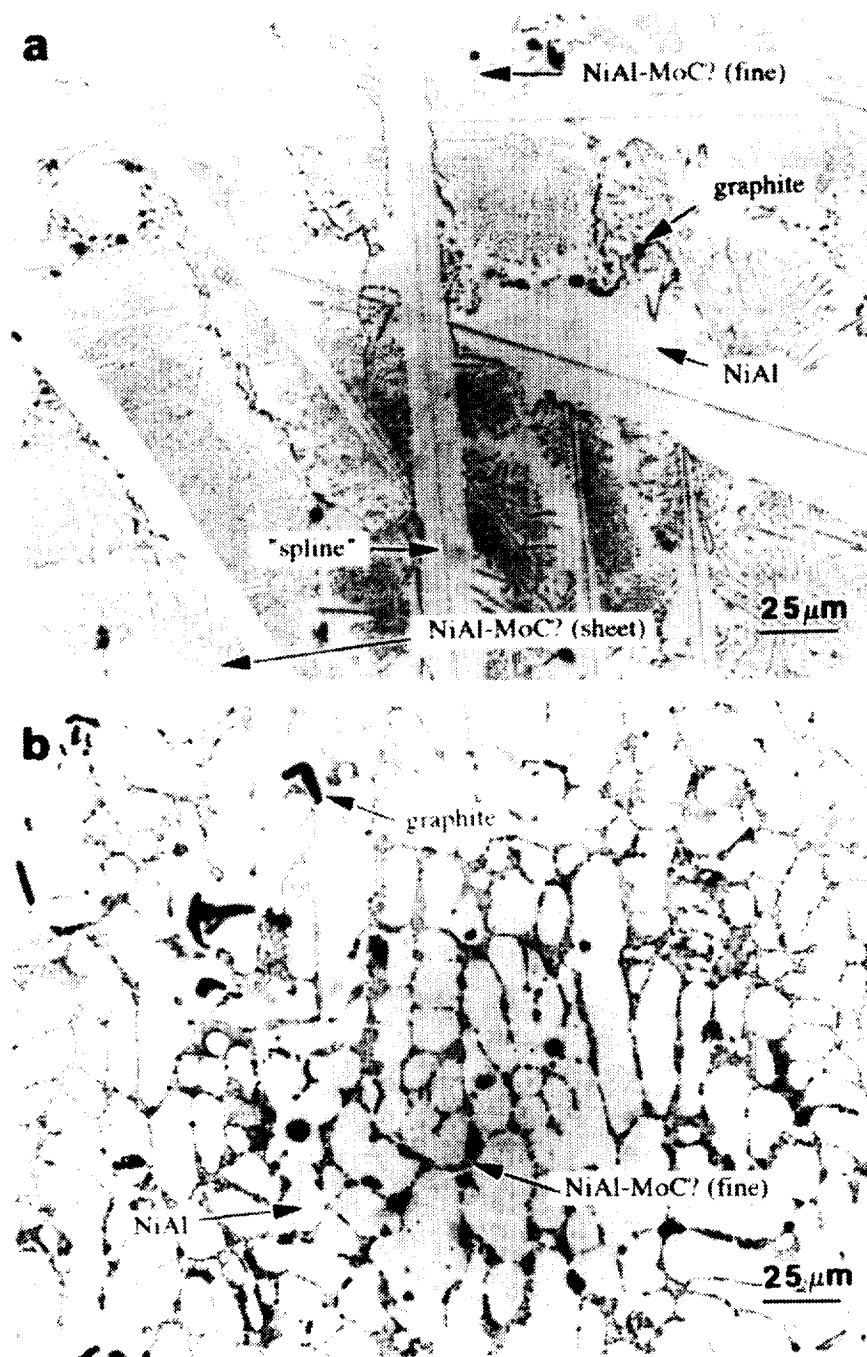


Figure 19: Light optical micrographs of arc-melted ingots with compositions of (a) NiAl-1Mo-1C and (b) NiAl-0.5Mo-1.5C.

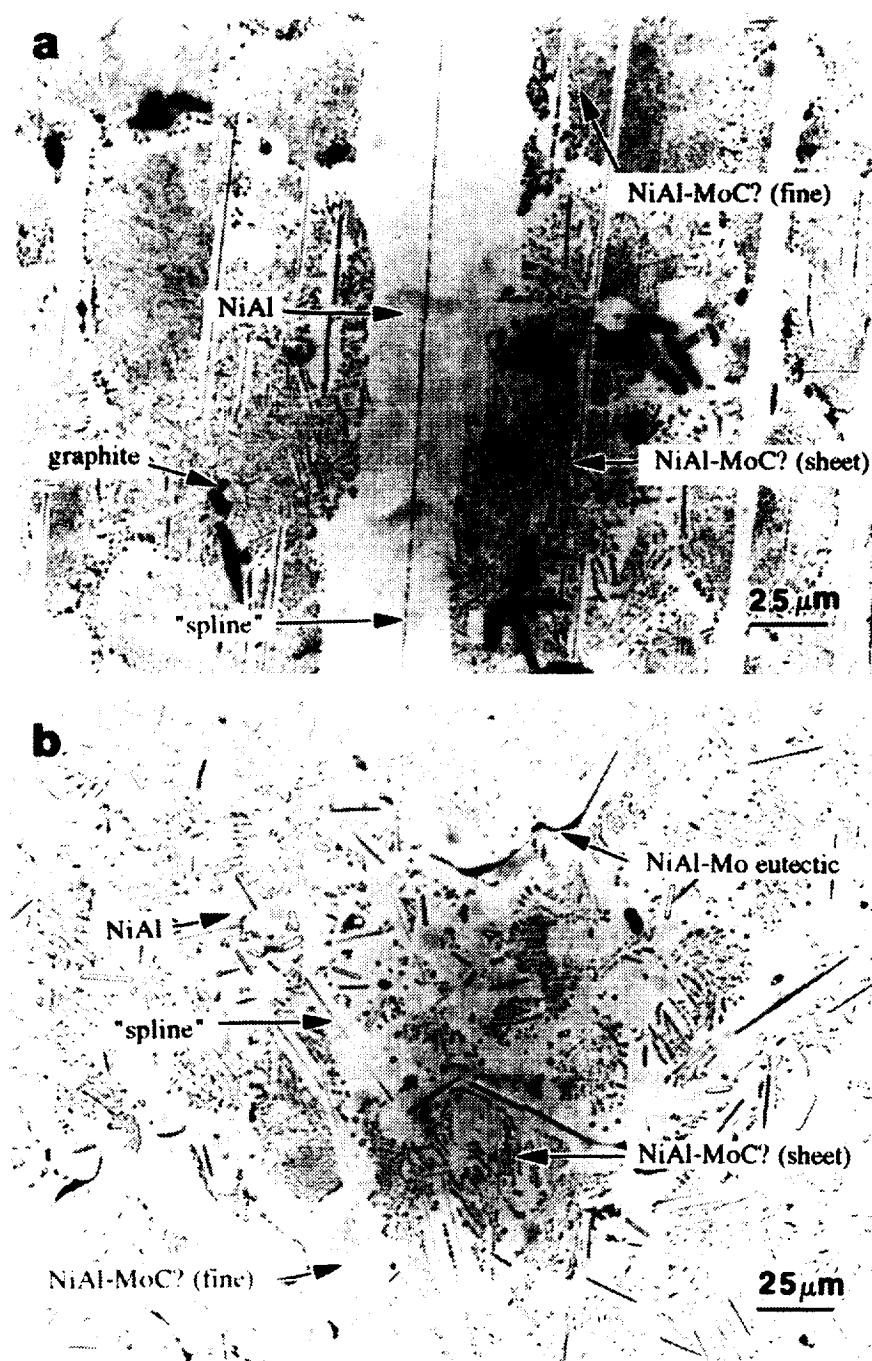


Figure 20: Light optical micrographs of arc-melted ingots with compositions of (a) NiAl-1Mo-1.5C and (b) NiAl-2.75Mo-1.24C.

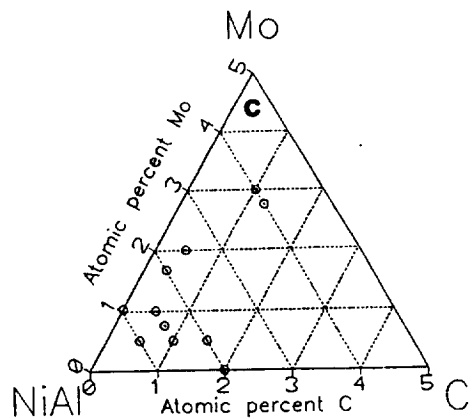
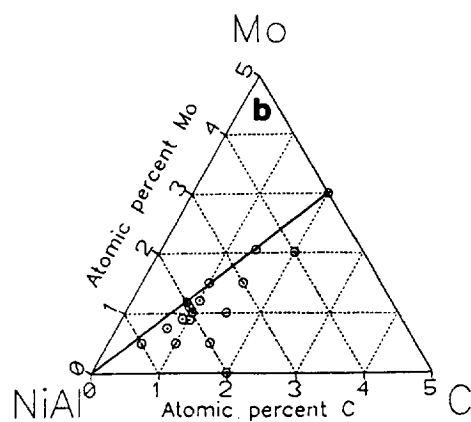
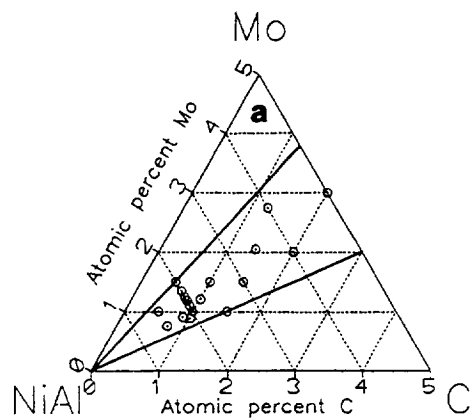


Figure 21: Arc-melted ingot compositions containing (a) "splines" with NiAl sheath, (b) graphite flakes, and (c) NiAl dendrites (no spline).

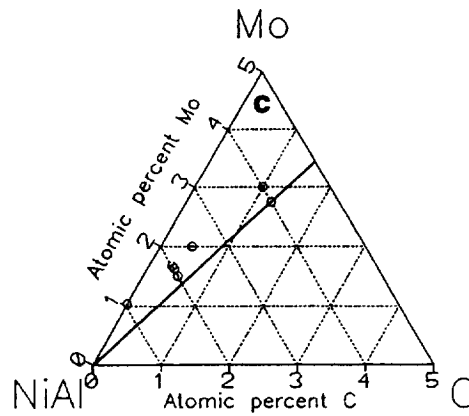
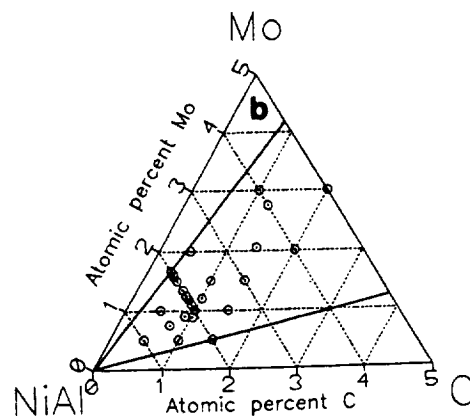
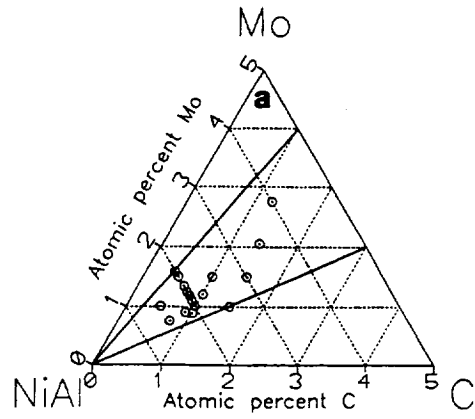


Figure 22: Arc-melted ingot compositions containing (a) NiAl-MoC? (sheet) two-phase structure, (b) NiAl-MoC? (fine) two-phase structure, and (c) NiAl-Mo two-phase eutectic.

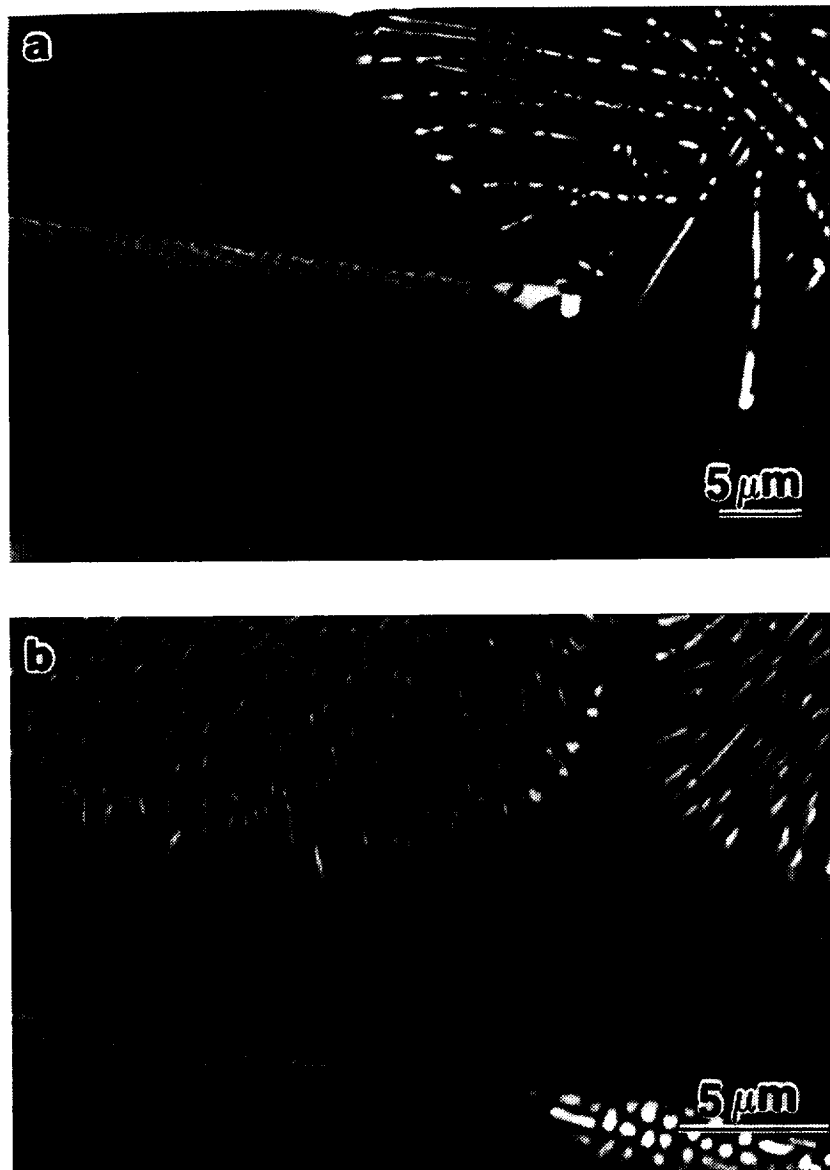


Figure 23: SEM backscattered electron micrograph of an arc-melted NiAl-1Mo-1C ingot showing splines with lattice-type structures.

regular "lattice-work" structure. In addition, the "fine" two-phase structure was verified to be rod-like as also seen by the micrographs in Figure 24. The NiAl-Mo interdendritic structure is also observable.

Extraction of the carbides from the NiAl was to some extent successful. In the first few specimens, Solution 1 showed no observable effect upon the surface, even after 1 hour of etching. Solution 2 was also tested on several specimens, but reacted so violently that bubbles formed beneath the carbon film and disintegrated it. Solution 1 was again tested with more uniform scratches upon the carbon film. Although the reaction took between 20 and 30 minutes, it was partially successful. None of the collected specimens were full 3 mm grids. All broke away into smaller pieces before lifting from the surface.

The first composition examined by transmission electron microscopy was NiAl-1.58Mo-0.41C. Although some concern had been made about the extraction method, it appeared to be successful. Figure 25 is a bright field micrograph of a large number of particles imbedded in the carbon film. At higher magnification, it is clear that they are short aspect rods approximately 1  $\mu\text{m}$  in length. The approximate diameter of the rods was shown to be about 0.1  $\mu\text{m}$  in Figure 26. A dendritic particle was also observed in these specimens (Figure 27). Larger bundles of fibers, likely bundles of molybdenum fibers from the NiAl-Mo eutectic, were also observed imbedded in the film (Figure 28). The other compositions produced particles of similar and dissimilar shapes. From NiAl-2.75Mo-1.24C, Figure 29 is a bright field image of a large dendritic particle exhibiting uniform branching. Additionally, Figure 30 is a TEM micrograph of a slightly faceted particle from an NiAl-0.5Mo-1.5C ingot. Diffraction patterns were attempted in several different situations, but limited size of the particles prevented good results.

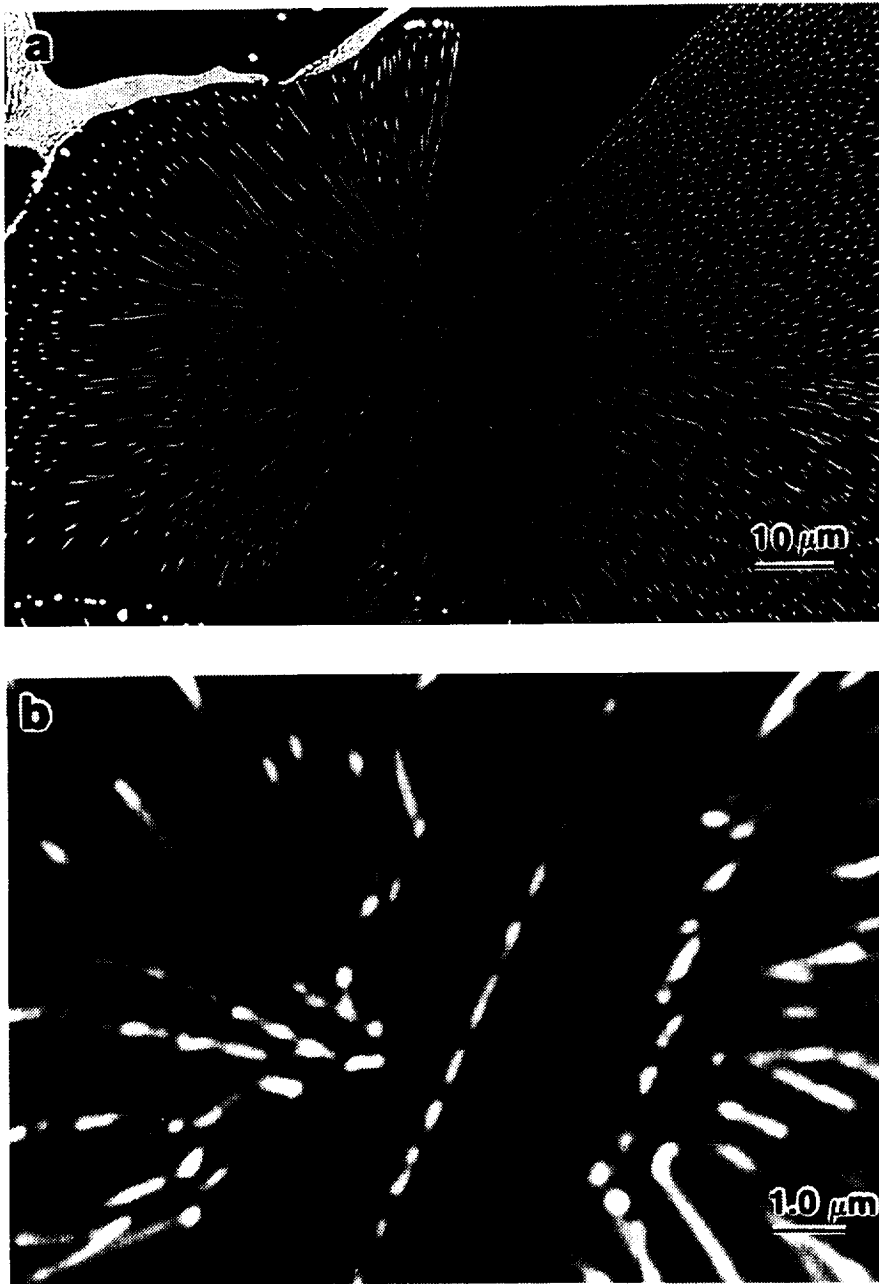


Figure 24: SEM backscattered electron micrograph of an arc-melted NiAl-1.58Mo-0.41C ingot showing a "spline" with sheath and the NiAl-MoC? (fine) constituent.

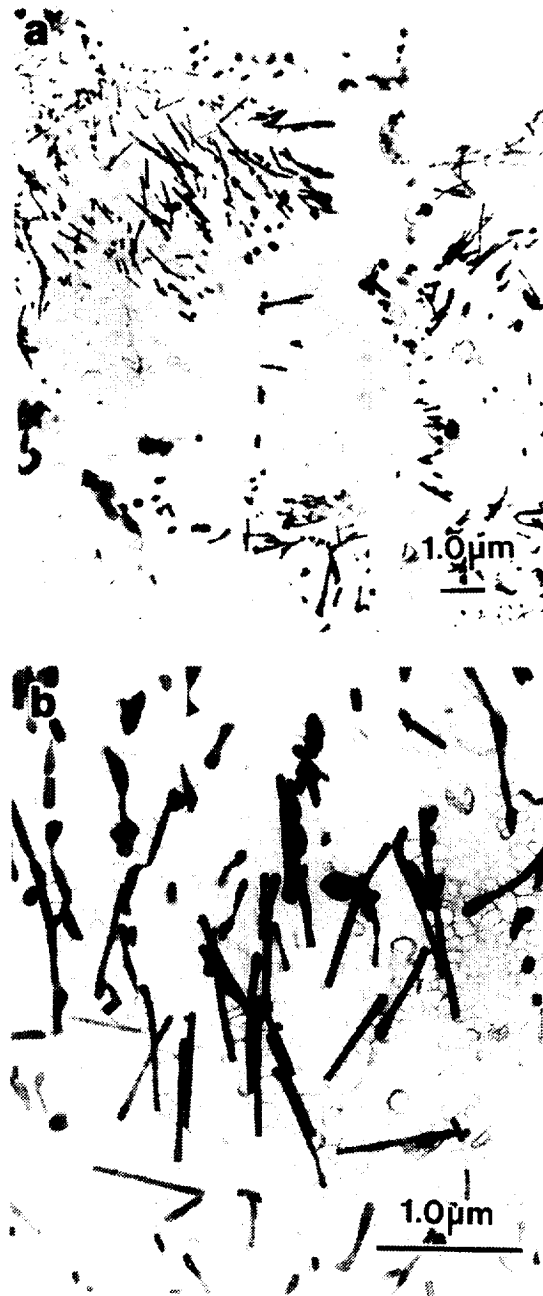


Figure 25: Brightfield TEM photomicrograph of extracted particles from an arc-melted NiAl-1.58Mo-0.41C ingot.

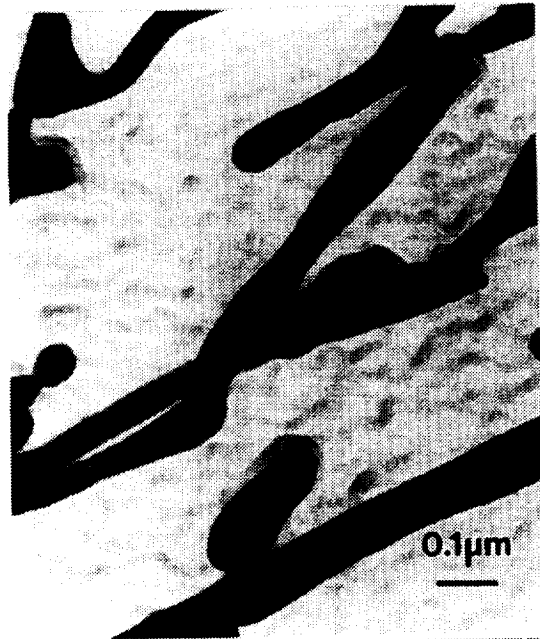


Figure 26: Brightfield TEM photomicrograph of extracted particles from an arc-melted NiAl- 1.58Mo-0.41C ingot.

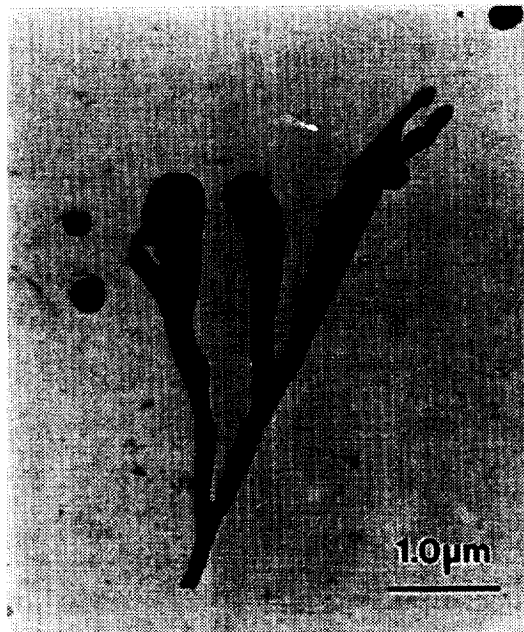


Figure 27: Brightfield TEM photomicrograph of extracted particles from an arc-melted NiAl-1.58Mo-0.41C ingot.



Figure 28: Brightfield TEM photomicrograph of extracted particles from an arc-melted NiAl-1.58Mo-0.41C ingot.

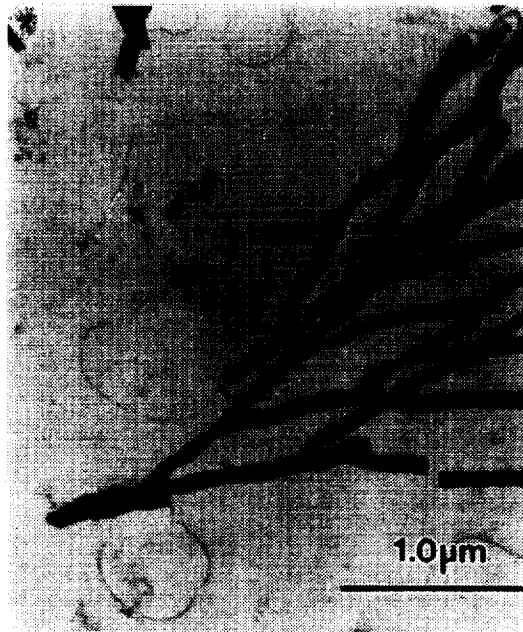


Figure 29: Brightfield TEM photomicrograph of extracted particles from an arc-melted NiAl-2.75Mo-1.24C ingot.

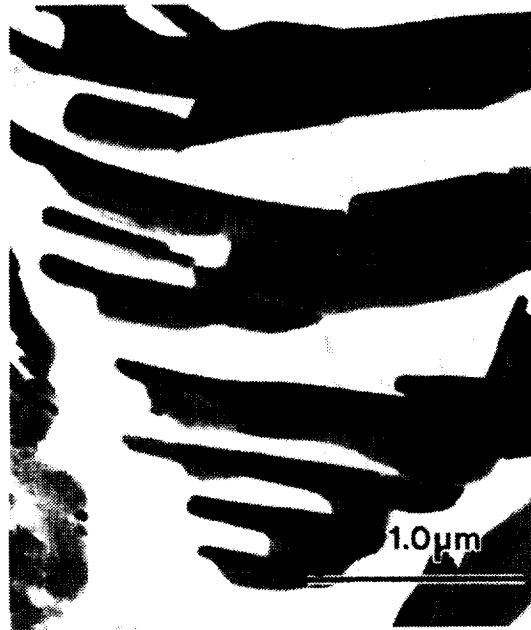


Figure 30: Brightfield TEM photomicrograph of extracted particles from an arc-melted NiAl-0.5Mo-1.5C ingot.

Powder x-ray diffraction of several arc-melted specimens identified NiAl and MoC (50 at. % C, hexagonal). The x-ray results are provided in Appendix A. With the larger volume fraction of NiAl relative to the carbide, the relative intensity of the carbide peaks was much lower than that of NiAl.

### Slow cooled ingots

All of the microconstituents observed in the arc-melted ingots were also present within the slow cooled ingots. One exception is the regular lattice-work structure of the splines. Observations were made of splines with holes (Figure 31), but none with the regular lattice-work structure seen within some of the arc-melts. Ingots SC-2 (NiAl-1Mo-1C), SC-6 (NiAl-1Mo-3C), and SC-7 (NiAl-1Mo-1C) contained large regions of aligned carbides and graphite flakes in an NiAl matrix as seen in Figures 32 and 33. The aligned carbides are large broken lamellar sheets very similar in appearance to the splines (Figure 34). Heavy etching revealed large, branched carbides similar to those observed in the arc-melted specimens (Figure 35). In addition, limited metallography of Ingot SC-7 (NiAl-1Mo-1C) revealed splines surrounded by aligned carbides (Figure 36).

Transmission electron microscopy of Ingot SC-2 was not very successful. Although the thinning process produced a hole in each sample, only small areas were thin enough to allow electron transmission. Figure 37 is a brightfield image of particles protruding from the matrix across a hole. Diffraction patterns were performed on areas permitting transmission.

Differential thermal analysis (DTA) performed on a section of Ingot SC-2 (NiAl-1Mo-1C) is provided in Appendix B. The melting point of this composition was shown to be 1889 K. Two peaks occur at high temperatures. This is not characteristic of true eutectic reaction which would provide only a single peak for the eutectic

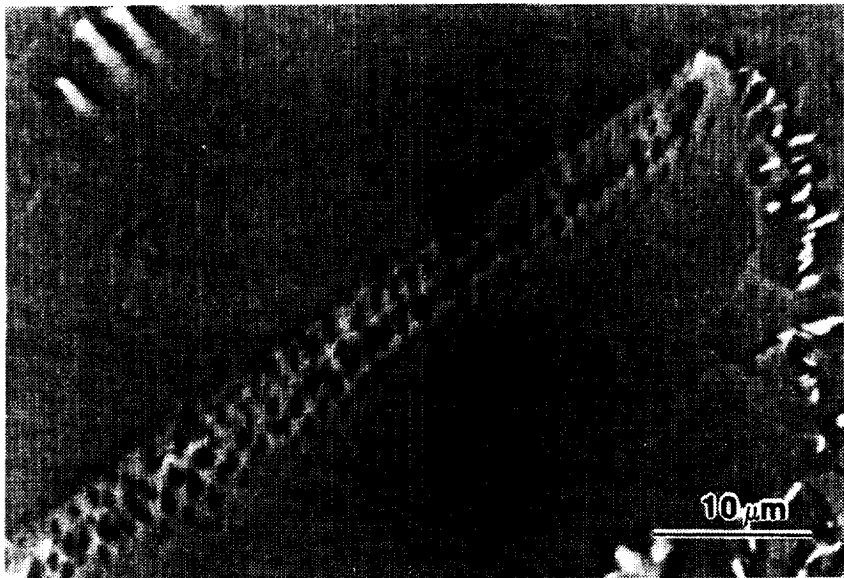


Figure 31: Backscattered SEM micrograph of a heavily etched slow cooled NiAl-1Mo-3C ingot showing spline with holes.

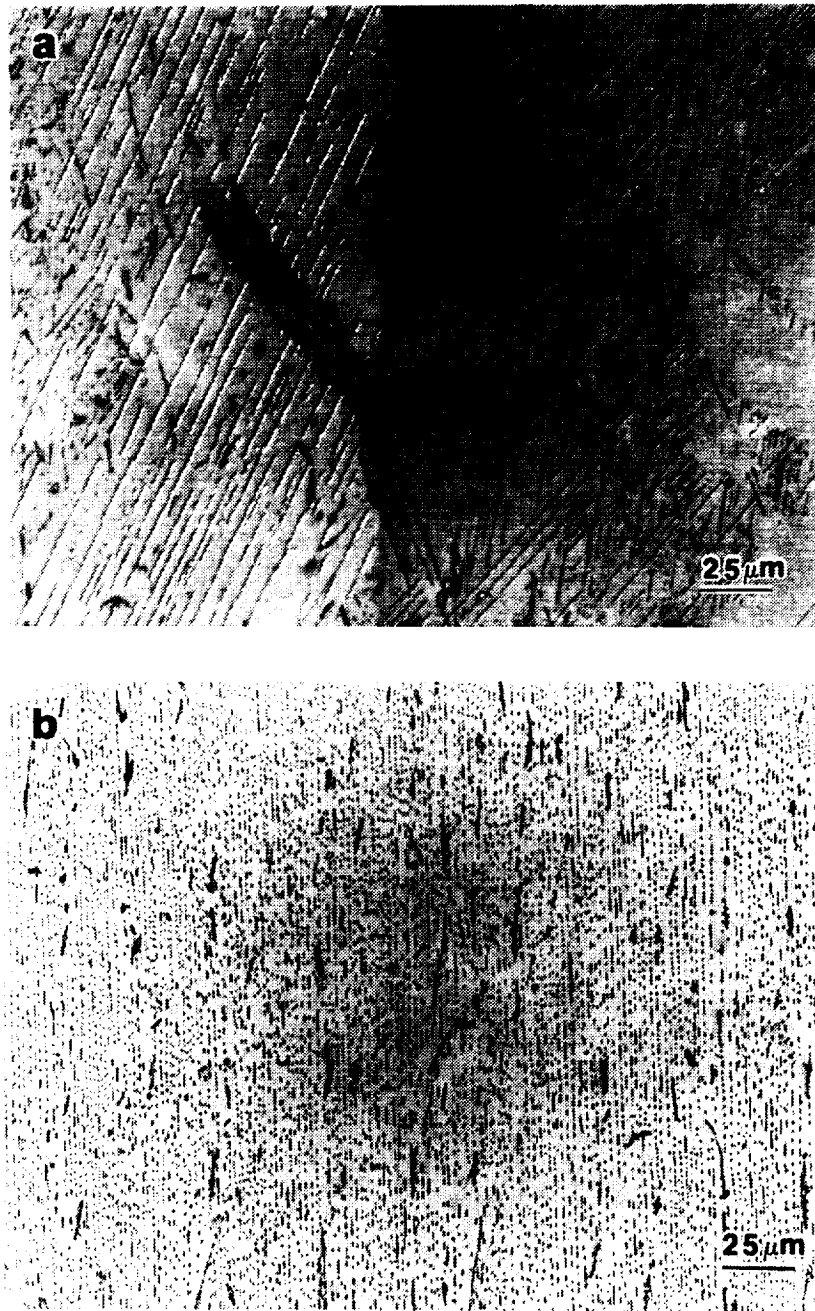


Figure 32: Light optical micrographs showing aligned carbides in slow cooled ingots (a) NiAl-1Mo-1C and (b) NiAl-1Mo-3C.

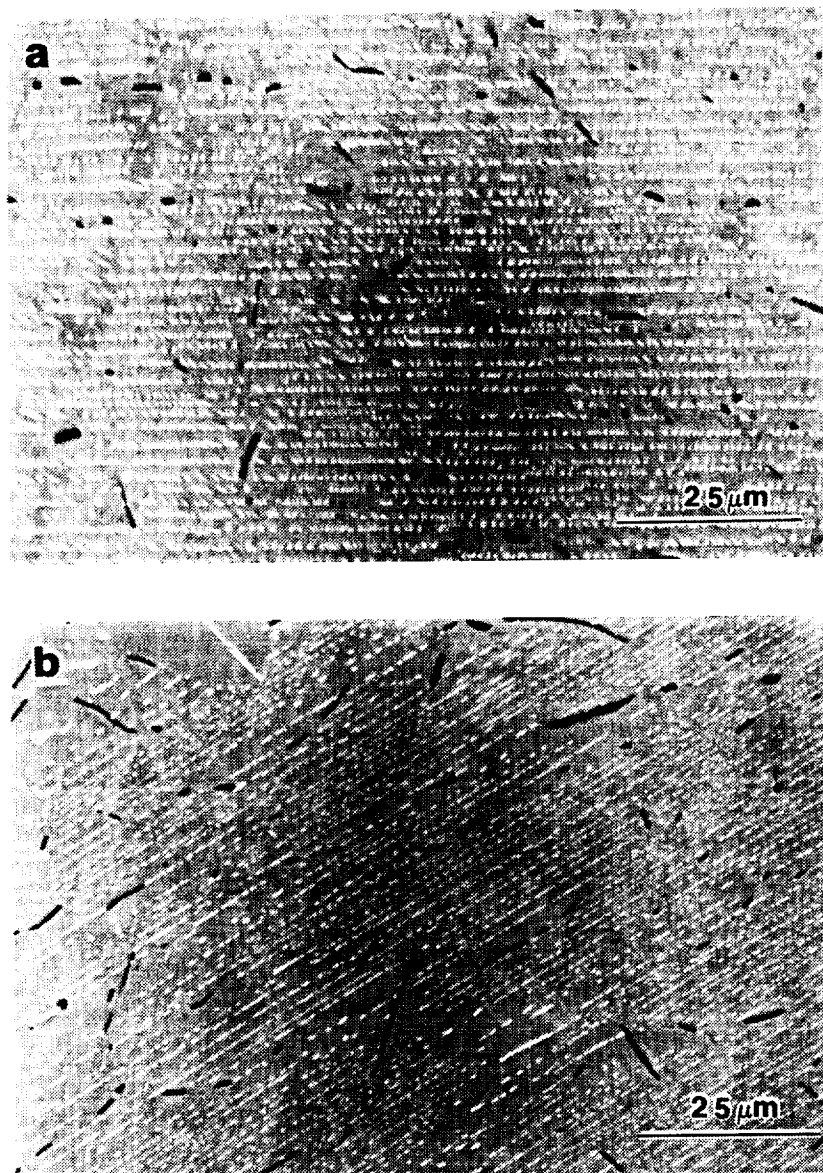


Figure 33: Backscattered SEM micrographs showing aligned carbides in slow cooled ingot SC-2 (NiAl-1Mo-1C).

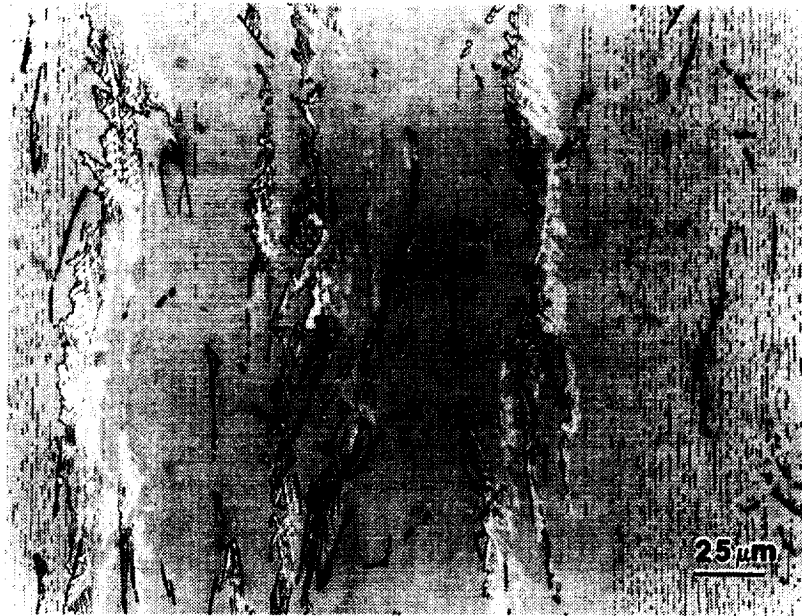


Figure 34: Light optical micrograph showing broken lamellar sheets of carbides in a slow cooled NiAl-1Mo-3C ingot.

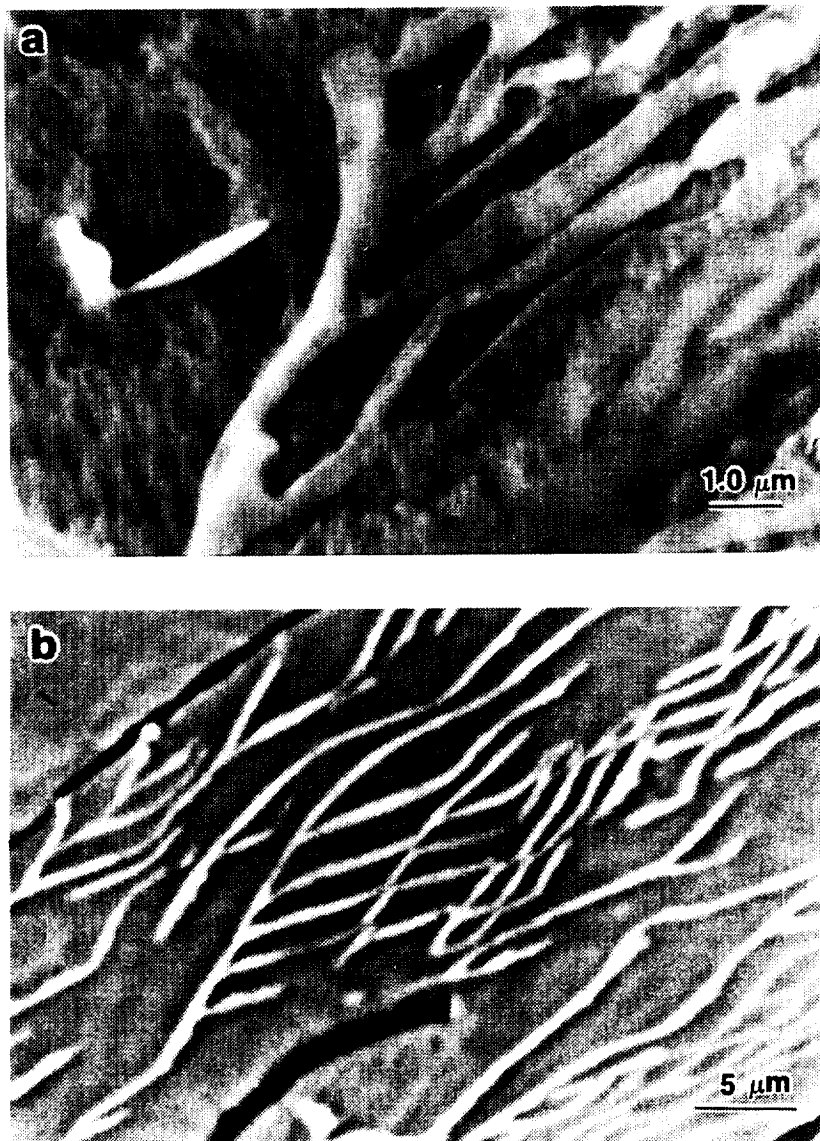


Figure 35: Backscattered SEM micrograph showing branched carbides in slow cooled ingots (a) SC-2 (NiAl-1Mo-1C) and (b) SC-6 (NiAl-1Mo-3C).



Figure 36: Backscattered SEM micrograph for slowed cooled ingot SC-7 (NiAl-1Mo-1C) showing spline with NiAl sheath surrounded by aligned carbides.



Figure 37: Brightfield TEM photomicrograph of particles protruding from the matrix of Ingot SC-2 (NiAl-1Mo-1C).

composition. In addition, a shoulder existed at approximately 1300°C.

Microstructural characterization revealed that the structure was completely unlike that observed prior to testing (Figure 38).

Powder x-ray diffraction again revealed the presence of NiAl and MoC (hexagonal, 50 at. % C) but also possibly a small amount of  $\alpha\text{Mo}_2\text{C}$  (hexagonal). Powder diffraction upon the residue from etching in Solution 1 was not successful. It was felt that the powder residue was of an organic nature. Powder diffraction on the residue from Solution 2 was identified as MoC. X-ray diffraction results are presented in Appendix A.

#### Heat treated ingots

Heat treatments on arc-melted specimens at 1473 K for 24 hours produced no observable changes in the microstructures. Sections of Ingot SC-2 (NiAl-1Mo-1C) annealed at higher temperatures did show variations in the microstructures after the treatments. Characteristic microstructures prior to treatment are presented in Figure 39. Figures 40, 41, and 42 are optical micrographs of heat treated sections of Ingot SC-2 for annealing conditions of 1603 K for 3 hours, 1623 K for 6 hours, and 1723 K for 3 hours, respectively. All three conditions produced Widmanstätten-type precipitation and finer, oriented carbides. However, even after annealing at 1623 K for 6 hours, the sheath of NiAl surrounding the carbide spline remained (Figure 43).

#### Directionally solidified ingots

Although only two ingots, MoC #2 (NiAl-1Mo-0.61C) and MoC #3 (NiAl-1Mo-0.73C), were directionally solidified successfully, the small processed regions from Ingot MoC #4 (NiAl-1Mo-1C) and spills from additional ingots provided information for the microstructural characterization of this system. Figure 44

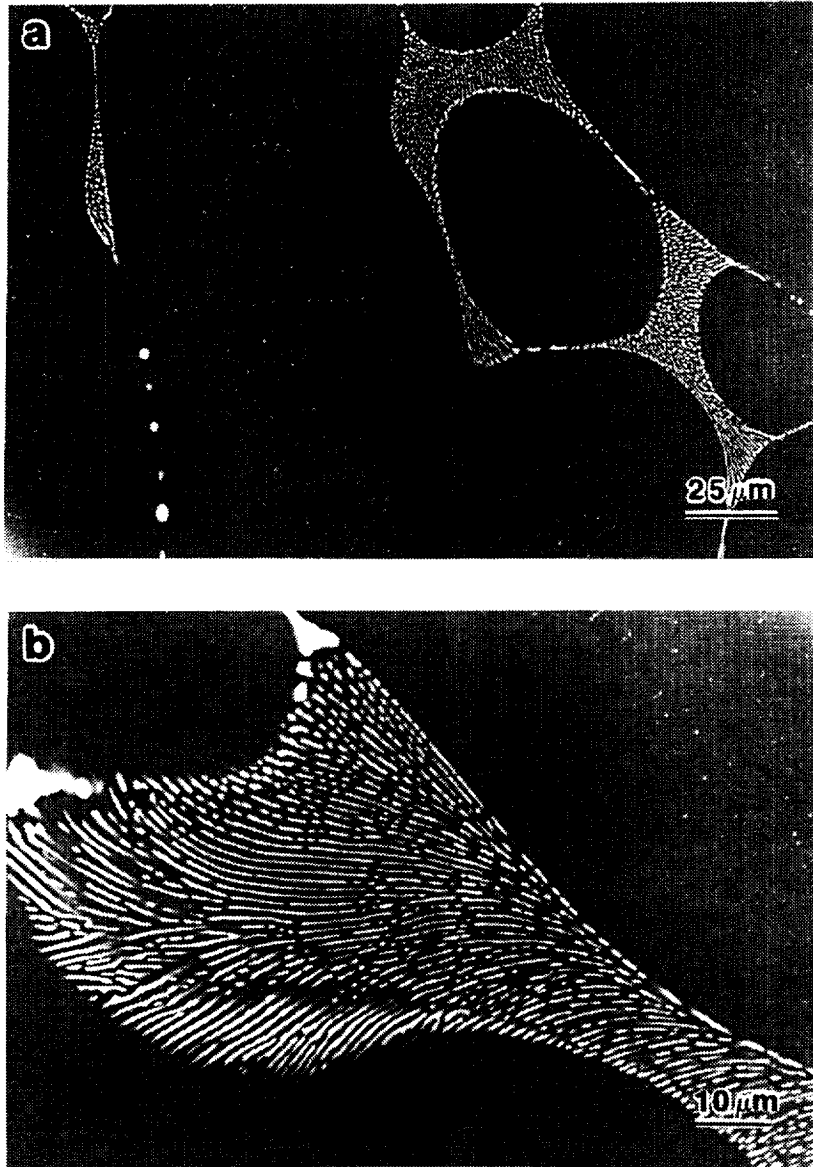


Figure 38: Backscattered SEM micrograph of a slow cooled NiAl-1Mo-1C ingot after differential thermal analysis.

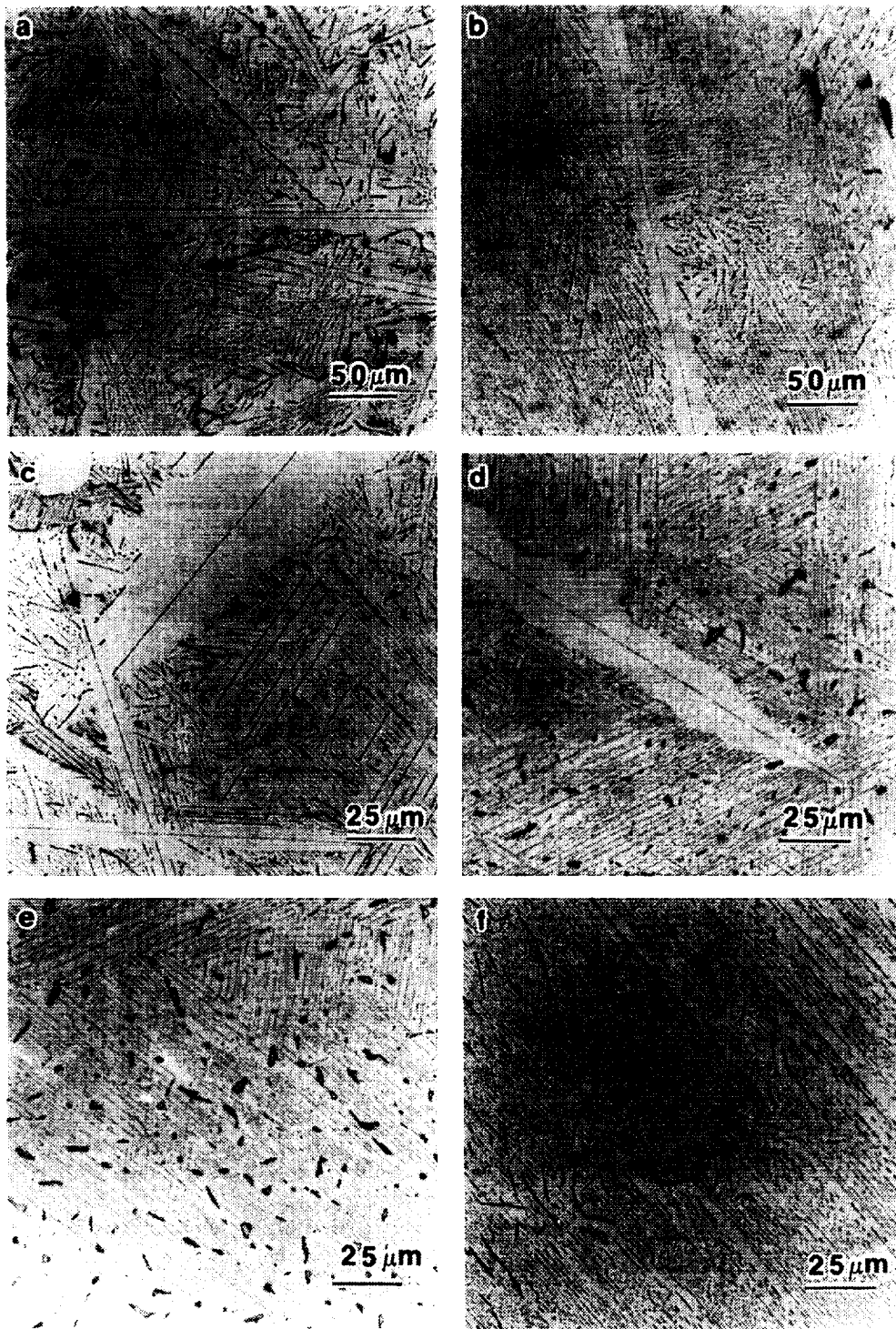


Figure 39: Light optical photomicrographs of characteristic microstructures for a slow cooled NiAl-1Mo-1C ingot prior to heat treatments.

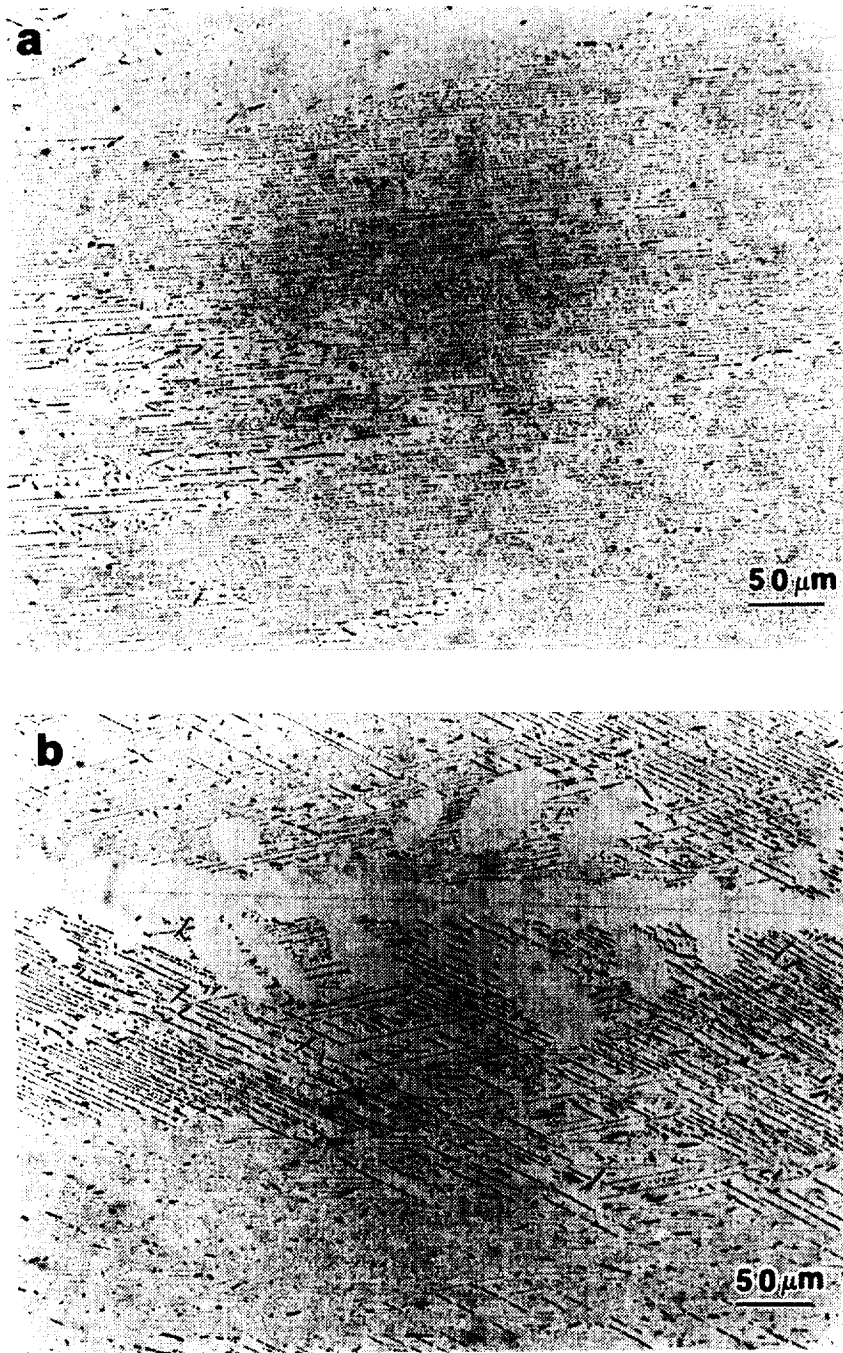


Figure 40: Light optical micrographs for a slow cooled NiAl-1Mo-1C ingot annealed at 1603 K for 3 hours and furnace cooled.

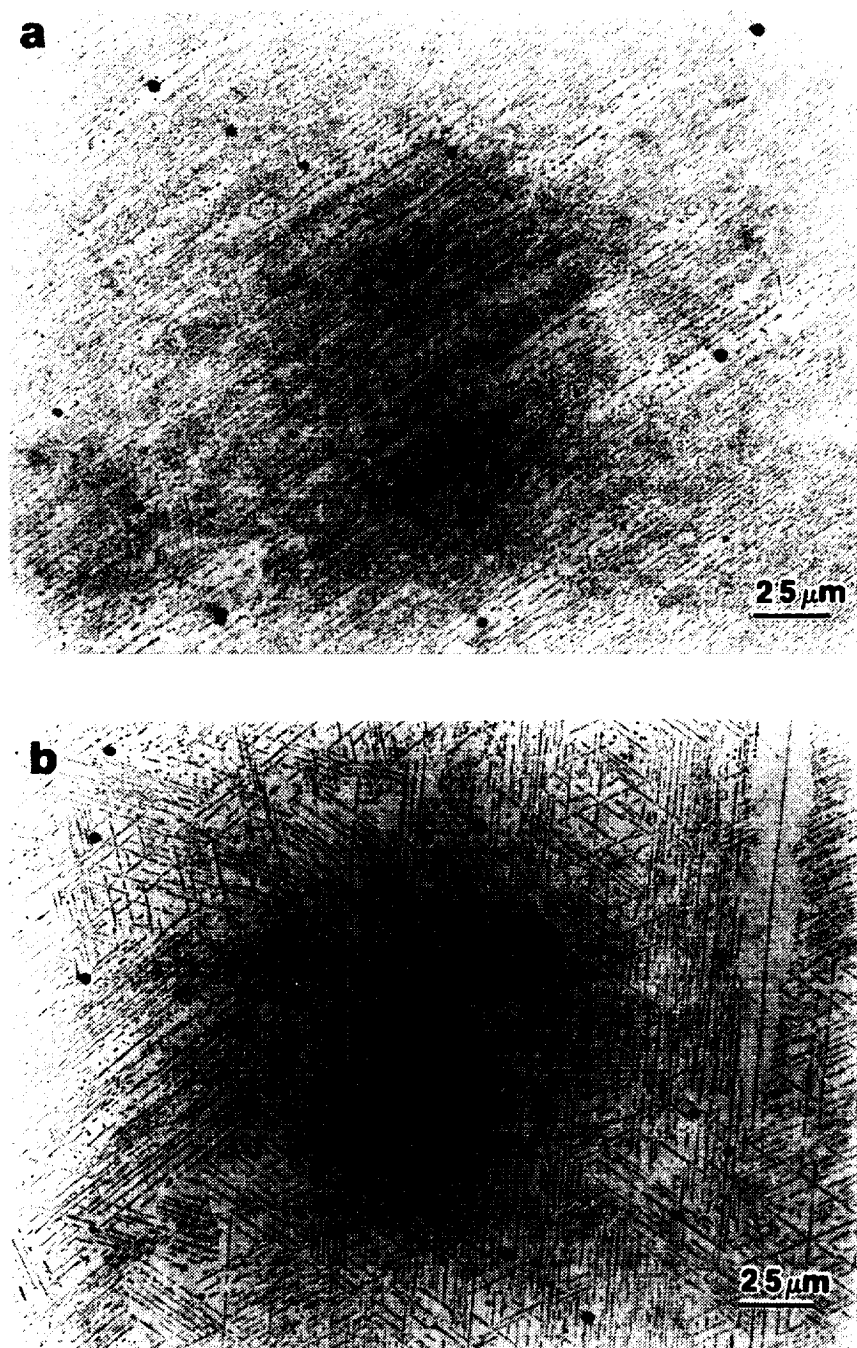


Figure 41: Light optical micrographs for a slow cooled NiAl-1Mo-1C ingot annealed at 1623 K for 6 hours and furnace cooled.

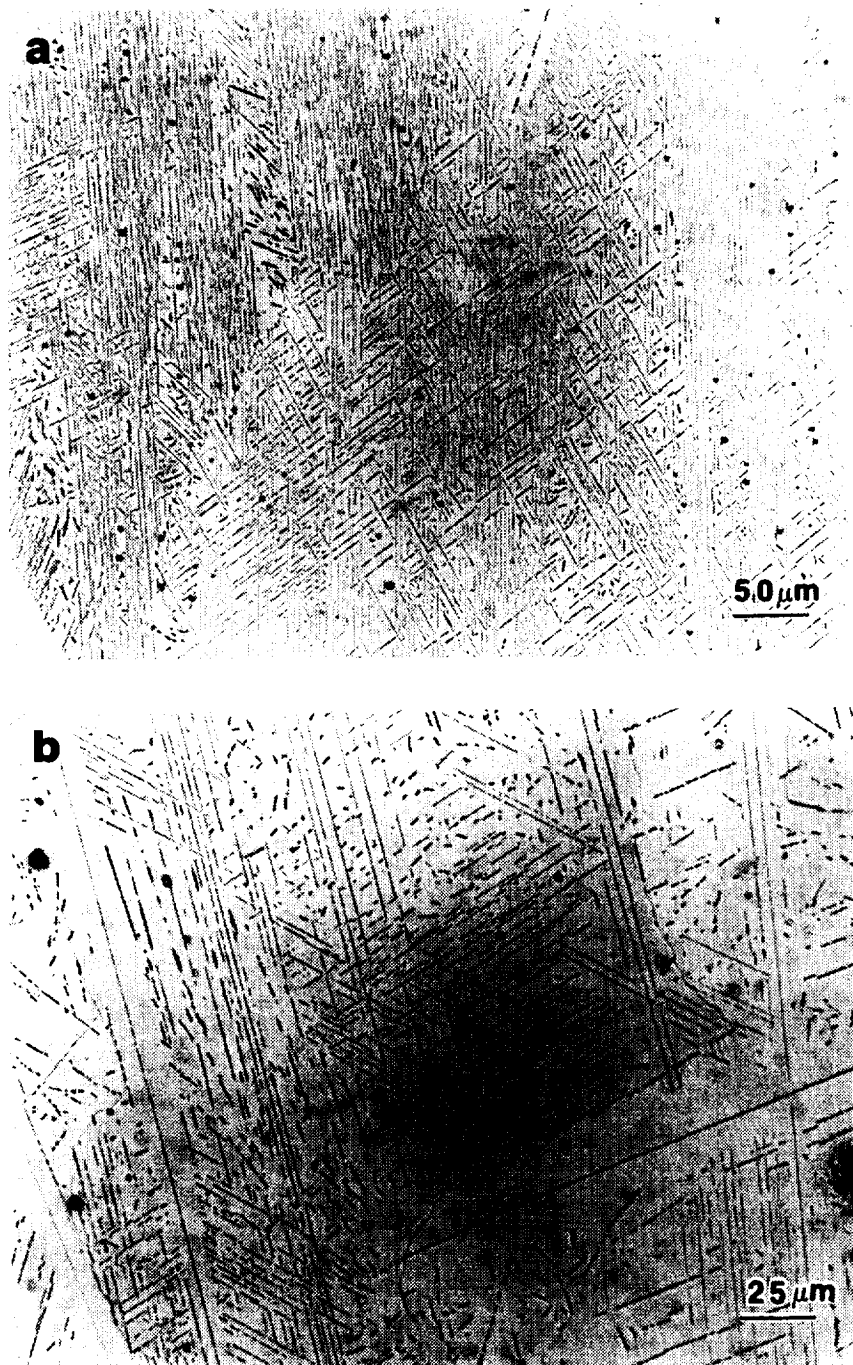


Figure 42: Light optical micrographs for a slow cooled NiAl-1Mo-1C ingot annealed at 1723 K for 3 hours and furnace cooled.

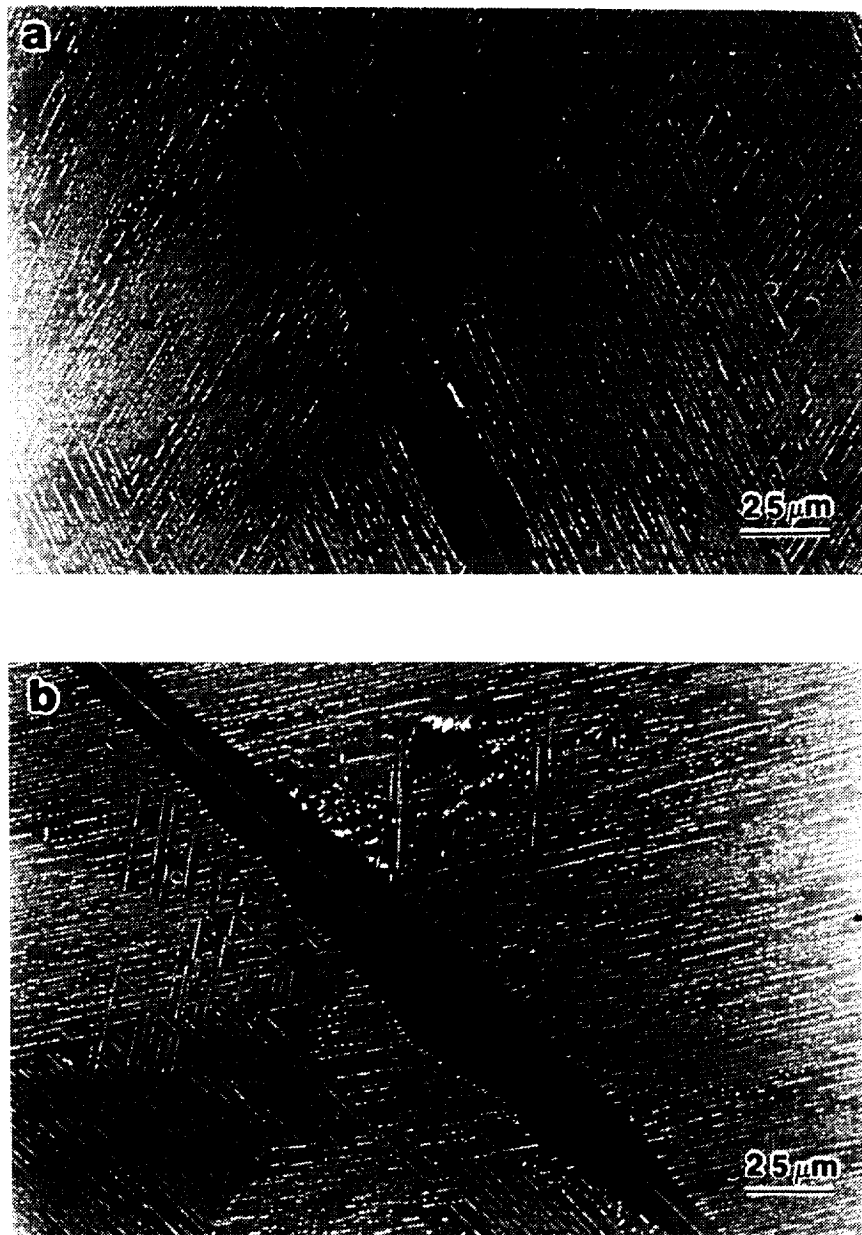


Figure 43: Backscattered SEM micrograph for a slow cooled NiAl-1Mo-1C ingot annealed at 1623 K for 6 hours and furnace cooled.

illustrates typical microstructures of the cast precursor ingots. These structures have the same characteristic structures as those observed in the arc-melted and slow cooled ingots.

Metallography on directionally solidified ingots MoC #2 and MoC #3 revealed a transition from a random dispersion of particles in an NiAl matrix near the first zone to oriented particles observed near the last zone (Figure 45). Ingot MoC #4, which froze due to a spill and coating on the interface, showed structures similar to those observed near end of processing for Ingots #2 and #3 (Figure 46). One exception is the presence of large graphite flakes in Figure 46 (a). While splines were not observed in the directionally solidified materials, they were present in the last zone and in spills from the liquid zone which occurred during processing. Optical micrographs from a spill during processing of Ingot MoC #4 are shown in Figure 47. The structure in Figure 47 (b) appears to be similar to the Widmanstätten-type precipitation observed during heat treating of the slow cooled ingots. In addition, microstructures from a spill during processing of Ingot MoC #2 are presented in Figure 48. The splines appear to nucleate from a single location and at angles of about  $60^\circ$ . Additional metallography on material from the failed directional solidification of Ingots MoC #5 and #6 revealed structures very similar to those shown in Figures 46 and 47.

Differential thermal analysis results for material taken from directionally solidified Ingots MoC #2 and MoC #3 are provided in Appendix B. The melting points are 1874 and 1870 K, respectively. As with the slow cooled ingot, two separate peaks are differentiated upon cooling. A shoulder is also apparent for each composition, but at different temperatures. Microstructural observations of the post-DTA samples revealed microstructures nearly identical to those of Figure 38.

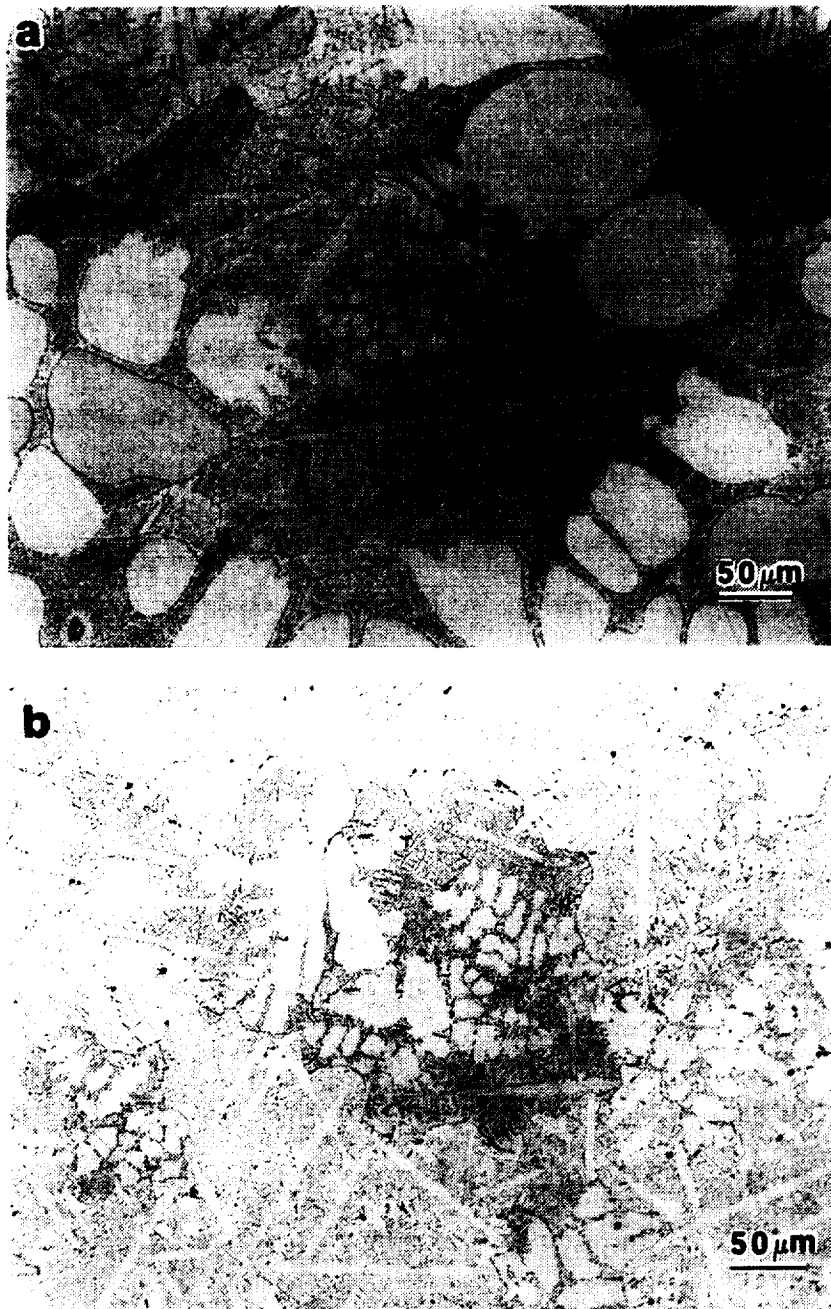


Figure 44: Light optical micrographs of cast precursor ingots (a) MoC #1 (NiAl-1Mo-0.59C) and (b) MoC #3 (NiAl-1Mo-0.73C).

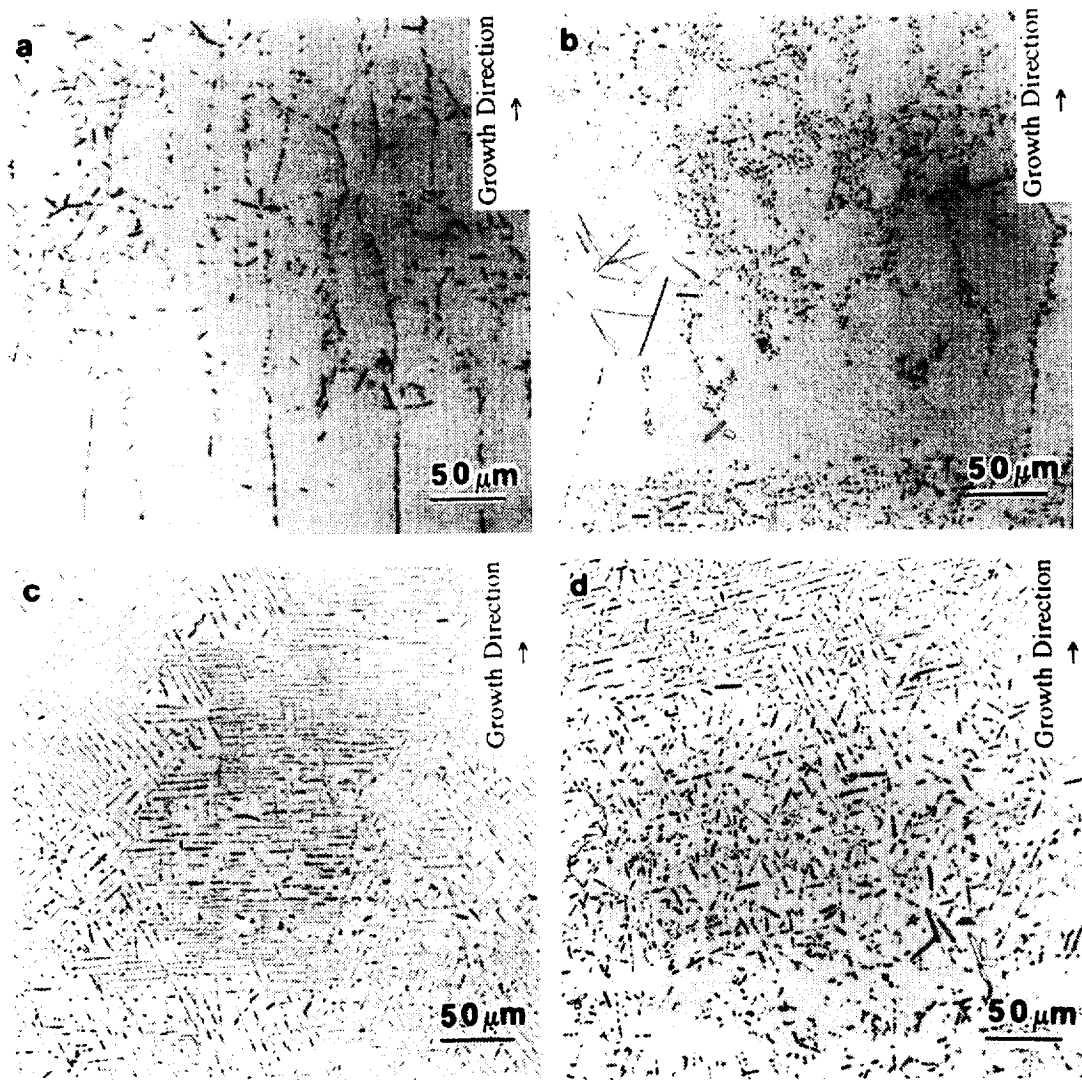


Figure 45: Light optical micrographs for directionally solidified Ingot MoC #3 (NiAl-1Mo-0.73C) showing transition from (a) near first zone to (d) just before last zone.

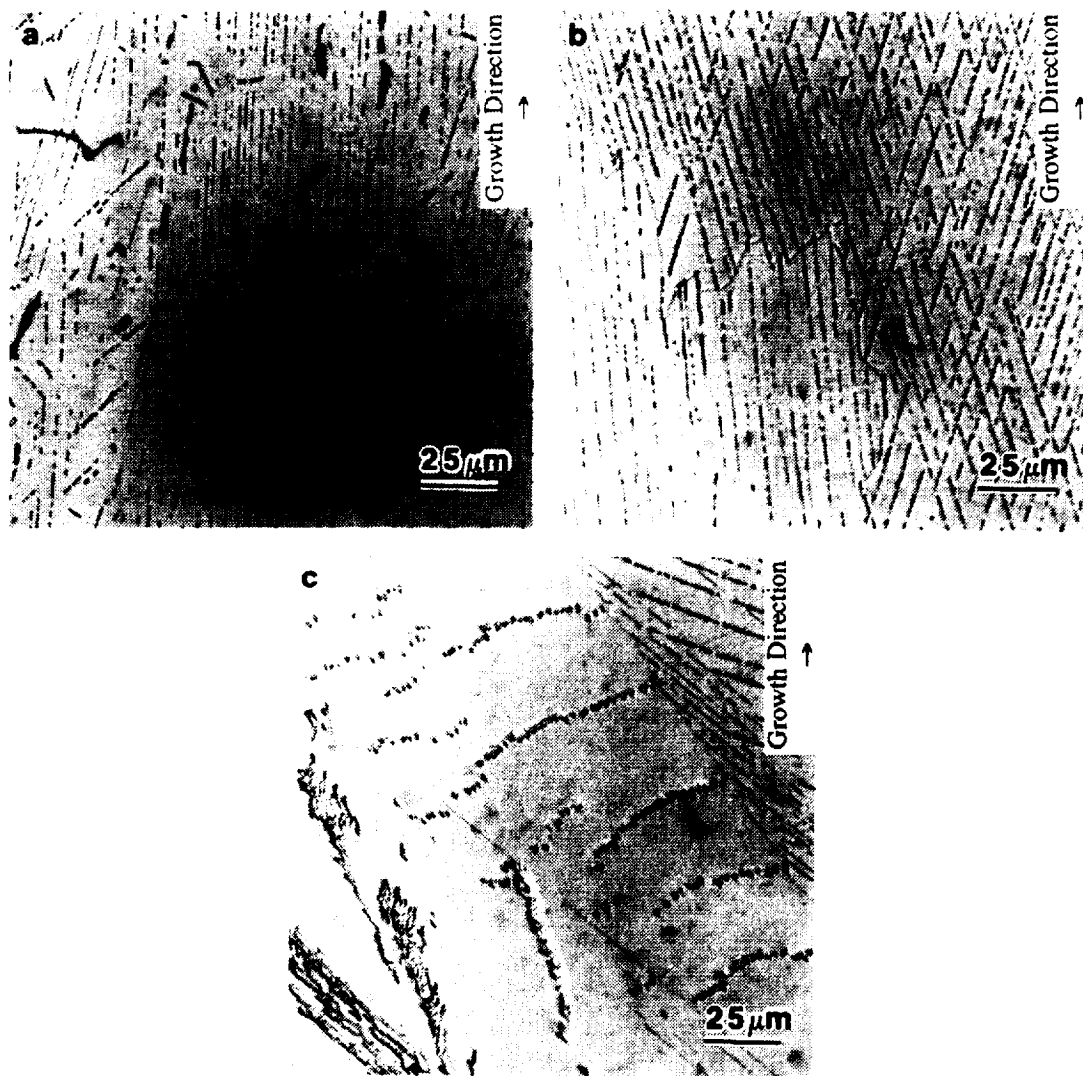


Figure 46: Light optical micrographs for directionally solidified ingot MoC #4 (NiAl-1Mo-1C).

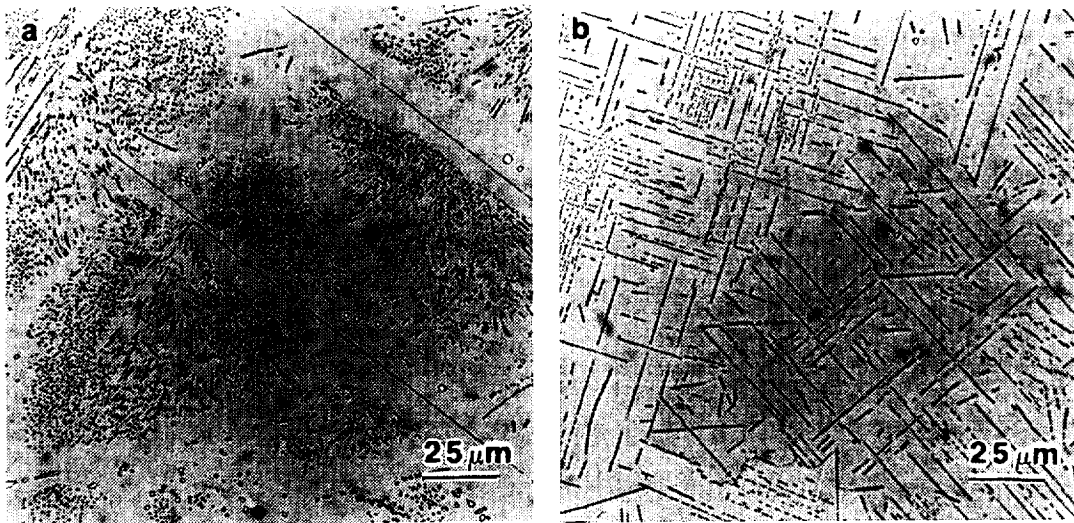


Figure 47: Light optical micrographs for a spill which occurred during containerless directional solidification of Ingot MoC #4 showing (a) splines and (b) Widmanstätten-type structure.

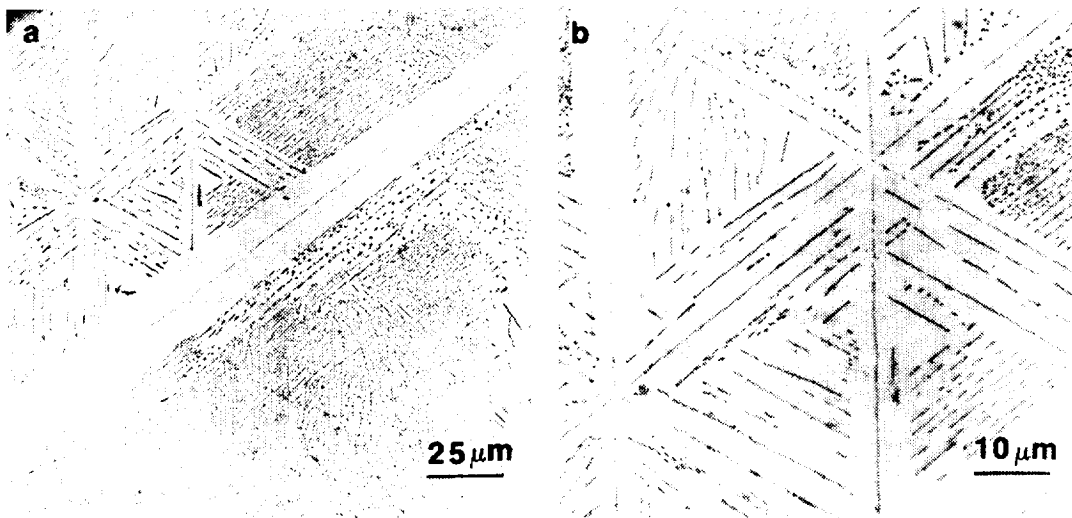


Figure 48: Light optical micrographs for a spill which occurred during containerless directional solidification of Ingot MoC #2 showing splines with a sheath of NiAl surrounding each.

## Discussion

Uncertainties abound regarding the NiAl-Mo-C microstructures. Several theories have been proposed regarding the formation of the splines surrounded by a sheath of NiAl. The carbides solidify first from the liquid with the NiAl nucleating on the surface. Since the splines have not been observed in directionally solidified material, it is felt that they are the result of large undercoolings present during freezing of the arc-melted or slow cooled ingots. The splines were also observed in the last zone to freeze or in spills from the liquid zone during processing (Figure 47). X-ray diffraction has identified the presence of MoC and possibly  $\alpha\text{Mo}_2\text{C}$  in the system. Both have complex crystal structures (hexagonal). Sundquist and Mondolfo have shown that metals or compounds with complex structures may often act as nucleating agents for materials with simple, open crystal structures [71].

Additionally, it has been proposed that the carbide may be a faceted phase. Whereas non-faceted phases have low undercoolings and typically isotropic growth, faceted phases are often associated with large undercoolings and anisotropic growth [72]. The aligned carbides observed in the slow cooled ingots in Figures 32-34 are very similar in appearance to the broken lamellar eutectic structures observed in numerous other systems [73, 74]. The broken lamellar eutectic structure consists of 'broken' plates in a regular array. This type of eutectic occurs in faceted/non-faceted systems containing < 10% volume of the faceting phase [74]. From microstructural observations, the NiAl-Mo-C system contains this type of eutectic reaction.

Although the carbides have been tentatively identified as MoC, it is possible that they are  $\text{Mo}_2\text{C}$ . Identification of the carbides by TEM diffraction patterns was difficult due to the similarity of the atom locations in the basal plane (0001). Simulated TEM diffraction patterns for these two carbides are nearly identical for the (0001) zone axis (Figure 49) [75]. Weaver has identified coarse precipitates in directionally solidified

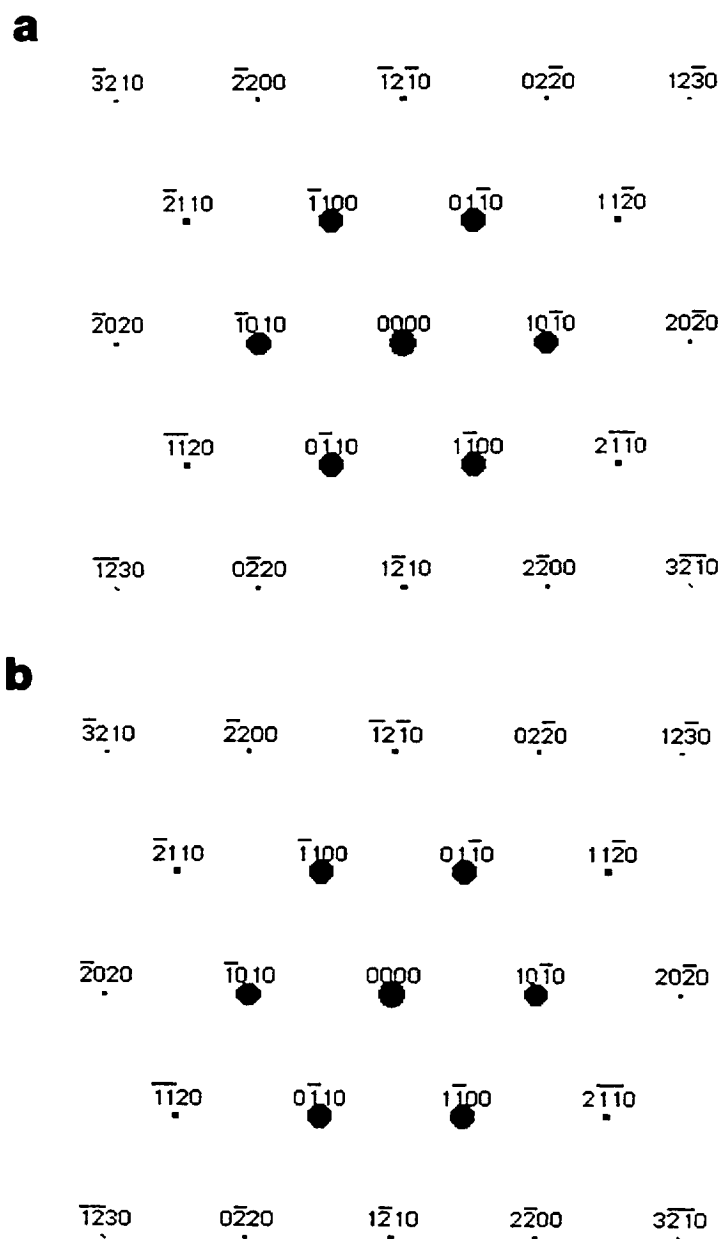


Figure 49: Simulated diffraction patterns with a zone axis of (0001) for (a) MoC and (b) Mo<sub>2</sub>C. Information for atom locations and lattice constants taken from [75].

and homogenized NiAl-0.1Mo ingots as  $\text{Mo}_2\text{C}$  [47]. Weaver's TEM observations provided an orientation relationship of  $[111]_{\text{NiAl}} / [11\bar{2}0]_{\text{Mo}_2\text{C}}$  and  $(01\bar{1})_{\text{NiAl}} / (000\bar{1})_{\text{Mo}_2\text{C}}$  between the precipitate and the NiAl matrix. The angles between the  $\{011\}$ -type planes are 0, 60, and 90°. Observations of the Widmanstätten-type precipitation in Figures 41-44 correspond well with these relations. With limited information available for the Ni-Al-Mo-C system, the accuracy of the diffraction results are questionable. The presence of other elements, Ni and Al, could alter the lattice parameters of the carbides or could stabilize one of the high temperature carbides in the Mo-C binary system (Figure 50). EDS proved ineffective in the identification of phases due to our limited ability to detect carbon.

As a result of this uncertainty in the number of carbides present in the NiAl-Mo-C system, developing phase constitution relationships is difficult. From Figures 21(a) and 22 (a), the compositional regions of arc-melted specimens are nearly identical for the spline and "sheet" two-phase structure. In addition, the presence of the "fine" two-phase constituent was observed in every explored composition of the NiAl-Mo-C system. It is possible that the "sheet" and "fine" structures are the same phase but with a different morphology. Although the "fine" constituent appears to consist of short aspect rods (Figure 25), carbides were observed which showed branching and rod-lamellar transitions (Figure 27, 29, 30, 35). The rod-lamellar, or rod-plate, transition has been shown to occur in certain faceted alloys and eutectic systems [76]. In fact, this behavior was observed in the NiAl-34Cr, NiAl-9Mo, and Ni-22W eutectic alloys.

The information provided by the DTA of the slow cooled and directionally solidified ingots does not verify the presence of a eutectic reaction within the NiAl-Mo-C system. Microstructurally, the samples are completely different after the DTA than before. Only NiAl dendrites with small precipitates and interdendritic NiAl-9Mo

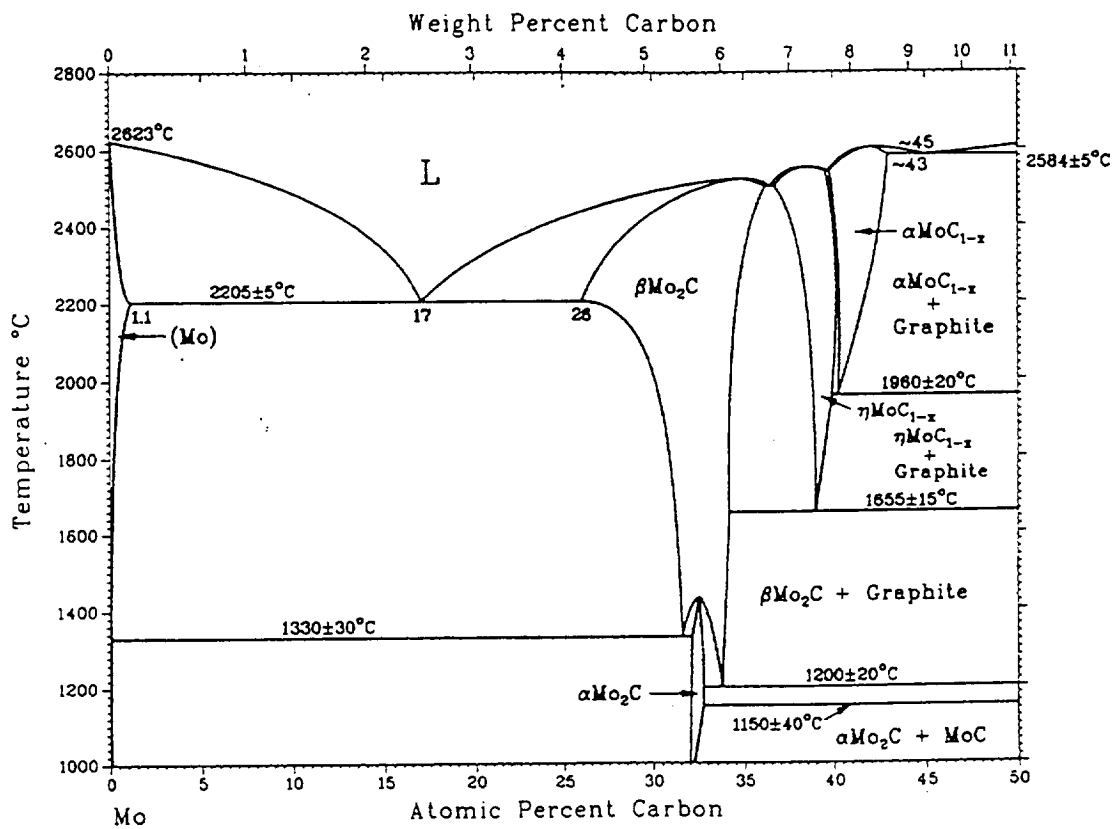


Figure 50: Phase diagram for the molybdenum-carbon system [5].

eutectic are observable. The lack of any carbides in all of the DTA samples suggest that the carbon was lost during differential thermal analysis. If the flowing helium gas were of insufficient purity, i.e. high oxygen content, the small amount of carbon present in the sample could be lost in the liquid state. Further investigation of this phenomenon is required.

The directionally solidified ingots are of particular interest. Although Ingots MoC #2 and MoC #3 were successfully directionally solidified, the microstructures varied along the length of the ingot. During containerless directional solidification, the solute content of the liquid zone will increase for off-eutectic compositions. This general behavior was observed in both ingots. Near the first zone, Figure 45 (a), the microstructure consisted of an NiAl matrix with a fine dispersion of carbides along the grain boundaries. After further processing, the volume fraction of the carbide began to increase, Figure 45 (b). Near the end of processing in both ingots, the microstructures of Figures 45 (c) and (d) were common. These structures are similar in appearance to the Widmanstätten precipitation observed during heat treating. This microstructure was also observed in the spill of Ingot MoC #4 shown in Figure 46 (b). It was difficult to determine if these structures were the result of solidification or precipitation, or both processes.

Ingot MoC #4, with only limited directional solidification, provided an extensive amount of information. From Figure 46 (a), it is clear that this composition contained graphite flakes. As previously discussed in Chapter 3, graphite was shown to cause difficulty during directional solidification due to its high emissivity. In addition, the aligned carbides were shown to be similar in appearance to those observed in the slow cooled ingots and in the directionally solidified MoC #2 and MoC #3 ingots (Figure 46 (c)).

Although a true pseudo-binary eutectic reaction may exist between NiAl and a molybdenum carbide, this investigation has not verified its presence. The evidence points to a broken lamellar eutectic, but the formation of the extensive Widmanstätten precipitate may be confusing the results. In fact, the exact nature of the phase diagram is uncertain and more investigations are required. There is little doubt that an hexagonal carbide is a stable phase.

While no changes were caused by the heat treatments at 1473 K, the microstructures changed dramatically at temperatures of 1603, 1623, and 1723 K. At these temperatures, Widmanstätten precipitation, spheroidization of graphite, and finer carbides were observed. This suggests that the carbides went into solution during annealing above 1600 K and precipitated upon cooling. This is also consistent with the DTA results showing a break near 1600 K.

The presence of the spline after the high temperature anneal proved to be an issue of debate and uncertainty. In the NiAl-28Cr-6Mo system, precipitates of NiAl were observed in the (Cr, Mo) phase. However, in the NiAl-34Cr system containing no molybdenum, no precipitates were detected [2]. Due to the rapid solidification around the carbide, the NiAl is likely much lower in carbon and molybdenum than the remaining liquid. The lack of molybdenum in solution may inhibit the dissolution of graphite in the NiAl. Further investigations are required to substantiate this.

## CHAPTER 5

### MECHANICAL PROPERTIES OF NiAl-Mo-C ALLOYS

#### Introduction

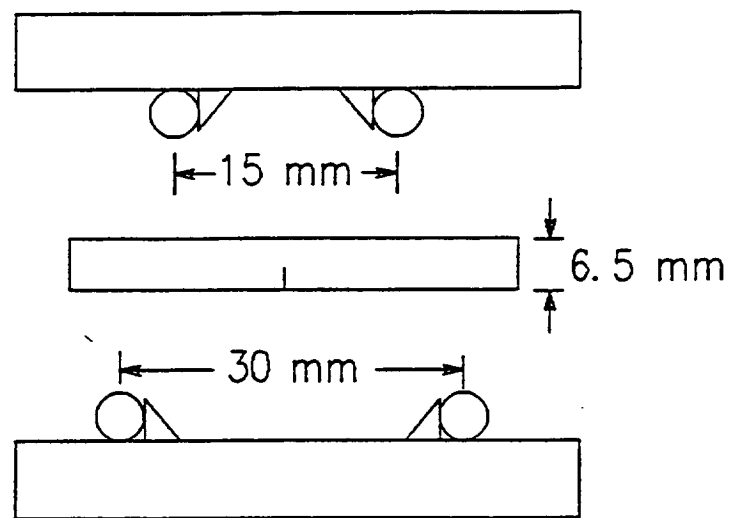
Selected ingots were tested for mechanical properties as a final evaluation of processed materials. Arc-melted ingots were limited by the size and general homogeneity of the microstructures. Larger ingots processed by slow cooling or directional solidification were therefore considered for four-point flexure testing and elevated temperature compression.

#### Experimental Procedures

##### Flexure testing

Directionally solidified ingots MoC #2 and MoC #3 were evaluated for room temperature fracture toughness by four-point flexure testing. Electrical discharge machining (EDM) was used to machine the directionally solidified ingots into rectangular bend specimens. The bend specimen geometry and testing fixture are illustrated in Figure 51 [2]. Surface damage was removed by wet grinding to 2400 grit SiC. Specimens were notched perpendicular to the growth direction. Tests were performed on an Instron 1000 pound load tensile frame at a constant crosshead rate of 0.01 in/min. A K calibration for pure bending was used to calculate the room temperature fracture toughness [77]. The outer fiber stress for each specimen was also calculated.

Fracture surfaces of several specimens were examined using scanning electron microscopy. Samples were examined at 20 KeV in either backscattered (BSE),



SAMPLE SIZE: 4.5 mm x 6.5 mm x 40 mm  
NOTCH: 2.00 mm x 0.35 mm

Figure 51: Geometry of the four-point flexure testing fixture and bend sample [2].

secondary (SE), or mixed (MIX) modes of operation on a Cambridge Stereoscan 120 SEM.

### Compression testing

Directionally solidified Ingots MoC #2 and MoC #3 were also evaluated for creep strength. In addition, samples were also taken from Ingot SC-7. Compression specimens, 5 mm diameter by 10 mm in length, were electrical discharge machined from the cast or directionally solidified ingots with the compression axis parallel to the growth direction. The compression test were conducted at the NASA Lewis Research Center. Evaluation of the creep resistance was performed at 1200 and 1300 K. Appraisal of the oxidation resistance was also performed simultaneously by conducting the test in air.

## **Results**

### Room temperature fracture toughness

Load-displacement curves for each test specimen are presented in Appendix C. A region of constant load may be observed for each sample. This load corresponds to the weight of the flexure assembly with the constant condition relating to removal of a gap between the tensile frame and the assembly. Results of the flexure testing for the directionally solidified and slow cooled ingots are presented in Table 6. Fracture toughness values range from 10.4 to 13.5 MPa $\sqrt{m}$  for the directionally solidified samples, while the slowed cooled ingots were much lower. Included with the fracture toughness values are the outer fiber stress for each specimen. In addition, one-half of the specimens exhibited crack arrest, i.e. both halves of the fracture specimen remained connected after fracture.

Table 6: Four point flexure results for containerless directionally solidified and slow cooled NiAl-Mo-C ingots.

Sample Number	$K_I^a$ (MPa $\sqrt{m}$ )	$\sigma^b$ (MPa)	Crack Arrest (Yes/No)
MoC2-1	12.4	133	Yes
MoC2-2	10.9	122	No
MoC2-3	13.4	144	No
MoC2-4	11.1	128	Yes
MoC2-5	12.0	139	Yes
MoC2-6	10.9	106	Yes
MoC2-7	10.6	121	Yes
MoC2-8	12.9	149	No
MoC3-1	11.5	128	Yes
MoC3-2	13.5	155	No
MoC3-3	12.7	156	No
MoC3-4	12.1	143	No
MoC3-5	11.8	127	No
MoC3-6	10.4	116	Yes
SC7-1	6.3	79.5	Yes
SC7-2	7.6	101	Yes

<sup>a</sup> Fracture toughness for pure bending [77]

<sup>b</sup> Outer fiber stress

Fracture surfaces examined by scanning electron microscopy exhibited cleavage-type fracture behavior. Figure 52 is a backscattered SEM micrograph near the notch showing the crack origin and bright carbides distributed across the fracture surface. The carbides do not appear to have affected the crack growth through the material. Although some pull-out of the carbides was observed, the benefits would have been minimal due to the low volume fraction (Figure 53-54). Microstructurally, the notches were placed in regions containing a fine dispersion of carbons in a polycrystalline NiAl matrix, as in Figure 45 (b). Observations were also made of peculiar cleavage behavior (Figure 55), but in general the fracture appeared to be transgranular.

#### Elevated temperature strength

The flow stress and strain rate,  $\dot{\epsilon}$ , data were fitted to a temperature compensated-power law equation:

$$\dot{\epsilon} = A\sigma^n \exp(-Q / RT)$$

where A is a constant,  $\sigma$  is the applied true stress (MPa), Q is the activation energy for deformation (kJ/mol), T is the absolute temperature, R is the gas constant ( $8.314 \times 10^{-3}$  kJ/mol-K), and n is the stress exponent. The creep results for the directionally solidified and slow cooled NiAl-Mo-C ingots are compared to stoichiometric single crystal NiAl in Table 7 [78]. In Figure 56, the 1300 K compressive behavior of the NiAl-Mo-C alloys are compared to single crystal NiAl [78] and a nickel-based single crystal superalloy [79]. The compressive stress-compressive strain curves are presented in Appendix D. Creep specimens were sectioned from the directionally solidified ingots near the last zone. Although these regions of the DS ingots were shown to consist of partially aligned carbides in a polycrystalline NiAl matrix, the exact microstructures of each creep test specimen was not determined.

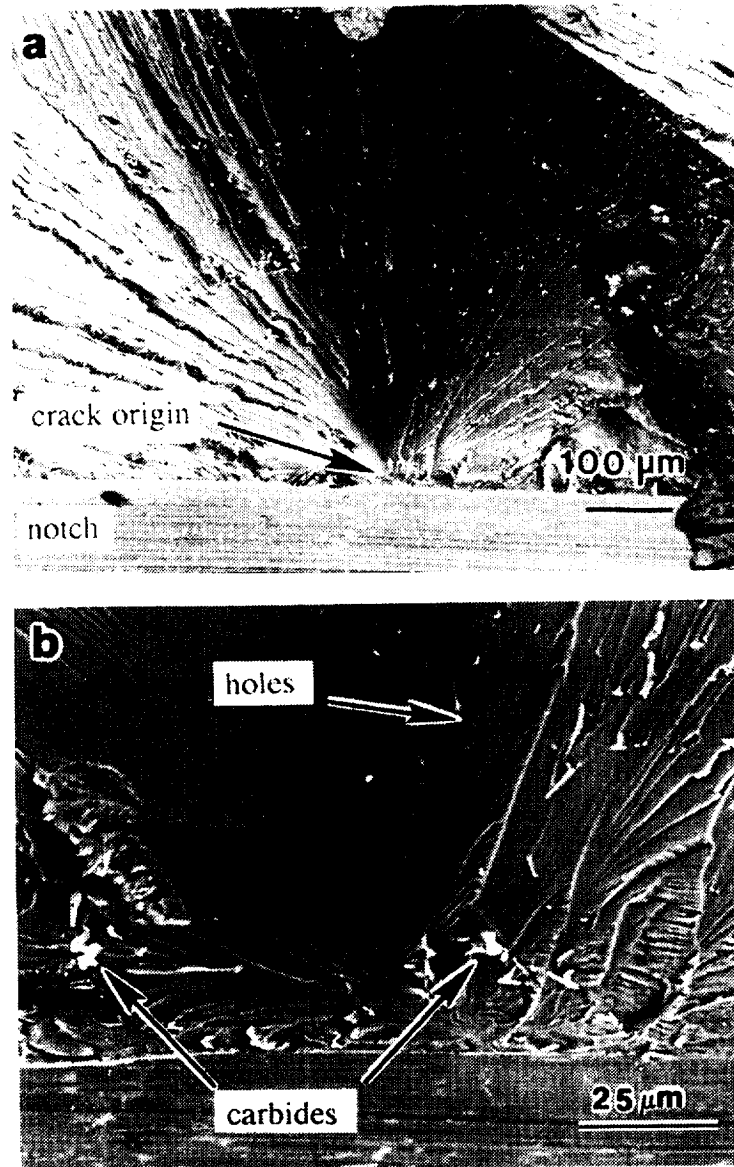


Figure 52: Backscattered SEM micrograph of a fracture surface from a directionally solidified NiAl-1Mo-0.73C bend specimen.

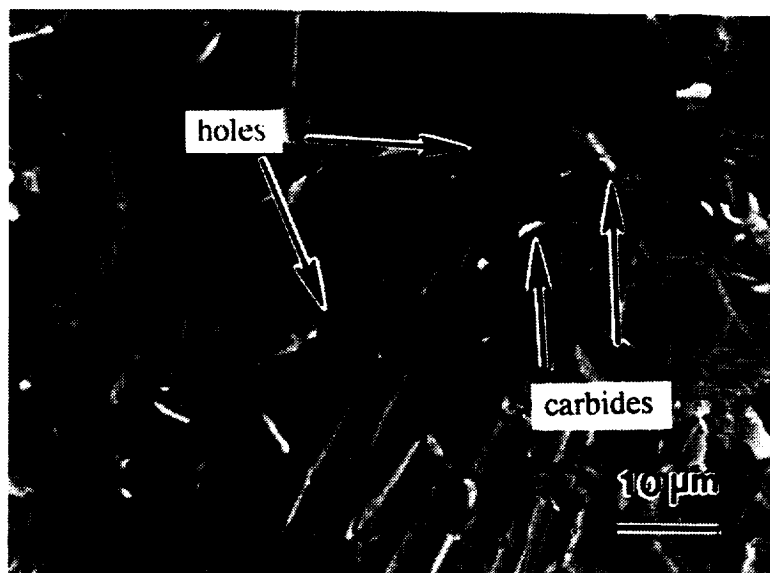


Figure 53: Backscattered SEM micrograph of a fracture surface from a directionally solidified NiAl-1Mo-0.73C bend specimen.

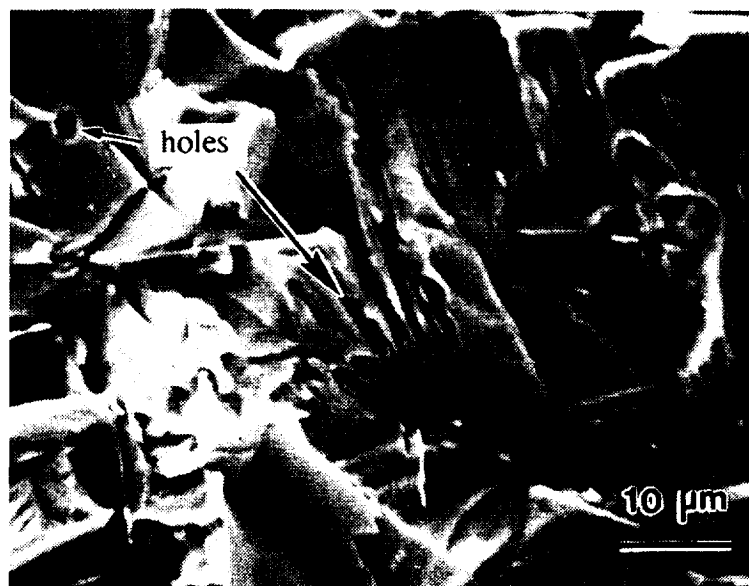


Figure 54: Secondary SEM micrograph of a fracture surface from a directionally solidified NiAl-1Mo-0.61C bend specimen.

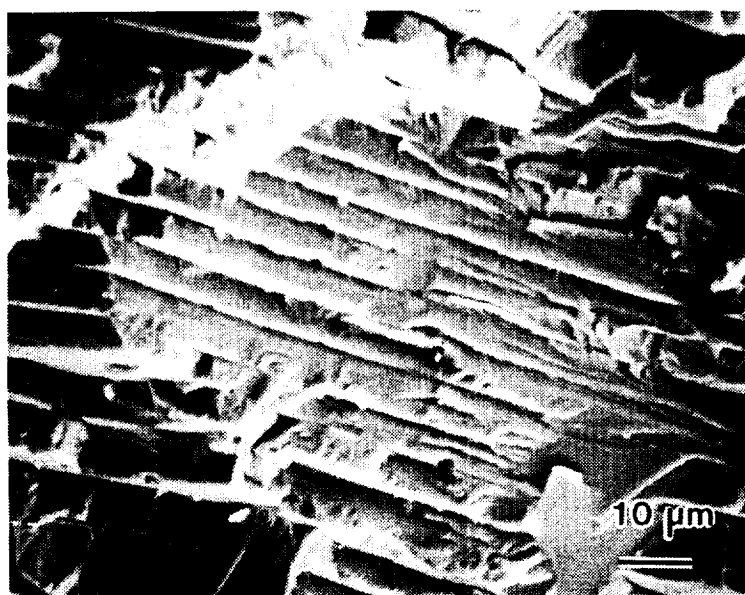


Figure 55: Secondary SEM micrograph of a fracture surface from a directionally solidified NiAl-1Mo-0.61C bend specimen.

Table 7: Representative creep behavior of NiAl-Mo-C alloys compared to stoichiometric single crystal NiAl.

Alloy	Representative Creep Behavior
NiAl [001] (Ni-50Al)	1100-1300 K $\dot{\epsilon} = 1480\sigma^{6.3}\exp(-439.3 / RT)$ [78]
NiAl-Mo-C (DS) (NiAl-1Mo-0.73C) (NiAl-1Mo-0.61C)	1200-1300 K $\dot{\epsilon} = 53.54\sigma^{7.53}\exp(-478.4 / RT)$
NiAl-Mo-C (SC) (NiAl-1Mo-1C)	1100-1300 K $\dot{\epsilon} = 741000\sigma^{7.44}\exp(-594.6 / RT)$

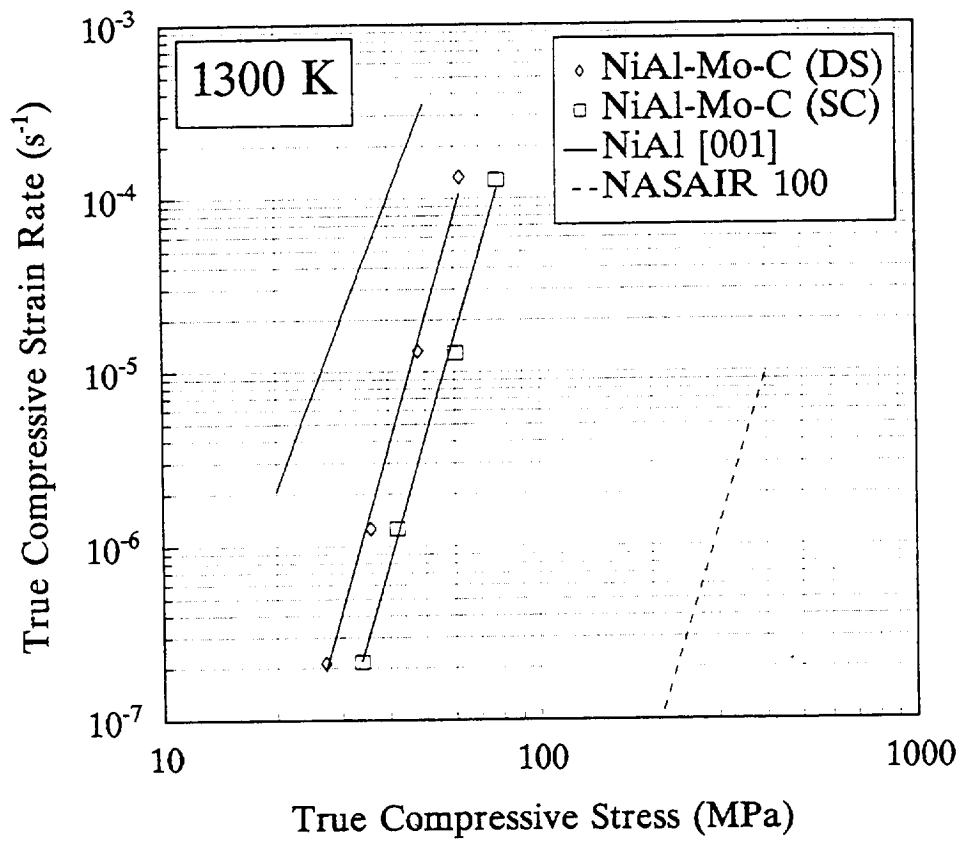


Figure 56: 1300 K compressive flow stress-strain rate behavior for directionally solidified NiAl-Mo-C compared to NiAl and NASAIR 100 [78, 79].

### Discussion

The fracture toughness values for the NiAl-Mo-C ingots are much higher than values of 4 to 6 MPa $\sqrt{m}$  typically observed in polycrystalline NiAl [33-38]. Typical fracture behavior in NiAl is intergranular fracture, but the NiAl-Mo-C specimens exhibited a transgranular behavior. The crack arrest behavior may be associated with the pull-out observed in Figures 53-54. As stated previously, this effect would be very limited due to the low volume fraction of reinforcement. The increased fracture toughness may be justified by second-phase toughening or gettering of impurities. Darolia has shown that limited additions of molybdenum to NiAl increase the ductility [1]. Directionally solidified ingots MoC #2 and #3 contained no graphite flakes. In fact, these ingots are not within the graphite region for arc-melts (Figure 21 (b)). It is therefore possible that all of the carbon has reacted with the molybdenum to form carbides. Flexure testing of directionally solidified ingots of varying composition may verify this theory.

While some of the NiAl-based eutectic systems have shown dramatic improvements in the creep strength, the NiAl-Mo-C system exhibited only a limited improvement. In terms of microstructure, the mechanical test specimens were not of the desired morphology due to difficulties during directional solidification. The optimum structure would be the aligned carbide structure observed in Figures 32 and 33. In general, Ingot SC-7 (NiAl-1Mo-1C) possessed this type of structure and did provide better creep resistance than the directionally solidified NiAl-Mo-C ingots.

Volume fractions for this systems are much lower than those for the other NiAl-based eutectic systems, especially in the directionally solidified ingots. By increasing the volume fraction of the reinforcing phases, improved mechanical properties may be achieved.

The goal of this research was to develop NiAl-carbide eutectic systems with low densities and mechanical properties better than unalloyed nickel aluminide. Although it is likely that a eutectic alloy of low volume fraction discontinuous phase has been observed, both the creep strength and room temperature fracture toughness were improved. Figure 57 is a modification of Figure 4. The NiAl-Mo-C system has been included with the NiAl-based eutectic systems. While the improvement is limited, it should be noted that the optimum morphology, volume fraction, and processing conditions were not achieved for this alloy system.

It should be noted that the information plotted in Figures 4 and 57 are for screening purposes only. More accurate methods should also be considered. For example, the use of room temperature fracture toughness as the x-axis may be misleading. This value does not take into account the effect of yield strength on the mechanical behavior of these alloys. A more accurate value to use would be the critical crack length,  $a_c$ . The critical crack length is proportional to  $(K_1/\sigma_{ys})^2$ , where  $K_1$  is the room temperature fracture toughness and  $\sigma_{ys}$  is the room temperature yield strength [80, 81]. In addition, a similar method of normalization could be performed on the y-axis by dividing the creep strength by the room temperature ultimate tensile strength. Although these techniques may provide a more accurate perspective in terms of component design, much of the mechanical property information required for these plots is currently unavailable for the systems presented in Figure 57.

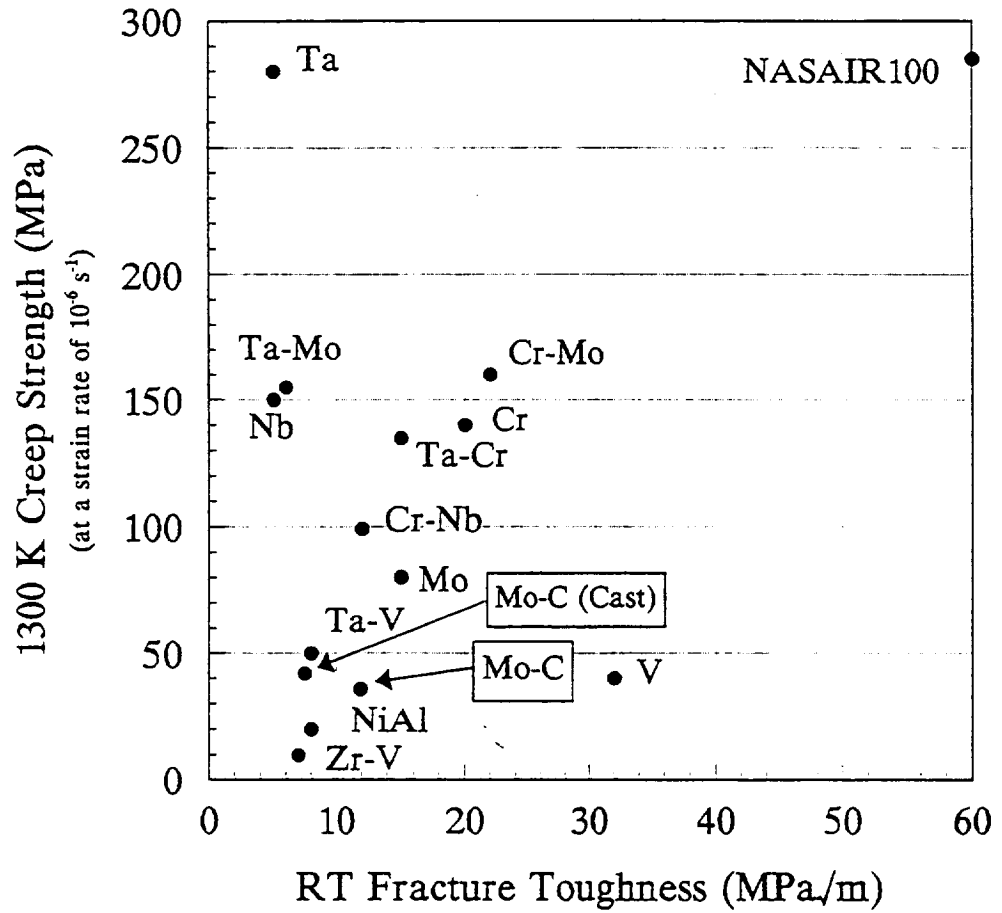


Figure 57: Performance plot of various NiAl-based eutectic systems directionally solidified at the University of Tennessee with the NiAl-Mo-C system included, modified from [24].

## CHAPTER 6

### SUMMARY

#### Conclusions

1. The melting of Ni-Al-refractory-metal-carbon systems is best achieved by reacting the carbon with the nickel then with the other components.
2. Of the NiAl-carbide systems examined, the NiAl-Mo-C system had the most appealing microstructures for use as an in-situ composite.
3. Arc-melting economically provided a wide range of compositions for the NiAl-Mo-C system. These ingots provided phase relationships and solidification behavior through microstructural characterization.
4. Slow cooled ingots provided additional phase relations and more material for subsequent testing. Conditions during solidification were closer to equilibrium than those for arc-melting.
5. In-situ reaction of graphite with the liquid zone during containerless processing was not successful.
6. Two ingots, NiAl-1Mo-0.61C and NiAl-1Mo-0.73C, were successfully processed by containerless means.
7. Attempts at directionally solidifying NiAl-1Mo-1C ingots failed due to the formation of a heavy coating of high emissivity on the liquid zone during processing.
8. Small variations in composition (<0.1 at.%) produced dramatic changes in the microstructure of the NiAl-Mo-C system.

9. Morphology, solidification behavior, and volume fraction all support the existence of a broken lamellar eutectic in the NiAl-Mo-C system, most likely with MoC.
10. Heat treatments reveal Widmanstatten precipitation of molybdenum carbides at approximately 60 and 90° angles.
11. The NiAl-Mo-C system contains several unique microstructures which have not been observed in other NiAl-based systems.
12. Splines are broken lamellar sheets which under unknown conditions may produce a regular "lattice-work" morphology.
14. The spline, along with the NiAl sheath, remains after high temperature annealing.
15. Although x-ray diffraction has identified MoC, more than one carbide may possibly be present.
16. Directionally solidified NiAl-Mo-C alloys demonstrated improvements in both the room temperature fracture toughness and creep strength compared to stoichiometric single crystal NiAl.
17. Further investigations of this system are required to clarify issues.

### **Recommendations**

Directional solidification of additional compositions would provide phase relationships, solidification behavior, and mechanical property data. This may be achieved by means other than containerless processing. A modified Bridgman technique may offer a more successful processing route. Mechanical property data for optimum conditions, i.e. volume fraction, morphology, and processing technique, would likely produce results better than those evaluated in this study. Higher velocity solidification could develop more optimum structures.

Further investigation of the Widmanstatten precipitation may produce a heat treatable alloy. Detailed transmission electron microscopy on heat treated and as-processed alloys would be beneficial to phase and orientation relationships.

Additional NiAl-carbide systems of interest may exist. More exploratory melts are necessary. The interaction of carbon with the NiAl-based eutectics requires work as well. It may be possible to produce precipitation of carbides in these structures.

**LIST OF REFERENCES**

## LIST OF REFERENCES

1. R. Darolia, "NiAl Alloys for High-Temperature Structural Applications," *JOM*, **43** [3], (1991), 44-49.
2. D. R. Johnson, "Processing and Mechanical Properties of NiAl-Based In-Situ Composites," Ph.D Dissertation, University of Tennessee, (1994).
3. S. M. Joslin, "NiAl and NiAl-Based Composites Directionally Solidified by a Containerless Zone Process," Ph.D. Dissertation, University of Tennessee, (1994).
4. P. Schwarzkopf and R. Kieffer, Refractory Hard Metals: Borides, Carbides, Nitrides, and Silicides, The MacMillan Company, New York (1953).
5. M. F. Singleton, J. L. Murray, and P. Nash, "NiAl", in Binary Alloy Phase Diagrams, T. B. Massalski, Ed., American Society for Metals, Metals Park, OH, (1986), 140-143.
6. D. B. Miracle, "The Physical and Mechanical Properties of NiAl," *Acta Metall. Mater.*, **41** [3], (1993), 649-684.
7. K. Vedula, V. Pathare, Aslanidis, and R. H. Titran, "Alloys Based on NiAl for High Temperature Applications," in High Temperature Ordered Intermetallic Alloys, C. C. Koch, C. T. Liu, and N. S. Stoloff, Eds., Materials Research Society Symp. Proc. Vol. 39, Pittsburgh, PA, (1985), 411-421.
8. A. Taylor and N. J. Doyle, "Further Studies on the Nickel-Aluminum System I. The  $\beta$ -NiAl and  $\delta$ -Ni<sub>2</sub>Al<sub>3</sub> Phase Fields," *J. Appl. Cryst.*, **5**, (1972), 201-209.
9. P. Georgopoulos and J. B. Cohen, "The Defect Structure and Debye Waller Factors vs. Composition in  $\beta$  Ni<sub>1±x</sub>Al<sub>1±x</sub>," *Scripta Metall.*, **11**, (1977), 147-150.
10. A. J. Bradley and A. Taylor, "An X-ray Analysis of the Nickel-Aluminum System," *Proc. R. Soc. (London)*, **A159**, (1937), 56-72.
11. L. N. Guseva, "On the Nature of the  $\beta$ -phase in the System Ni-Al," *Doklady Akad. Nauk. S.S.S.R.*, **77**, (1951), 415-418.
12. M. J. Cooper, "An Investigation of the Ordering of the Phases CoAl and NiAl," *Philos. Mag.*, **8**, (1963), 805-810.
13. G. S. Sauthoff, "Intermetallic Alloys-Overview on New Materials Developments for Structural Applications in West Germany," *Z. Metallk.*, **81**, (1990), 855-861.
14. G. S. Sauthoff, "Mechanical Properties of Intermetallics at High Temperatures," in High Temperature Aluminides and Intermetallics, S. H. Whang, C. T. Liu, D. P. Pope, and J. O. Stiegler, Eds., The Minerals, Metals and Materials Society, Warrendale, PA, (1990), 329-352.
15. W. S. Walston and R. Darolia, "Effect of Alloying on Physical Properties of NiAl," in High Temperature Ordered Intermetallic Alloys V, I. Baker, R. Darolia, J. D. Whittenberger, and M. H. Yoo, Eds., Materials Research Society Symp. Proc. Vol. 288, Pittsburgh, PA, (1993), 237-242.
16. J. D. Cotton, R. D. Noebe, and M. J. Kaufman, "NiAl-Rich Portion of the NiAl-Cr Pseudobinary Eutectic System," *J. Phase Equil.*, **14**, (1993), 579-582.

17. J. D. Cotton, R. D. Noebe, and M. J. Kaufman, "Ternary Alloying Effects in Polycrystalline  $\beta$ -NiAl," in International Symposium on Structural Intermetallics, R. Darolia, J. J. Lewandowski, C. T. Liu, P. L. Martin, D. B. Miracle, and M. V. Nathal, Eds., The Minerals, Metals and Materials Society, Warrendale, PA, (1993), 513-522.
18. E.-T. Henig and H. L. Lukas, "Kalorimetrische Bestimmung der Bildungsenthalpie und die Beschreibung der Fehlordnung der Geordneten b-Phase (Ni,Cu)<sub>1-x</sub>Al<sub>x</sub>," *Z. Metallk.*, **66**, (1975), 98-106.
19. R. W. Cahn, "Load-Bearing Ordered Intermetallic Compounds-A Historical View," *MRS Bulletin*, XVI [5], (1991), 44-49.
20. R. D. Field, D. F. Lahrman, and R. Darolia, "Slip Systems in  $\langle 001 \rangle$  Oriented NiAl Single Crystals," *Acta Metall. Mater.*, **39**, (1991), 2951-2959.
21. M. Dollar, S. Dymek, S. J. Hwang, and P. Nash, "The Occurrence of  $\langle 110 \rangle$  Slip in NiAl," *Scripta Metall. Mater.*, **26**, (1992), 29-43.
22. R. T. Pascoe and C. W. A. Newey, "Deformation Processes in the Intermediate Phase NiAl," *Met. Sci. J.*, **5**, (1971), 50-55.
23. M. J. Mills and D. B. Miracle, "The Structure of  $a \langle 100 \rangle$  and  $a \langle 110 \rangle$  Dislocation Cores in NiAl," *Acta Metall. Mater.*, **41**, (1993), 85-95.
24. R. D. Noebe, "The Effect of Various Metallurgical Parameters on the Flow and Fracture Behavior of Polycrystalline NiAl Near the Brittle-To-Ductile Transition," NASA Technical Memorandum 106534, NASA Lewis Research Center, Cleveland, Ohio (April 1994).
25. M. H. Loretto and R. J. Wasilewski, "Slip Systems in NiAl Single Crystals at 300°K and 77°K," *Philos. Mag. Lett.*, **62**, (1971), 1311-1328.
26. R. R. Bowman, R. D. Noebe, and R. Darolia, "Mechanical Properties and Deformation Mechanisms of NiAl," in HITEMP Review-1989: Advanced High Temperature Engine Materials Technology Program, NASA CP-10039 (1989), 47-1 to 47-15.
27. R. J. Wasilewski, S. R. Butler, and J. E. Hanlon, "Plastic Deformation of Single Crystal NiAl," *Trans. Metall. Soc. AIME*, **239**, (1967), 1357-1364.
28. R. T. Pascoe and C. W. A. Newey, "Deformation Modes of the Intermediate Phase NiAl," *Phys. Status Solidi*, **29**, (1968) 357-366.
29. P. Veysiere and R. D. Noebe, "Weak-Beam Study of  $\langle 111 \rangle$  Superlattice Dislocations in NiAl," *Philos. Mag.*, **65**, (1992), 1-13.
30. J. T. Kim and R. Gibala, "Slip Transition in  $[001]$  Oriented NiAl at High Temperatures," in High Temperature Ordered Intermetallic Alloys IV, L. Johnson, Ed., Materials Research Society Symp. Proc. Vol. 213, Pittsburgh, PA, (1993), 261-266.
31. R. D. Field, D. F. Lahrman, and R. Darolia, "A Mechanistic Study of the Microalloying Effect in NiAl Base Alloys," in High Temperature Ordered Intermetallic Alloys V, I. Baker, R. Darolia, J. D. Whittenberger, and M. H. Yoo, Eds., Materials Research Society Symp. Proc. Vol. 288, Pittsburgh, PA, (1993), 423-428.
32. R. D. Noebe, R. R. Bowman, and M. V. Nathal, "Review of the Physical and Mechanical Properties of the B2 compound NiAl," *International Materials Reviews*, **38** [4], (1993), 193-232.

33. J. J. Lewandowski, G. M. Michal, I. E. Locci, J. D. Rigney, "Fracture Toughness and the Effects of Stress State on Fracture of Nickel Aluminides," in Alloy Phase Stability and Design, G. M. Stocks, D. P. Pope, and A. F. Giamei, Eds., Materials Research Society Symp. Proc. Vol. 186, (1991), 341-347.
34. K.S. Kumar, S. K. Mannan, J. D. Whittenberger, R. K. Viswanadham, and L. Christodoulou, "Nickel Aluminide/Titanium Diboride Composites Via XD Synthesis," MML TR 89-102(C), Martin Marietta Corp., Baltimore, MD,(1989).
35. K. S. Kumar, S. K. Mannan, and R. K. Viswanadham, "Fracture Toughness of NiAl and NiAl-Based Composites," *Acta Metall. Mater.*, **40**, (1992), 1201-1222.
36. S. M. Russell, C. C. Law, M. J. Blackburn, P. C. Clapp, and D. M. Pease, "Lightweight Disk Alloy Development," PWA-FR-19577-8, Pratt and Whitney, West Palm Beach, FL, (1989).
37. S. Reuss and H. Vehoff, "Temperature Dependence of the Fracture Toughness of Single Phase and Two Phase Intermetallics," *Scr. Metall. Mater.*, **24**, (1990), 1021-1026.
38. W. A. Kaysser, R. Laag, J. C. Murray, and G. E. Petzow, ",", *Int. J. Powder Metall.*, **27** (1991), 43-49.
39. K. -M. Chang, R. Darolia, and H. A. Lipsitt, "Fracture of B2 Aluminide Single Crystals," in High Temperature Ordered Intermetallic Alloys IV, L. Johnson, Ed., Materials Research Society Symp. Proc. Vol. 213, Pittsburgh, PA, (1993), 597-602.
40. R. Darolia, R. D. Field, R. D. Noebe, A. Garg, and W. S. Walston, "A Mechanistic Study of Microalloying Effects in NiAl," AFOSR Final Report, Contract F49620-91-C-0077, March, (1995).
41. J. E. Hack, J. M. Brzeski, and R. Darolia, "Evidence of Inherent Ductility in Single Crystals of the Ordered Intermetallic Compound NiAl," *Scripta Metall. Mater.*, **27**, (1992), 1259-1263.
42. D. R. Johnson, S. M. Joslin, B. F. Oliver, R. D. Noebe, and J. D. Whittenberger, "High Purity NiAl Single Crystals and Composites by Containerless Automated Processing," in First International Conference on Processing Materials for Properties, H. Henein and T. Oki, Eds., The Minerals, Metals and Materials Society, Warrendale, PA, (1993), 865-870.
43. H. K. DeMarco and A. J. Ardell, "Mechanical Behavior of Monocrystalline NiAl Using A Miniaturized Disk-Bend Test," in High Temperature Ordered Intermetallic Alloys V, I. Baker, R. Darolia, J. D. Whittenberger, and M. H. Yoo, Eds., Materials Research Society Symp. Proc. Vol. 288, Pittsburgh, PA, (1993), 641-646.
44. P. R. Strutt, R. S. Polvani, and B. H. Kear, "Dynamic Strain Ageing in Creep of  $\beta$ -NiAl," *Scripta Metall.*, **7**, (1973), 949-954.
45. M. L. Weaver, M. J. Kaufman, and R. D. Noebe, "The Effects of Alloy Purity on the Mechanical Behavior of Soft Oriented NiAl Single Crystals," *Scripta Metall. Mater.*, **29**, (1993), 1113-1118.
46. M. L. Weaver, R. D. Noebe, J. J. Lweandowski, B. F. Oliver, and M. J. Kaufman, "The Effects of Interstitial Content, Heat Treatment, and Prestrain on the Tensile Properties of NiAl," *Materials Science and Engineering A*, **A192/193**, (1995), 179-185.
47. M. L. Weaver, "Investigation of Strain Aging in the Ordered Intermetallic Compound  $\beta$ -NiAl," Ph.D. Dissertation, University of Florida, (1995).

48. E. Schulson and D. R. Barker, "A Brittle to Ductile Transition in NiAl of a Critical Grain Size," *Scripta Metall.*, **17**, (1983), 519-522.
49. N. S. Stoloff, "Toughening Mechanisms in Intermetallics," *Metall. Trans A*, **24A** (1993) 561-567.
50. C. C. Law and M. J. Blackburn, "Rapidly Solidified Lightweight Durable Disk Material," Final Technical Report, AFWAL-TR-87-4102, Pratt and Whitney Aircraft, East Hartford, CT, (1987).
51. G. Sauthoff, "High Temperature Deformation and Creep Behavior of BCC Based Intermetallics," in Intermetallic Compounds - Structure and Mechanical Properties (JIMIS-6), O. Izumi, Ed., Japan Institute of Metals, Sendai, Japan, (1991) 371-378.
52. J. D. Whittenberger, E. Arzt, and M. J. Luton, "Compressive Properties of a Reaction Milled NiAl-AlN Composite," *J. Mater. Res.*, **5**, (1990), 2819-2827.
53. H. E. Cline, J. L. Walter, E. Lifshin, and R. R. Russell, "Structures, Faults, and the Rod-Plate Transition in Eutectics," *Metall. Trans.*, **2**, (1971), 189-194.
54. P. W. Pelligrini and J. J. Hutta, "Investigations of Phase Relations and Eutectic Directional Solidification on the NiAl-V Join," *J. Crystal Growth*, **42**, (1977), 536-539.
55. F. E. Heredia, M. Y. He, G. E. Lucas, A. G. Evans, H. E. Deve, and D. Konitzer, "The Fracture Resistance of Directionally Solidified Dual-Phase NiAl Reinforced with Refractory Metals," *Acta Metall. Mater.*, **41** [2], (1993), 505-511.
56. R. D. Reviere, B. F. Oliver, and D. D. Bruns, "Computer Controlled Containerless Processing of High Temperature Intermetallic Compounds," *Mat. Manuf. Process.*, **4** [1], (1989), 103-131.
57. R. D. Reviere, "Ductilization of Single Phase TiAl Via Ternary and Quaternary Additions," Ph.D. Dissertation, University of Tennessee, (1992).
58. R. D. Noebe, NASA Lewis Research Center, Personal Communication, (1994).
59. J. D. Whittenberger, R. D. Reviere, R. D. Noebe, B. F. Oliver, "Compressive Strength of Directionally Solidified NiAl-NiAlNb Intermetallics at 1200 and 1300 K," *Scripta Metall. Mater.*, **26**, (1992), 987-992.
60. D. R. Johnson, S. M. Joslin, B. F. Oliver, R. D. Noebe, J. D. Whittenberger, "Intermetallic/Metallic Polyphase In-Situ Composites," in Intermetallic Matrix Composites II, D. Miracle, J. Graves, and D. Anton, Eds., Materials Research Society Symp. Proc. Vol. 273, Pittsburgh, PA, (1992), 87-92.
61. J. C. Schuster, and H. Nowotny, "The Ternary System Nickel-Aluminum-Carbon," *Monatsh. Chem.*, **113**, (1982), 163-170.
62. S. Sridharan, H. Nowotny, and S. F. Wayne, "Investigations Within the Quaternary System Titanium-Nickel-Aluminum-Carbon," *Monatsh. Chem.*, **114**, (1983), 127-135.
63. G. V. Samsonov and I. M. Vinitskii, Handbook of Refractory Compounds, IFI/Plenum, New York, (1980).
64. T. Ya. Kosolapova, Carbides: Properties, Production, and Applications, Plenum Press, New York-London, (1971).
65. D. R. Johnson, X. F. Chen, B. F. Oliver, R. D. Noebe, J. D. Whittenberger, "Processing and Mechanical Properties of In-Situ Composites from the NiAl-Cr and NiAl-(Cr,Mo) Eutectic Systems," *Intermetallics*, **3** [2], (1993), 99-113.
66. T. S. Newport, B. F. Oliver, D. R. Johnson, R. D. Noebe, "Containerless Automated Processing of High-purity Intermetallic Compounds and Composites," to be published in *Mat. Manuf. Process.*

67. Handbook of Chemistry and Physics, Robert C. Weast, Ed., CRC Press, Cleveland, Ohio, (1975), E-229 to E-230.
68. F. N. Rhines, Phase Diagrams in Metallurgy: Their Development and Application, McGraw-Hill Book Company, New York, (1956).
69. P. J. Goodhew, Specimen Preparation for Transmission Electron Microscopy of Materials, Oxford University Press, London, (1984), 30-32.
70. A. Czyrska-Filemonowicz and K. Spiradek, *USA Microscopy and Analysis*, March (1995), 23.
71. B. E. Sundquist and L. F. Mondolfo, "Heterogeneous Nucleation in the Liquid-to-Solid Transformation in Alloys," *Trans. Met. Soc. AIME*, **221**, (1961), 157-164.
72. W. Kurz and D. J. Fisher, Fundamentals of Solidification, Trans Tech Publications, Switzerland, (1986), 34-42.
73. M. R. Taylor, R. S. Fidler, and R. W. Smith, "Broken Lamellar Eutectic Growth; Structure of the Silver-Bismuth Eutectic," *J. Crystal Growth*, **3-4**, (1968), 666-673.
74. R. Elliott, Eutectic Solidification Processing: Crystalline and Glassy Alloys, Butterworths, London, (1983), 135-138.
75. P. Villars and L. D. Calvert, Pearson's Handbook of Crystallographic Data for Intermetallic Phases, Volume 2, American Society for Metals, United States of America, (1985), 1550.
76. H. E. Cline, J. L. Walter, E. Lifshin, and R. R. Russell, "Structures, Faults and the Rod-Plate Transition in Eutectics," *Met. Trans.*, **2**, (1971), 189-194.
77. W. F. Brown and J. E. Srwaley, in Plane Strain Crack Toughness Testing of High Strength Metallic Materials, ASTM Special Publication No. 410, ASTM, Philadelphia, PA (1966) 13-14.
78. J. D. Whittenberger and R. D. Noebe, unpublished data, (1991).
79. M. J. Nathal and L. J. Ebert, "Elevated Temperature Creep-Rupture Behavior of the Single Crystal Nickel-Base Superalloy NASAIR 100," *Metall. Trans. A*, **16A**, (1985), 427-439.
80. R. W. Hertzberg, Deformation and Fracture Mechanics of Engineering Materials, John Wiley & Sons, New York, (1989), 304-305.
81. T. L. Anderson, Fracture Mechanics: Fundamentals and Applications 2nd Edition, CRC Press, Boca Raton, (1995).

**APPENDICES**

**APPENDIX A**  
**X-RAY DIFFRACTION RESULTS**

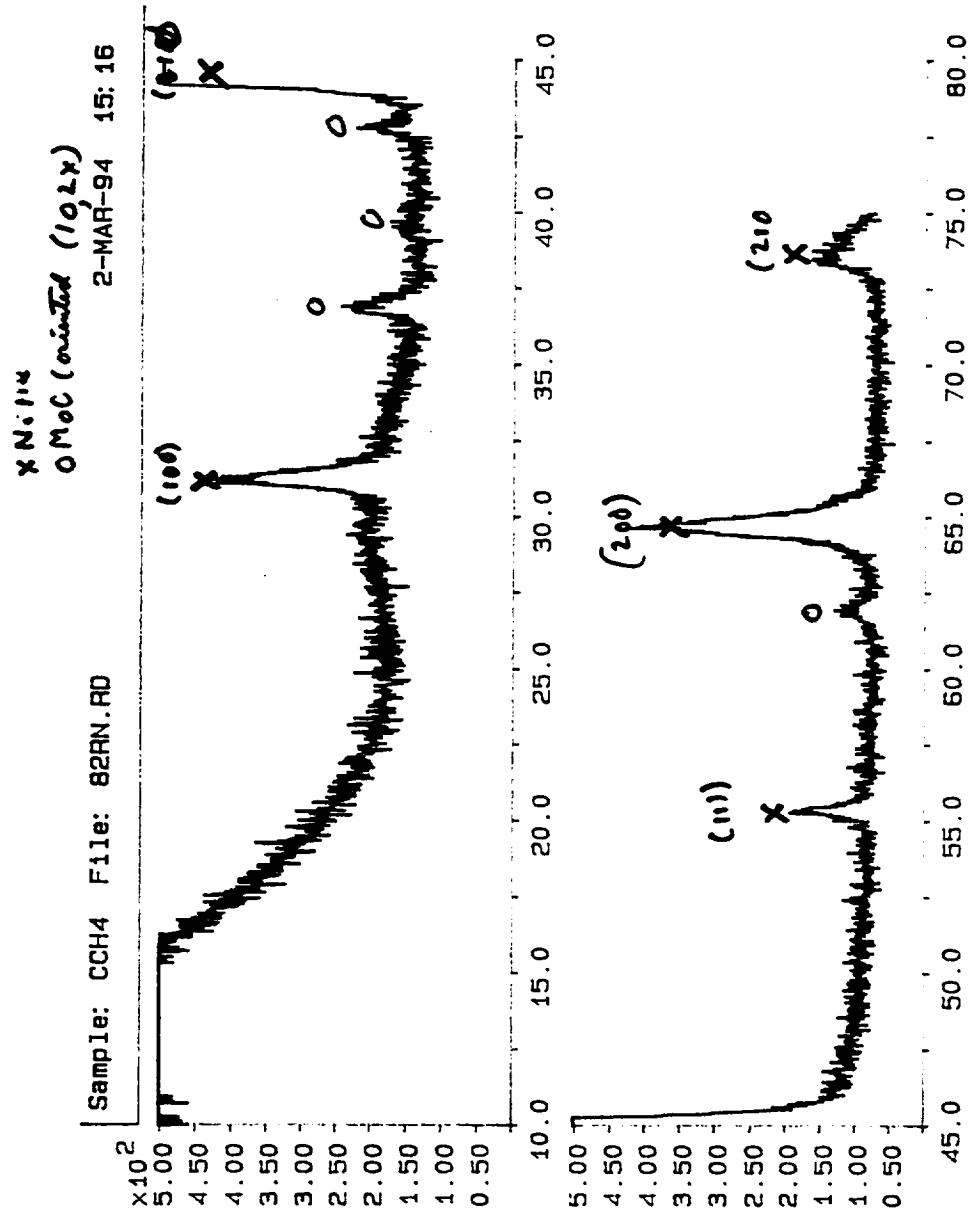


Figure A1: Powder x-ray diffraction scan for an arc-melted NiAl-1Mo-1C ingot.

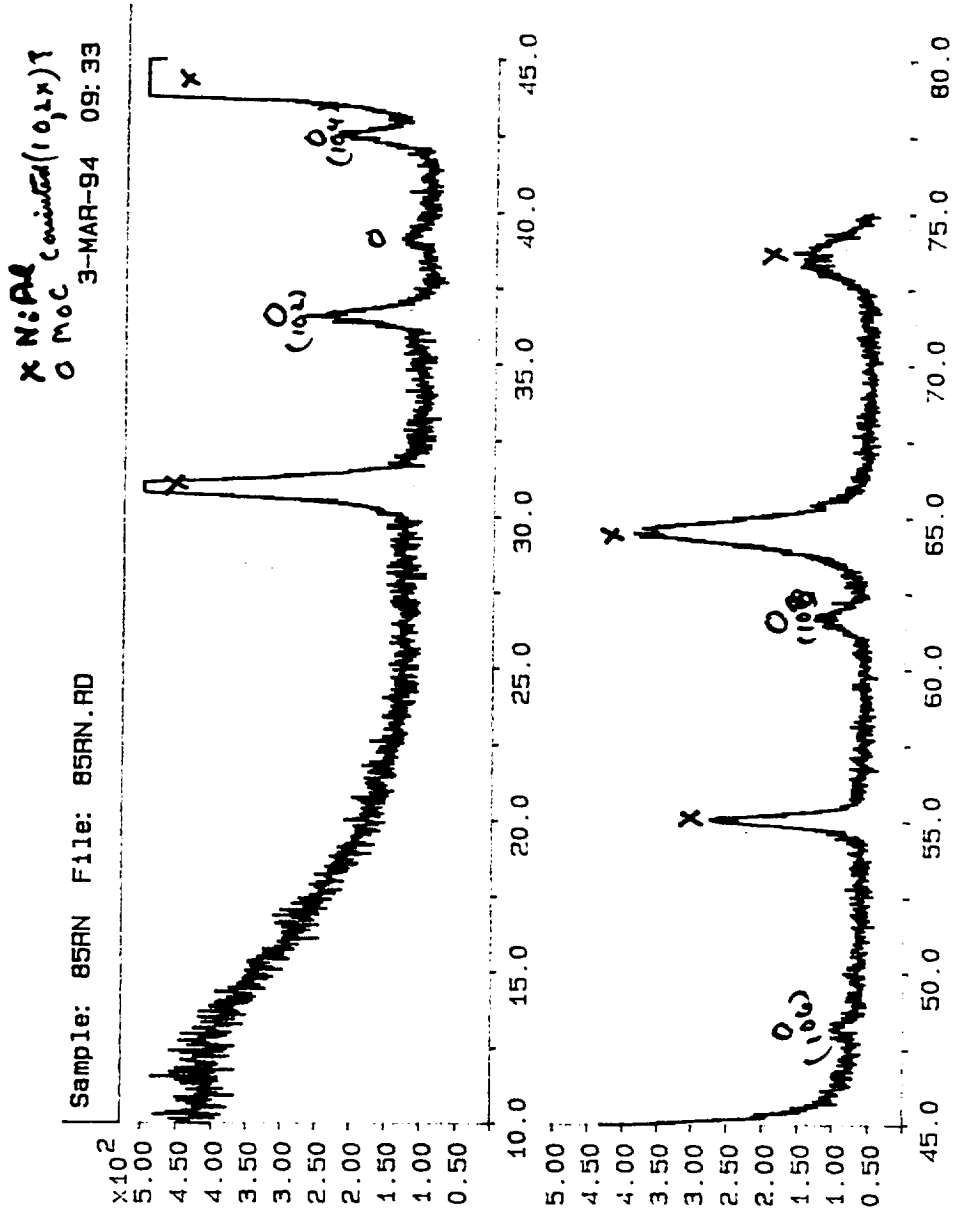


Figure A2: Powder x-ray diffraction scan for an arc-melted NiAl-1Mo-1C ingot.

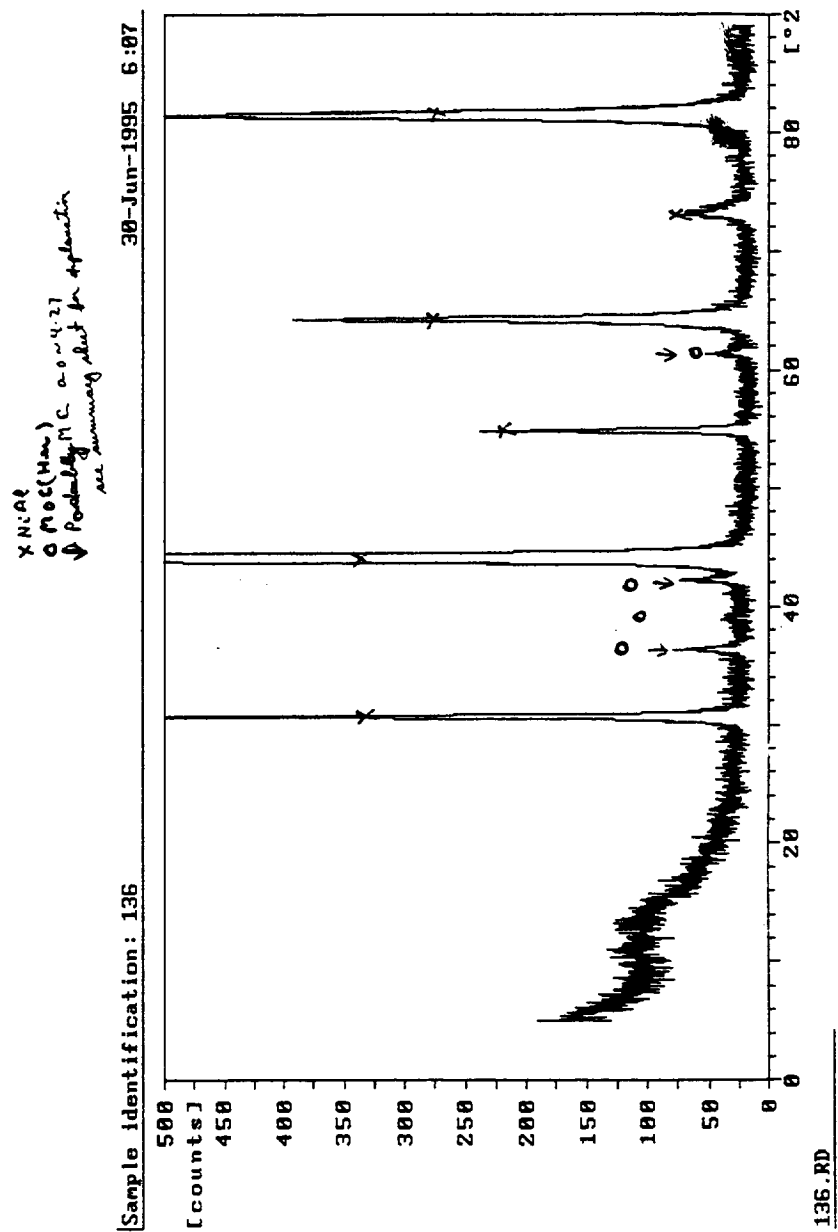


Figure A3: Powder x-ray diffraction scan for an arc-melted NiAl-0.9Mo-0.9C ingot.

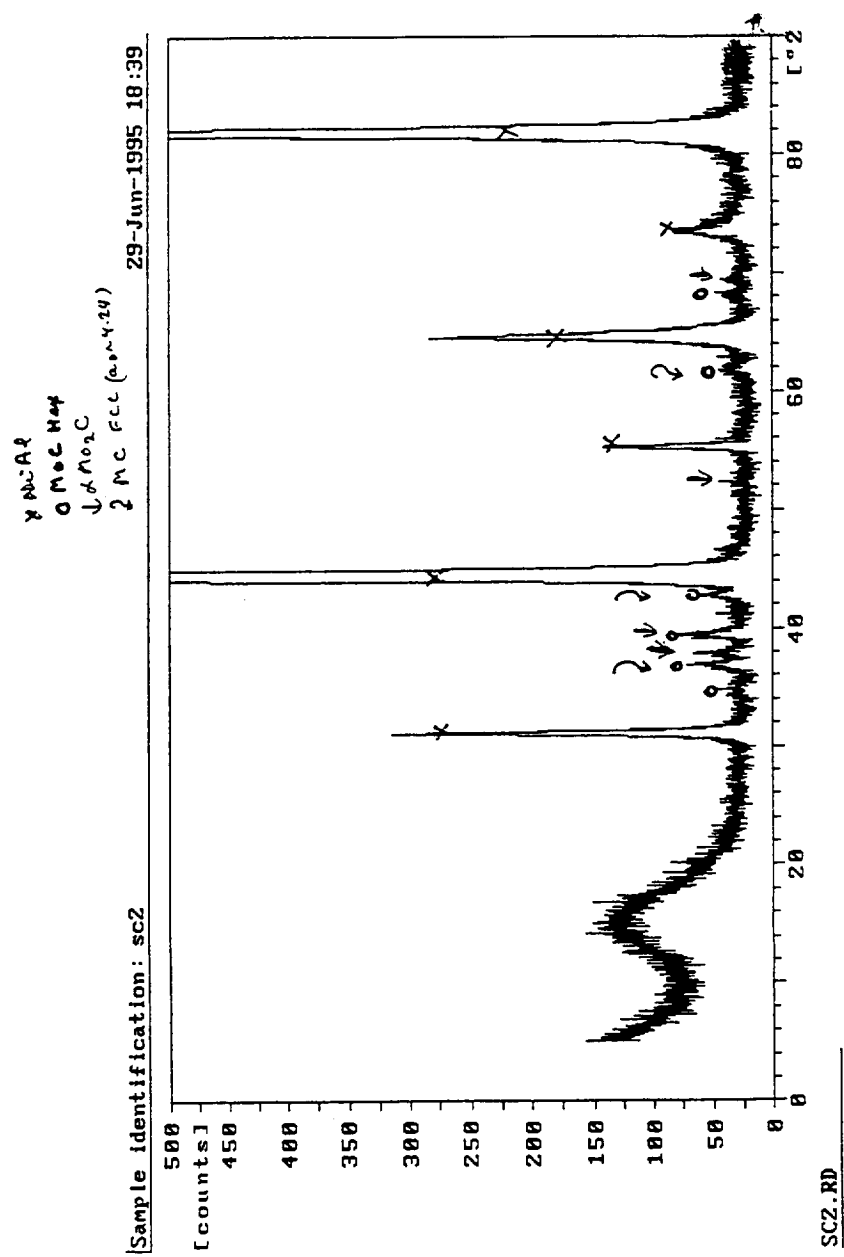


Figure A4: Powder x-ray diffraction scan for a slow cooled NiAl-1Mo-1C ingot.

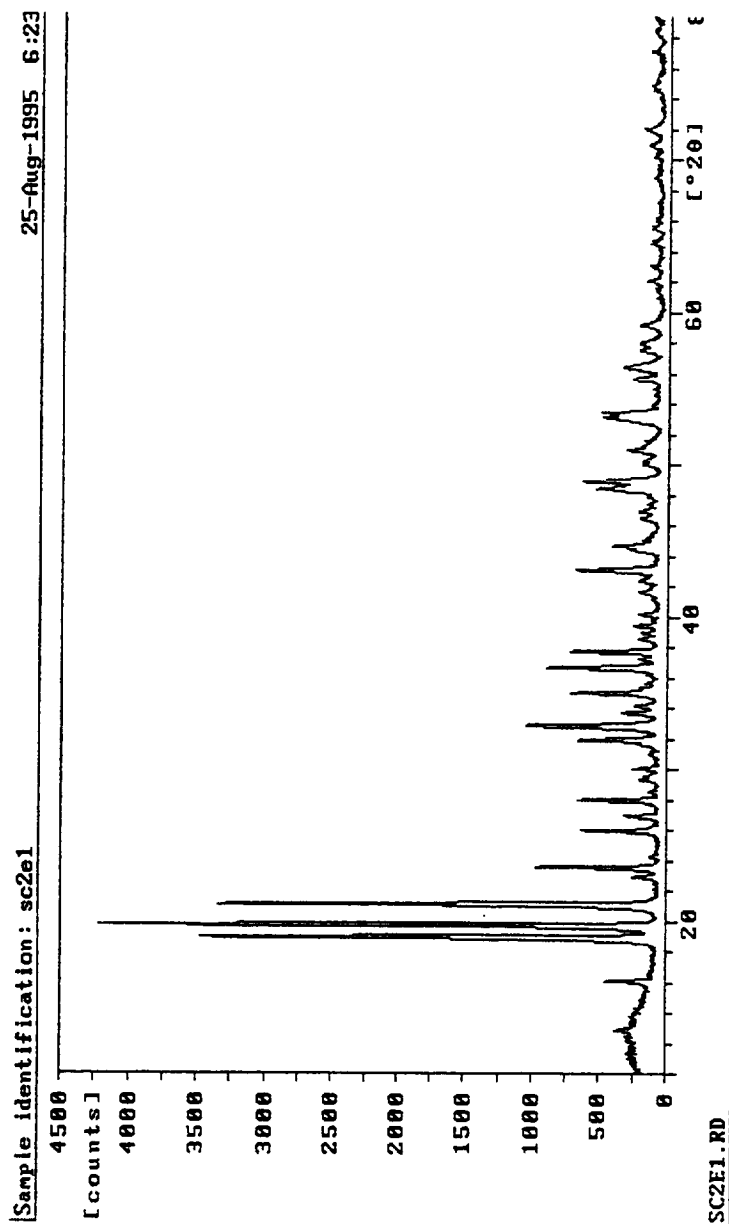


Figure A5: Powder x-ray diffraction scan for an arc-melted NiAl-1Mo-1C ingot etched in Solution 1 for several days.

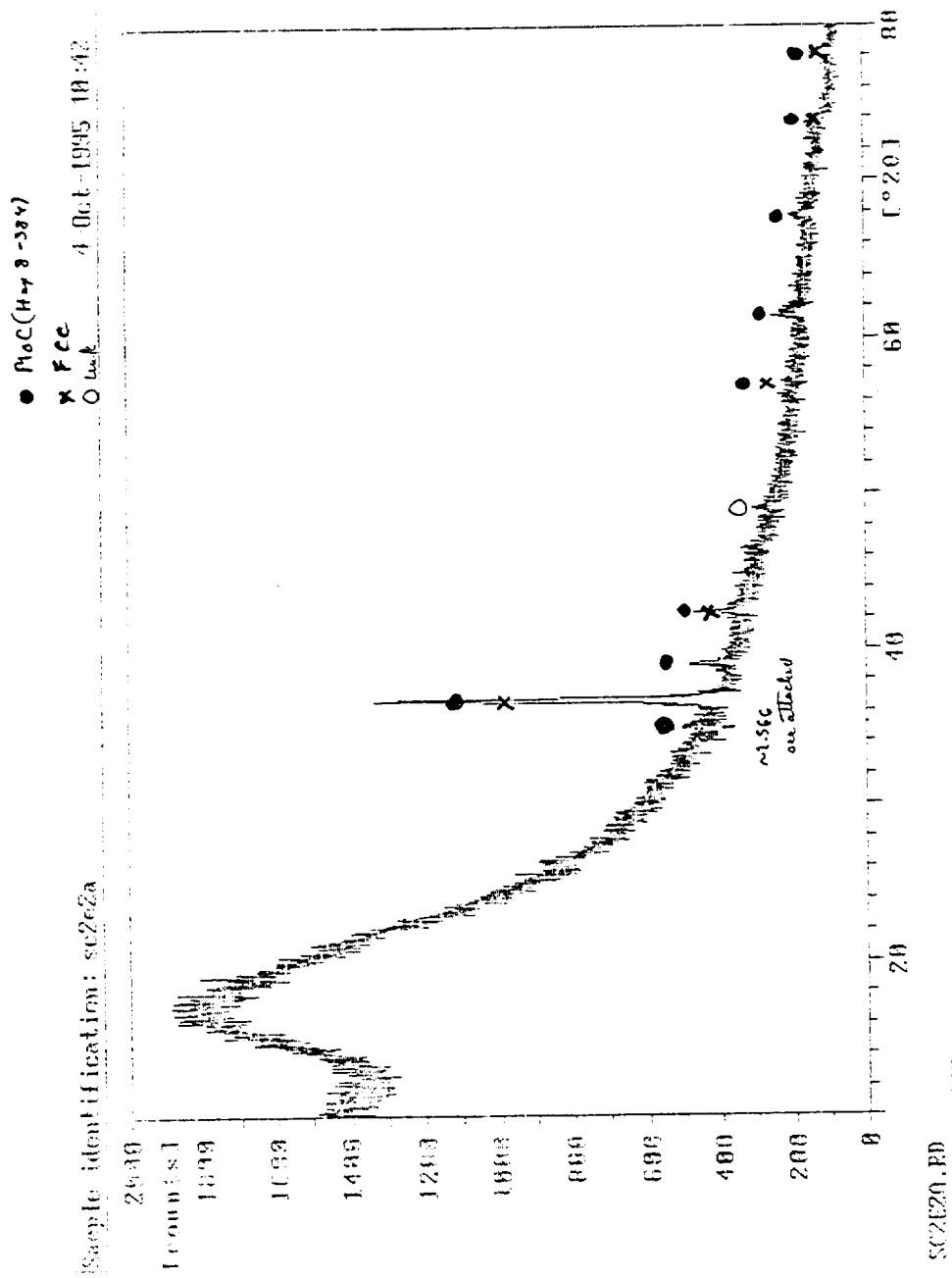


Figure A6: Powder x-ray diffraction scan for an arc-melted NiAl-1Mo-1C ingot etched in Solution 2 for several days.

**APPENDIX B**  
**DTA RESULTS**

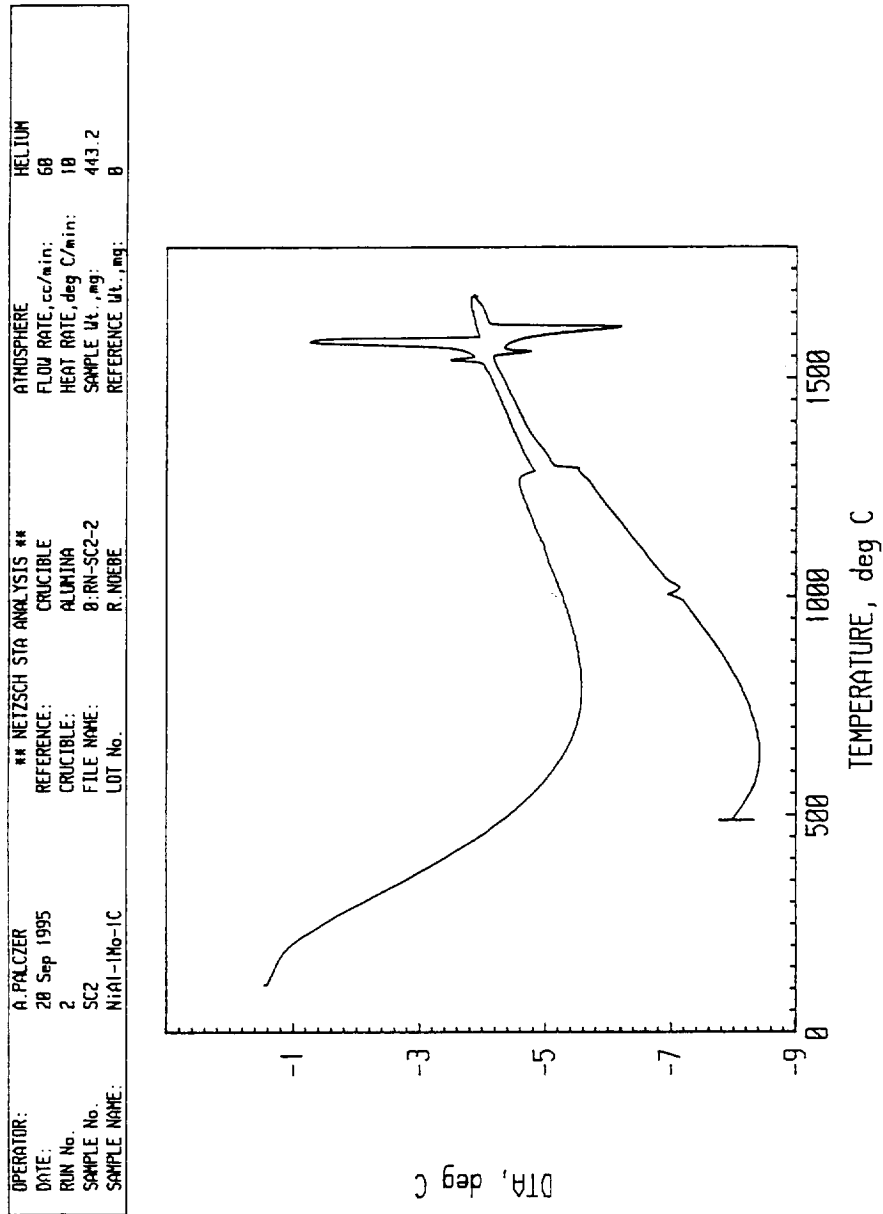


Figure B1: DTA scan for material taken from an NiAl-1Mo-1C slow cooled ingot.

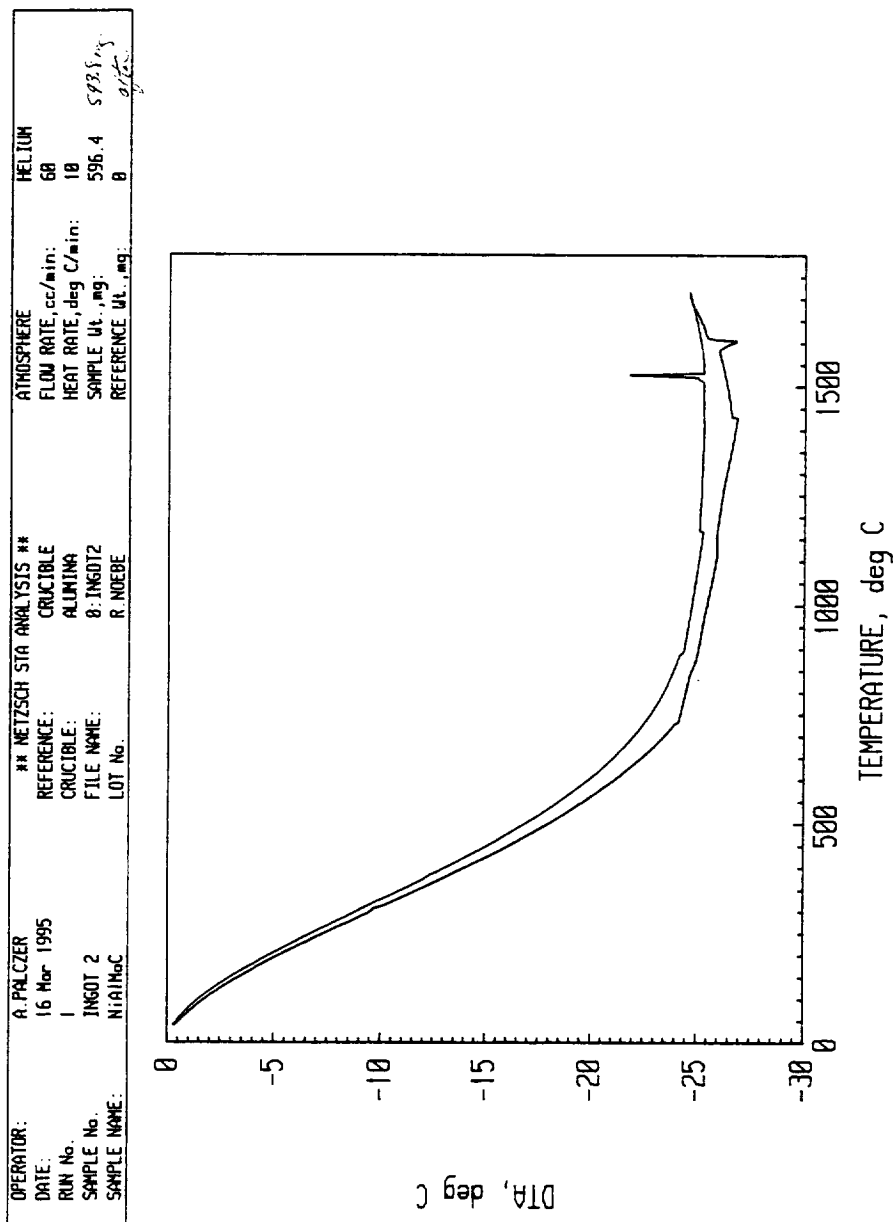


Figure B2: DTA scan for material taken from an NiAl-1Mo-0.61C directionally solidified ingot.

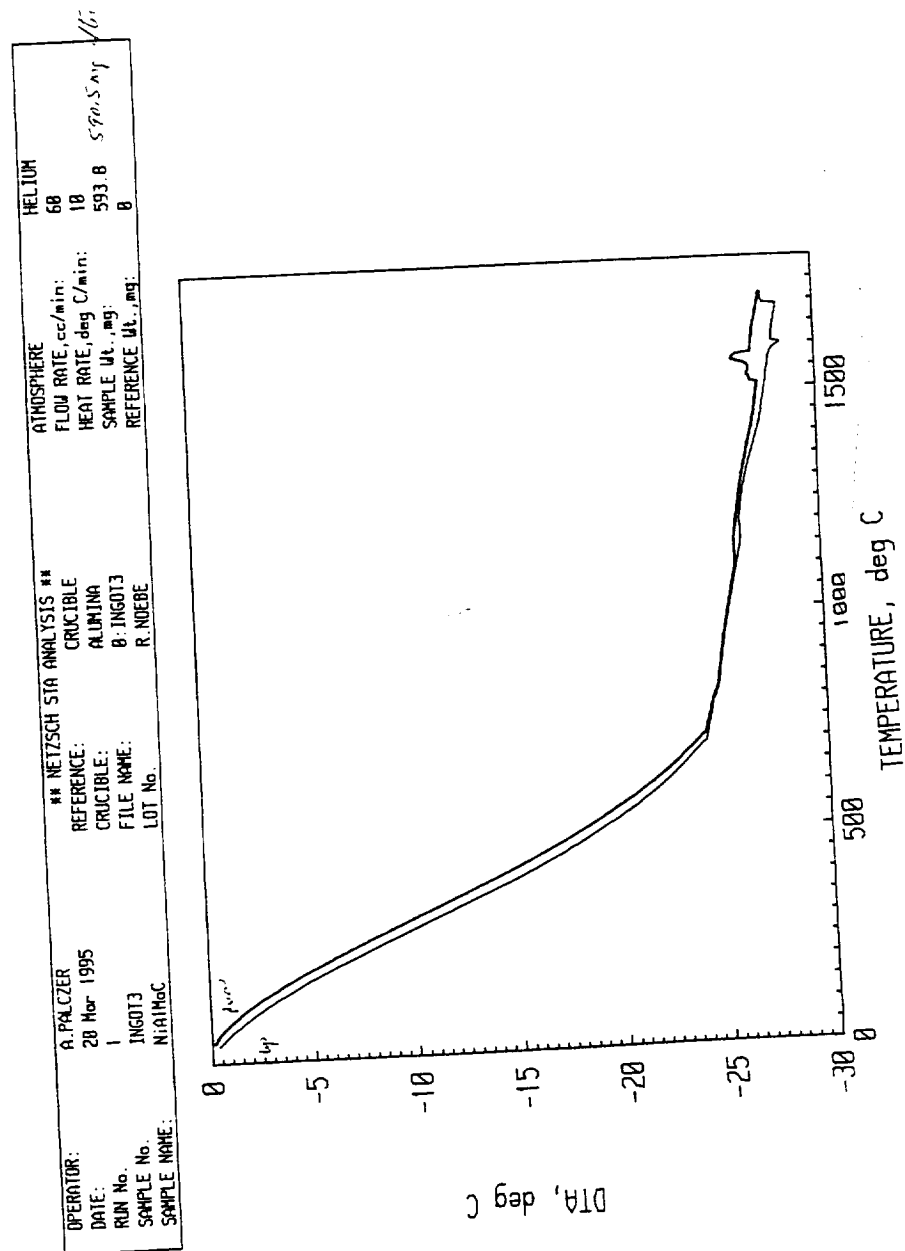


Figure B3: DTA scan for material taken from an NiAl-1Mo-0.73C directionally solidified ingot.

**APPENDIX C**  
**FLEXURE TESTING RESULTS**

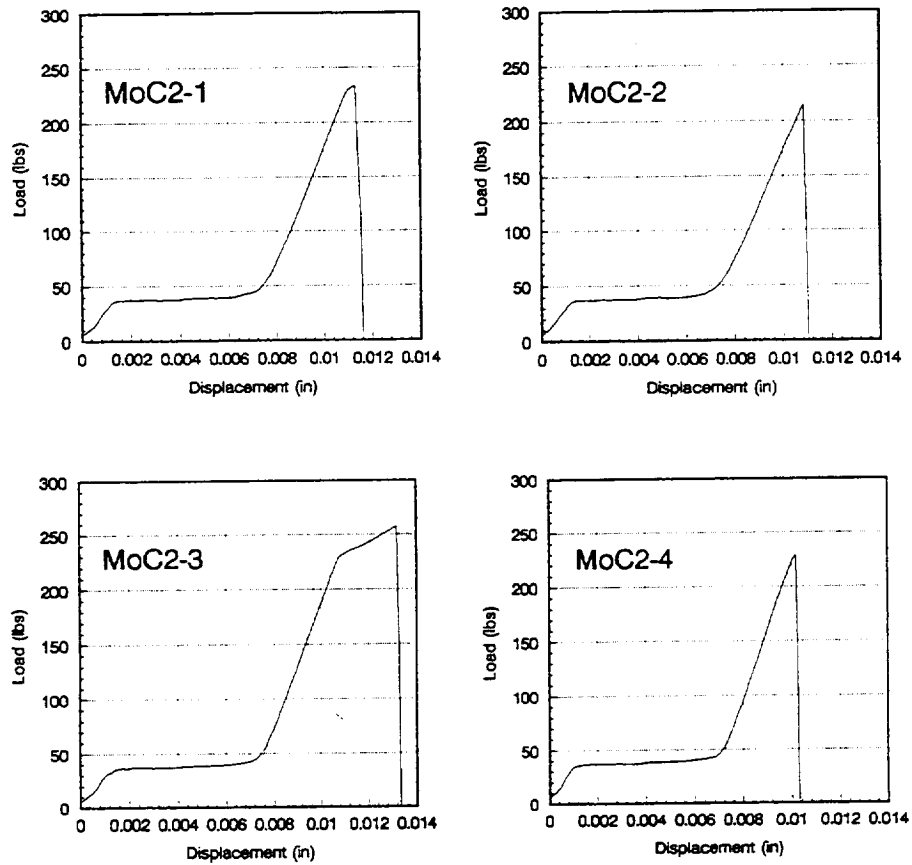


Figure C1: Load-displacement curves for 4-point flexure testing of a directionally solidified NiAl-1Mo-0.61C ingot.

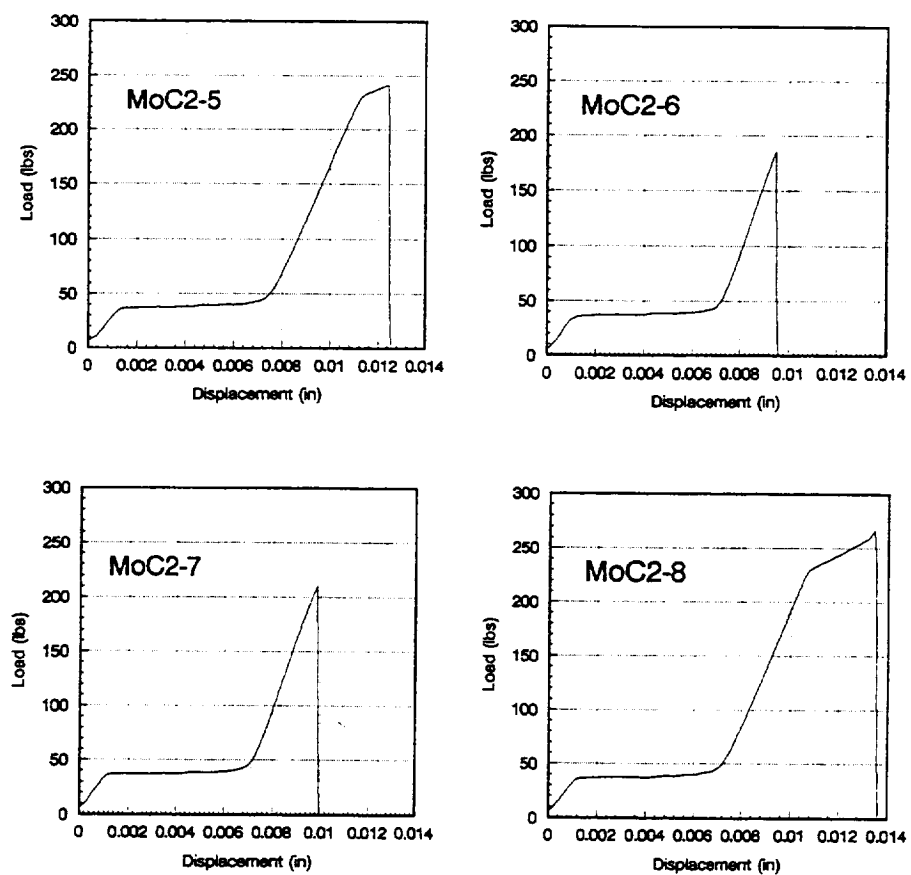


Figure C2: Load-displacement curves for 4-point flexure testing of a directionally solidified NiAl-1Mo-0.61C ingot.

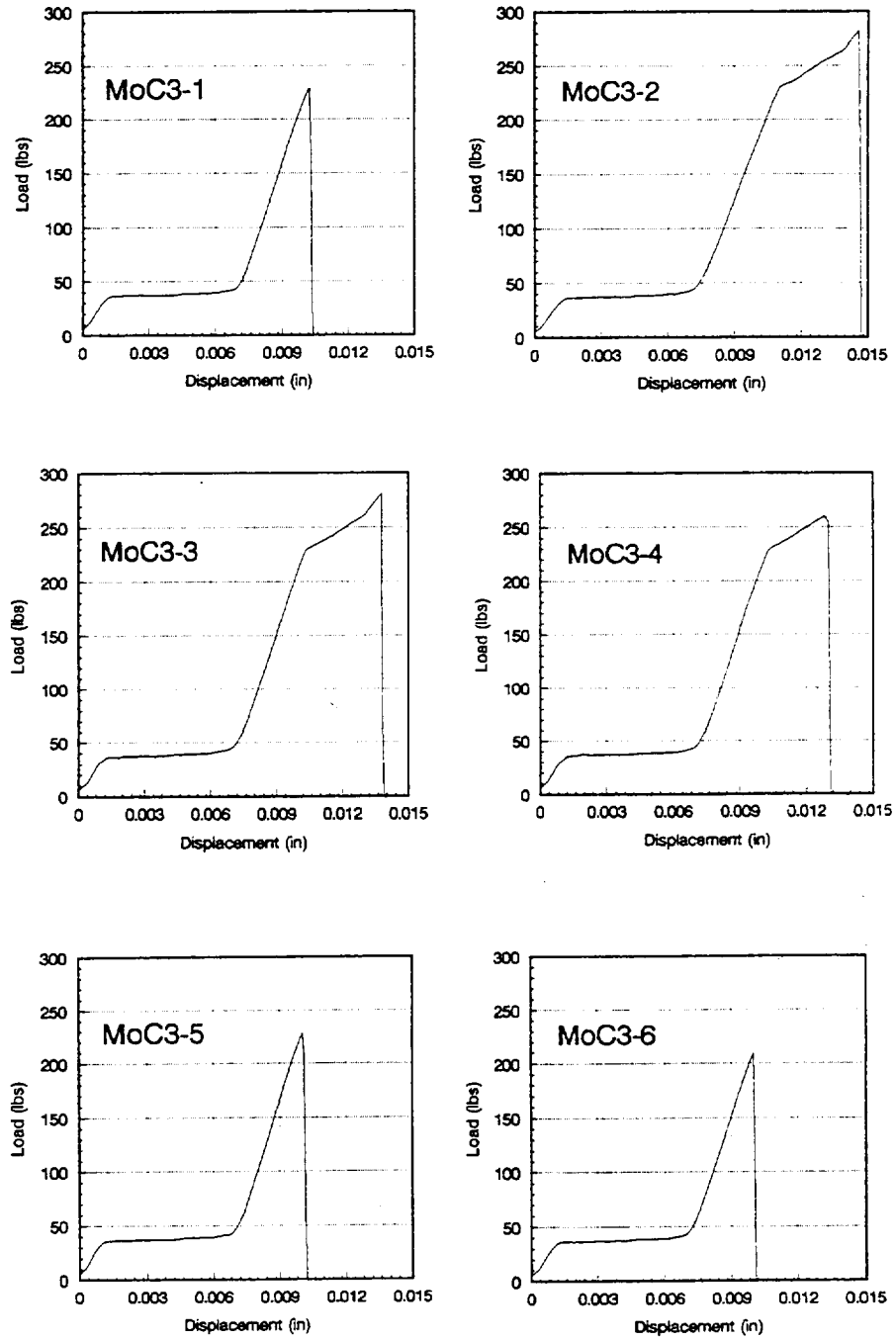


Figure C3: Load-displacement curves for 4-point flexure testing of a directionally solidified NiAl-1Mo-0.73C ingot.

**APPENDIX D**  
**COMPRESSION TESTING RESULTS**

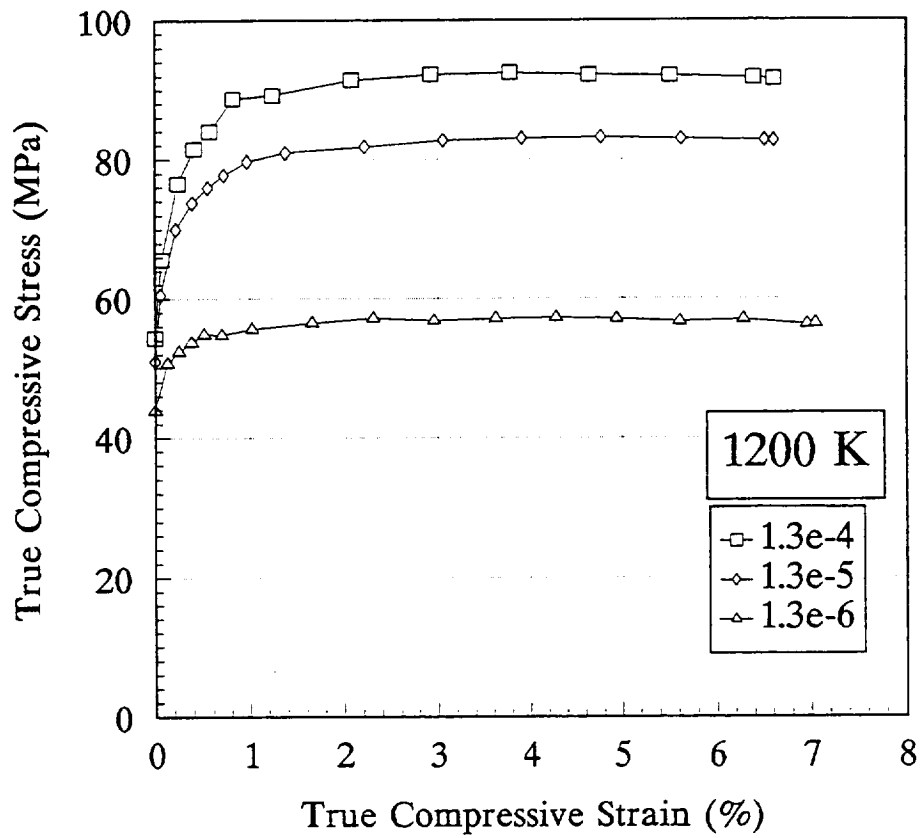


Figure D1: True compressive stress-true compressive strain curves for NiAl-Mo-C directionally solidified ingots at 1200 K.

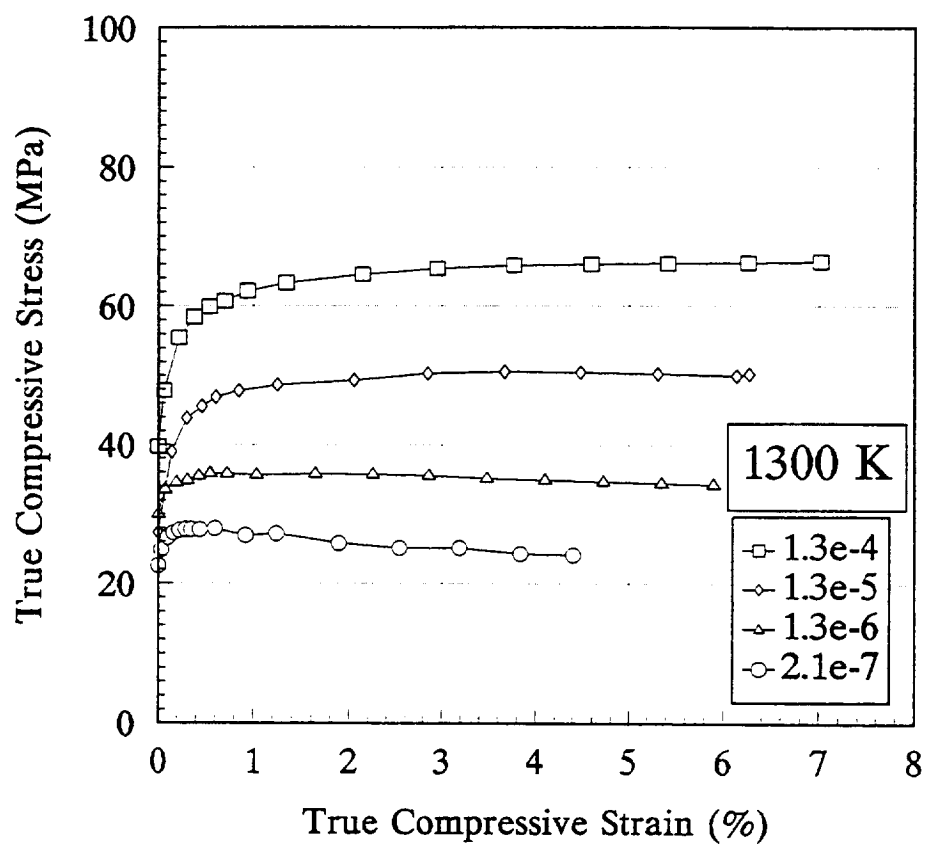


Figure D2: True compressive stress-true compressive strain curves for NiAl-Mo-C directionally solidified ingots at 1300 K.

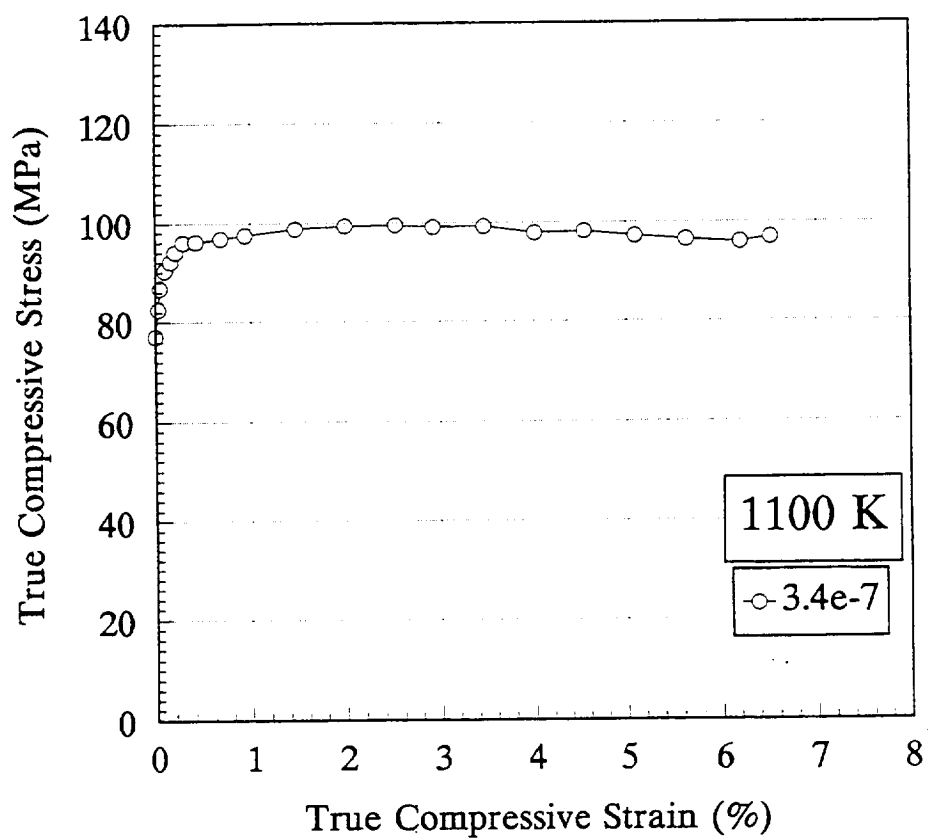


Figure D3: True compressive stress-true compressive strain curves for NiAl-Mo-C slow cooled ingots at 1100 K.

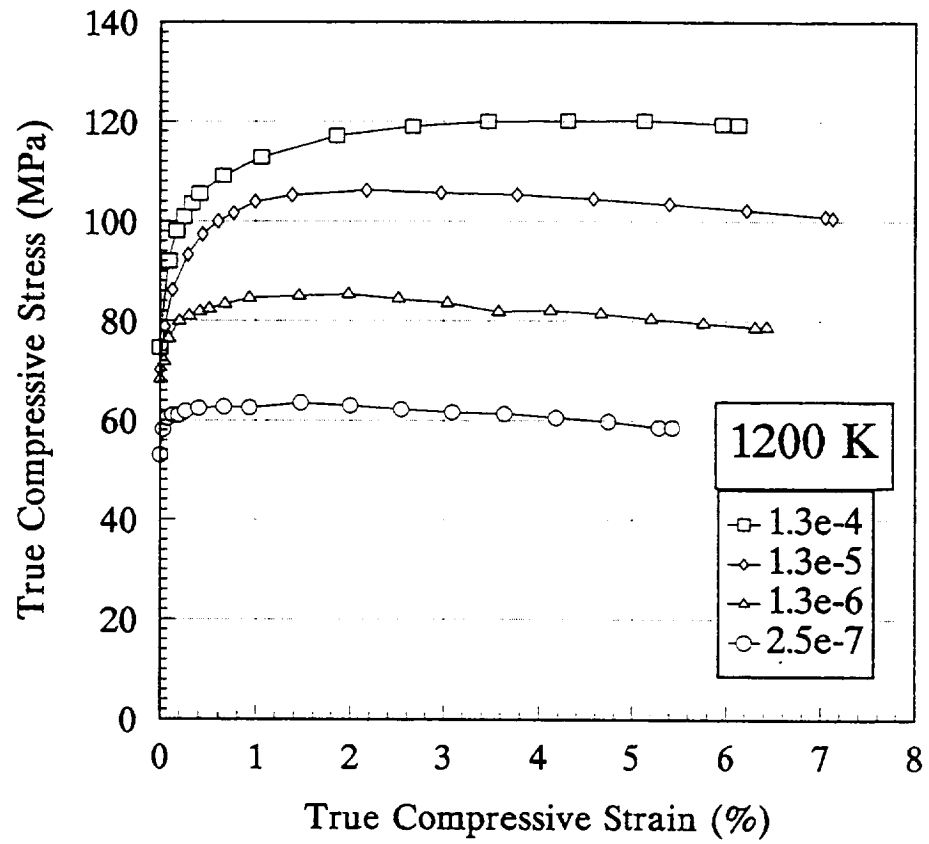


Figure D4: True compressive stress-true compressive strain curves for NiAl-Mo-C slow cooled ingots at 1200 K.

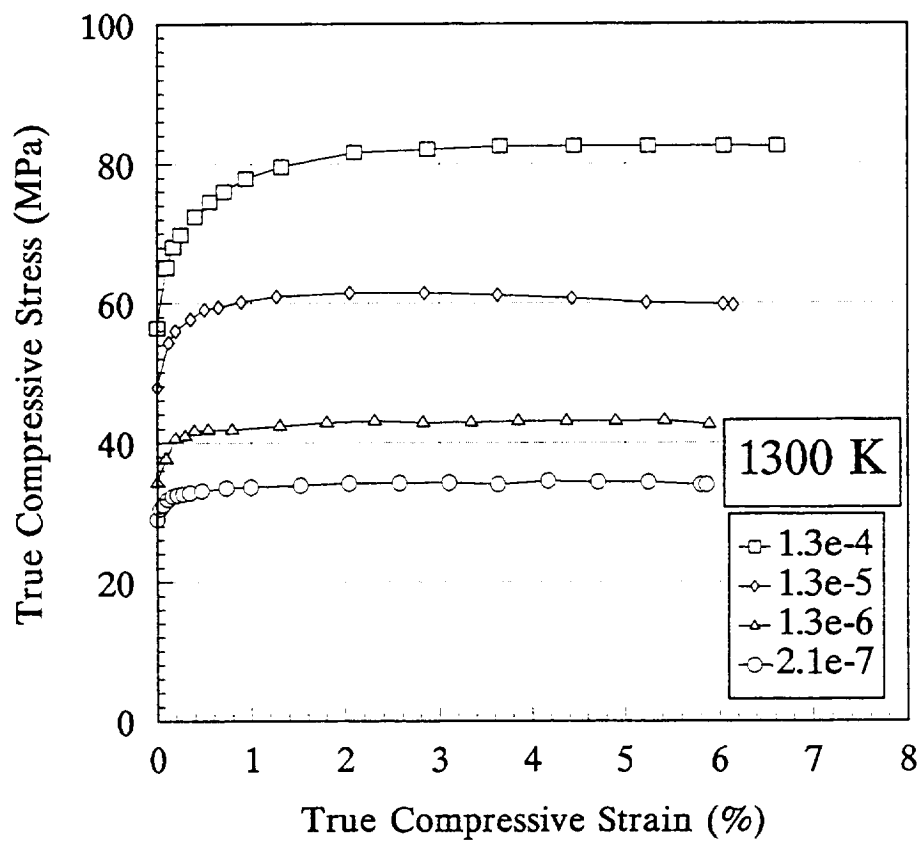


Figure D5: True compressive stress-true compressive strain curves for NiAl-Mo-C slow cooled ingots at 1300 K.

# REPORT DOCUMENTATION PAGE

Form Approved  
OMB No. 0704-0188

Public reporting burden for this collection of information is estimated to average 1 hour per response, including the time for reviewing instructions, searching existing data sources, gathering and maintaining the data needed, and completing and reviewing the collection of information. Send comments regarding this burden estimate or any other aspect of this collection of information, including suggestions for reducing this burden, to Washington Headquarters Services, Directorate for Information Operations and Reports, 1215 Jefferson Davis Highway, Suite 1204, Arlington, VA 22202-4302, and to the Office of Management and Budget, Paperwork Reduction Project (0704-0188), Washington, DC 20503.

<b>1. AGENCY USE ONLY (Leave blank)</b>		<b>2. REPORT DATE</b> April 1996	<b>3. REPORT TYPE AND DATES COVERED</b> Final Contractor Report	
<b>4. TITLE AND SUBTITLE</b>  Development and Processing of Nickel Aluminide-Carbide Alloys			<b>5. FUNDING NUMBERS</b>  WU-505-63-52 G-NAG3-1697	
<b>6. AUTHOR(S)</b>  Timothy Scott Newport				
<b>7. PERFORMING ORGANIZATION NAME(S) AND ADDRESS(ES)</b>  University of Tennessee at Knoxville Department of Materials Science and Engineering Knoxville, Tennessee 37996-0140			<b>8. PERFORMING ORGANIZATION REPORT NUMBER</b>  E-10116	
<b>9. SPONSORING/MONITORING AGENCY NAME(S) AND ADDRESS(ES)</b>  National Aeronautics and Space Administration Lewis Research Center Cleveland, Ohio 44135-3191			<b>10. SPONSORING/MONITORING AGENCY REPORT NUMBER</b>  NASA CR-198454	
<b>11. SUPPLEMENTARY NOTES</b>  This report was submitted as a thesis in partial fulfillment of the requirements for the degree Master of Science to the University of Tennessee at Knoxville, Knoxville, Tennessee, December 1995. Project Manager, Ronald D. Noebe, NASA Lewis Research Center, Materials Division, organization code 5120, (216) 433-2093.				
<b>12a. DISTRIBUTION/AVAILABILITY STATEMENT</b>  Unclassified - Unlimited Subject Category 26  This publication is available from the NASA Center for Aerospace Information, (301) 621-0390.			<b>12b. DISTRIBUTION CODE</b>	
<b>13. ABSTRACT (Maximum 200 words)</b>  With the upper temperature limit of the Ni-based superalloys attained, a new class of materials is required. Intermetallics appear as likely candidates because of their attractive physical properties. With a relatively low density, high thermal conductivity, excellent oxidation resistance, high melting point, and simple crystal structure, nickel aluminide (NiAl) appears to be a potential candidate. However, NiAl is limited in structural applications due to its low room temperature fracture toughness and poor elevated temperature strength. One approach to improving these properties has been through the application of eutectic composites. Researchers have shown that containerless directional solidification of NiAl-based eutectic alloys can provide improvements in both the creep strength and fracture toughness. Although these systems have shown improvements in the mechanical properties, the presence of refractory metals increases the density significantly in some alloys. Lower density systems, such as the carbides, nitrides, and borides, may provide NiAl-based eutectic structures. With little or no information available on these systems, experimental investigation is required. The objective of this research was to locate and develop NiAl-carbide eutectic alloys. Exploratory arc-melts were performed in NiAl-refractory metal-C systems. Refractory metal systems investigated included Co, Cr, Fe, Hf, Mo, Nb, Ta, Ti, W, and Zr. Systems containing carbides with excellent stability (i.e., HfC, NbC, TaC, TiC, and ZrC) produced large blocky, cubic carbides in an NiAl matrix. The carbides appeared to have formed in the liquid state and were randomly distributed throughout the polycrystalline NiAl. The Co, Cr, Fe, Mo, and W systems contained NiAl dendrites with a two-phase interdendritic microconstituent present. Of these systems, the NiAl-Mo-C system had the most promising microstructure for in-situ composites. Three processing techniques were used to evaluate the NiAl-Mo-C system: arc-melting, slow cooling, and containerless directional solidification. Arc-melting provided a wide range of compositions in an economical and simple fashion. The slow cooled ingots provided larger ingots and slower cooling rates than arc-melting. Directional solidification was used to produce in-situ composites consisting of NiAl reinforced with molybdenum carbides.				
<b>14. SUBJECT TERMS</b>  NiAl; NiAl-carbide alloys; Fracture; Creep			<b>15. NUMBER OF PAGES</b> 148	
			<b>16. PRICE CODE</b> A07	
<b>17. SECURITY CLASSIFICATION OF REPORT</b> Unclassified	<b>18. SECURITY CLASSIFICATION OF THIS PAGE</b> Unclassified	<b>19. SECURITY CLASSIFICATION OF ABSTRACT</b> Unclassified	<b>20. LIMITATION OF ABSTRACT</b>	



National Aeronautics and  
Space Administration

**Lewis Research Center**  
21000 Brookpark Rd.  
Cleveland, OH 44135-3191

Official Business  
Penalty for Private Use \$300

POSTMASTER: If Undeliverable — Do Not Return